Decentralized Schemes for Grid-Forming Inverter System Efficiency Improvement and Online-Inverter Detection

by

Ali Sheykhi

A thesis submitted in partial fulfillment of the requirements for the degree of

Master of Science

in

Energy Systems

Department of Electrical and Computer Engineering

University of Alberta

Abstract

Parallel grid-forming (GFM) inverters are used in many modern power system applications. Therefore, improving their system efficiency is of paramount importance for energy savings. The droop control method has been conventionally used to share the power among inverters proportional to their power ratings. However, the droop strategy does not guarantee an efficient power sharing especially at light loads, where the low power demand is divided among inverters, forcing them to supply a low power at a low efficiency according to their efficiency curve. Addressing the aforementioned issue while maintaining the advantages of parallel inverters used in residential areas is the focus of this thesis.

A nested-loop control system for a single-phase inverter operating in standalone mode is introduced. The control system includes current, voltage, and harmonic control loops, and is designed based on the linear quadratic tracking (LQT) optimal control method. The designed controllers exhibit a satisfactory performance in tracking the reference signals and rejecting the unwanted harmonics in case of linear and nonlinear loads. Moreover, a total harmonic distortion (THD) of 1.65% is obtained when a nonlinear load is connected to the system.

A decentralized modified droop strategy is also proposed to improve the system efficiency of parallel grid-forming inverters. The main idea is to control the power sharing among the inverters such that the output power of each inverter is maintained within a proper range with respect to the inverter efficiency curves. Hence, an optimal

number of inverters supply the loads efficiently, and the unnecessary inverters do not share any power. In contrast to the existing methods, the proposed method does not have a single point of failure while it features modularity, flexibility, and reliability. Additionally, the reliability of the system is enhanced by extending the lifetime of inverters with higher power ratings which are considered as valuable assets of the system. Furthermore, a stability verification of the system within the designed operating range of the inverter no-load frequencies is conducted to ensure a stable operation.

As in very-light load situations none of the inverters can operate within the proper power range with a high efficiency, an online-inverter detection (OID) method is proposed such that each inverter detects the online inverters and the unnecessary inverters stop injecting power to obtain a higher system efficiency. As the proposed OID is decentralized and modular, more inverters can be added to the system without adjusting the settings of installed inverters. Detailed derivations, simulations, and experimental results are presented to validate the effectiveness of the schemes.

I dedicate this thesis to my amazing parents for their unconditional love and support.

Acknowledgments

I would like to express my deepest appreciation to my thesis supervisor Dr. Sayed Ali Khajehoddin for giving me the amazing opportunity of pursuing my master's degree at the prestigious University of Alberta in a vibrant and friendly research group. I would also like to thank him for the guidance, support, encouragement, and insightful feedback.

My greatest appreciation is extended to Dr. Nima Amouzegar Ashtiani who helped me substantially during my research project both technically and emotionally. Not only am I indebted to him for the collaborative effort in the experimental phase of my project, but I would also like to thank him for all the constructive discussions on theoretical aspects.

I would also like to thank my fellow graduate students in the uAPEL lab, especially Dr. Mohammad Ebrahimi and Dr. Amin Khakparvar for their professional and emotional support throughout these years.

Last but certainly not least, I would like to express a great debt of gratitude to my parents for all their invaluable emotional support, encouragement, and devotion. Without their support, none of this would have been possible.

Contents

List of Tables

List of Figures

List of Symbols

η	Overall system efficiency
$\omega_k^{nl,\text{cod}}$	Coded no-load angular frequency of the kth inverter
ω_k^{nl}	No-Load angular frequency of the kth inverter
ω_{VSM}	Virtual rotating speed of the virtual synchronous machine
ω_g	Grid angular frequency
ω_{nom}	Nominal angular frequency
ω_k	Angular frequency of the kth inverter
i^{ref}	Reference current
i_L	Load current
i_1	Current of the inverter-side inductor
i_2	Current of the load-side inductor
P_k^{loss}	Average power loss of the kth inverter
P^{fl}	Inverter full-load power
P_L	Injected power to the loads
P_k	Average power of the kth inverter
p_k	Instantaneous power of the kth inverter
Q_k	Average reactive power of the kth inverter
q_k	Instantaneous reactive power of the kth inverter
v^{inv}	Inverter voltage
v^{ref}	Reference voltage
v_k^{vir}	Voltage drop across the virtual impedance of the kth inverter

V_k^{nl}	No-Load voltage amplitude of the kth inverter
v_L	Load voltage
V_{nom}	Nominal voltage
v_{c_L}	Capacitive part of the load voltage
v_c	Voltage of the LCL filter capacitor
V_{dc}	DC link voltage
V_k	Voltage amplitude of the kth inverter

Chapter 1

Introduction

In general, inverters can be categorized into two groups of grid-following (GFL) and grid-forming (GFM). GFL inverters should be synchronized with the grid voltage and frequency at the point of common coupling (PCC). Therefore, they are used in grid-connected mode in applications such as photovoltaic (PV) systems, wind power systems, and line-interactive uninterruptible power supply (UPS) systems. On the other hand, GFM inverters regulate the frequency and voltage amplitude of the local grid. Hence, they can operate independently in standalone mode. GFM inverters are used in several applications such as standby UPS systems, energy storage systems, and islanded microgrids. Thus, GFM inverters are suitable for remote areas with no access to the main grid. They are also required in situations where there might be an emergency need of electricity such as hospitals [1–9].

There are a variety of reasons that has encouraged the use of parallel inverter systems instead of a single-inverter system in many applications; some of which are as follows: higher power capacity, reliability, flexibility, modularity, and preventing single-point of failure [10–13]. Parallel inverters are widely utilized in power system applications, such as microgrids, UPS systems, photovoltaic systems, interlinking converters, and high-power wind energy conversion systems [12–15].
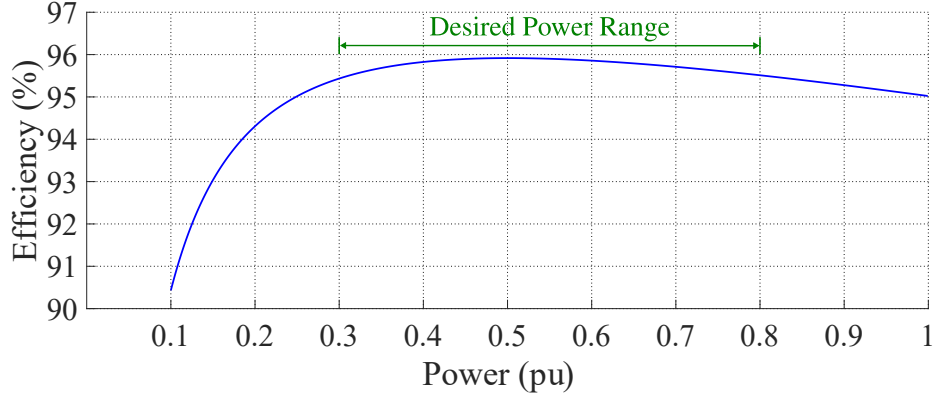
Figure 1.1: Inverter typical efficiency curve.

Table 1.1: European and CEC Efficiency Weight Factors.

	$\eta_{5\%}$	$\eta_{10\%}$	$\eta_{20\%}$	$\eta_{30\%}$	$\eta_{50\%}$	$\eta_{75\%}$	$\eta_{100\%}$
EU	0.03	0.06	0.13	0.1	0.48	0	0.2
CEC	0	0.04	0.05	0.12	0.21	0.53	0.05

In some inverter applications, the system operates at light loads for long periods of time, such as PV systems, portable battery-powered energy storage systems, and remote microgrids where the load profile is below half of the peak value for the majority of the day [16]. In such light-load applications, the efficiency of the inverter is normally low as shown in Fig. 1.1. To take this into account in PV applications where the irradiation varies in a wide range, the European (EU) and California Energy Commission (CEC) weighted efficiencies [17] are introduced such that inverters are evaluated not only based on their peak efficiencies but also based on a weighted average of their efficiencies from 5% to 100% of the full-load power as seen in Table 1.1.

Solar inverters with power switches based on wide-bandgap materials such as silicon carbide (SiC) and gallium nitride (GaN) provide high CEC efficiencies. For instance, consider three inverter products shown in Table 1.2 whose CEC efficiencies are high [18–21]. As can be seen in the efficiency curves of the inverters illustrated in Fig. 1.2, despite the overall high efficiency, their efficiencies are lower at light loads.

Table 1.2: Three inverter products with high CEC efficiency.

Inverter Model	Rated Power	CEC Efficiency
SolarEdge SE3000H-US	3 kW	99%
Delta M6-TL-US	6 kW	97.5%
Huawei SUN2000-10KTL-USL0	10 kW	99%
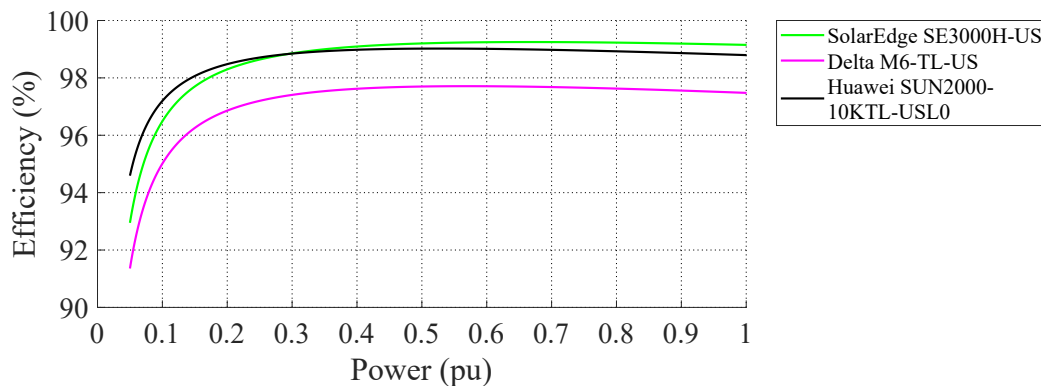
Figure 1.2: Efficiency curves of three inverter products with high CEC efficiencies.

The reason is that there are auxiliary circuits in the inverter products which always produce constant losses. Such losses are more conspicuous at light loads, and thus, the efficiency would be lower. Hence, improving the system efficiency of inverters operating at light loads plays a key role in energy savings in PV systems.

The droop control method has been conventionally used to share the required power by the loads among parallel inverters proportional to their power capacity [22–25]. However, this method does not guarantee efficient power sharing, especially at light-load conditions, where the inverters only process a portion of the low output power forcing them to operate at powers where the inverters normally have low efficiency as shown in Fig. 1.1. Hence, the power sharing among inverters needs to be revised to reduce the losses and increase the system efficiency. This thesis focuses on improving the overall efficiency of parallel GFM inverter systems operating in standalone mode, which are used in residential areas.

3

In this chapter, first, the control system structure and design method for a single inverter is discussed. Next, the concept of the proposed efficiency improvement method is explained, and an online-inverter detection (OID) method is introduced to enhance the system efficiency in very-light load situations. Finally, the chapter concludes with the thesis objectives and thesis outline.

1.1 Single Inverter Control

Three common structures used for controlling the output of a plant $G(s)$ are shown in Fig. 1.3. In the single-loop control systems, the output of the plant is directly controlled by the controller, $C(s)$, whereas in state-feedback control approaches, the control signal u applied to the plant is formed by a linear combination of system states. The aforementioned structures are limited to controlling the system output and cannot control other variables of the system. Nested-loop structures, however, provide more degrees of freedom in terms of controlling the internal variables of the system. For instance, in Fig. 1.3(c), the internal variable y_1 can be controlled similar to the system output y_2. By shaping the dynamics of the internal variables, the control system can protect the plant against unexpected disturbances and also improve the overall performance of the system.
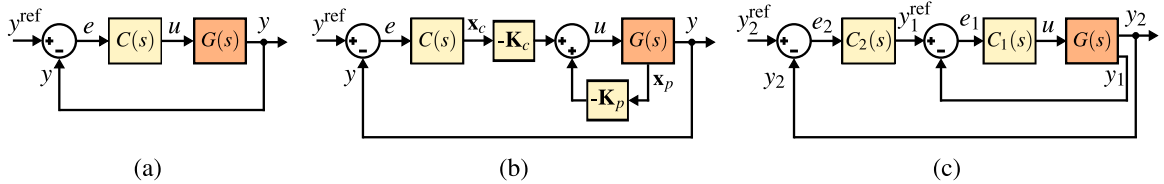
Figure 1.3: Control system structures: (a) single-loop control, (b) state-feedback control, and (c) nested-loop control.

1.1.1 Nested-Loop Control Systems in Power Electronics

The most common nested-loop control system used in power electronics includes an outer loop which is responsible to track the reference voltage and an inner current loop that ensures current reference tracking and system stability against uncertainties [26]. It is worth mentioning that the inner loop receives its reference from the outer loop as depicted in Fig. 1.3(c). A nested-loop control system with an inner current control loop provides more features in comparison with single-loop structures such as shaping the current, protecting the system against overcurrent, and reducing harmonic distortion [27].

Nested-loop control systems are used in applications such as motor drives, renewable energy systems, and battery chargers [27–29]. A nested control system including power, current, and voltage loops is proposed in [30] to control the single-phase inverters of small-scale renewable energy systems in a microgrid. Moreover, Nested-loop control systems can be used to control the dc-link voltage and inverter current of single-phase solar PV systems while achieving maximum power point tracking (MPPT) [31]. Furthermore, nested control systems are utilized in three-phase systems such as in [32], where the operation of a microgrid supplying unbalanced loads with distorted currents is investigated, and in [33], where a systematic method is proposed to optimally design the nested control loops of a grid-connected inverter.

Nested-loop control systems are capable of rejecting current and voltage harmonics by incorporating harmonic rejection compensators, as well. In an approach presented in [34], virtual admittance and virtual impedance loops are augmented with the inverter nested control system to attenuate the current harmonics in grid-connected and voltage harmonics in islanded operations of the microgrid, respectively. In another approach, a multiresonant harmonic compensator is included in the inner current loop of an inverter to reject the low-order harmonics of the load current under nonlinear loads [35]. Furthermore, as proposed in [36], selective harmonic compensation can be

achieved by adding a secondary control loop to the inner proportional-resonant (PR) controllers of inverters.

1.1.2 Nested-Loop Control Design Methods

There are two general approaches to design nested-loop control systems which are discussed below:

1.1.2.1 Sequential Design

Sequential design is the most conventional method to design nested-loop control systems. In this method, each inner loop should be designed sufficiently faster than its immediate outer loop such that the dynamics of the inner loop can be ignored or approximated by a simple transfer function in the design of the outer loop [37–39]. Despite the simplicity of this design method, the system may have a sluggish performance due to the timescale difference between the loops. Moreover, in sequential designs, large disturbances can lead to inter-loop interactions and result in system instability in case of timescale violations in practical applications.

1.1.2.2 Unified Design

In unified design methods, the interactions among the loops are considered and all the loops are designed together. Once the dynamic equations of the entire system are derived, the control loops can be designed optimally using state-feedback control methods such as the well-known linear-quadratic regulator (LQR) [40]. LQR offers high gain and phase margins, and robustness against system parameter uncertainties and nonlinearities [41].

The majority of the LQR methods used in power electronic applications are applied to three-phase systems as in the dq-frame, the variables are dc and the control tracking problem is converted to a regulating problem which can be solved by LQR.

A systematic design procedure for the weight matrix of the LQR problem is proposed in [42], where LQR-based selective harmonic controllers are used to reject the grid voltage harmonics. Furthermore, a linear quadratic Gaussian (LQG) Kalman filter can be used to estimate the state variables as proposed in [43,44], where an LQR controller is used for a three-phase inverter in synchronous frame. In the formulations of the aforementioned methods, the reference and disturbance inputs are ignored, which may result in a non-optimal solution without a guarantee that the advantages of the LQR tool are obtained.

The application of LQR in single-phase systems faces more challenges compared with three-phase systems since the variables are ac and the tracking problem should be converted to a regulating problem. The implementation of LQR control in a single-phase grid-connected residential solar system with active power filtering is investigated in [45]. A current control approach for single-phase inverters based on the LQR method is proposed in [46], where the controller addresses the start-up transient, active damping, current distortions, and steady-state tracking. In another approach, the feasibility of the LQR with integral action (LQRI) controller is evaluated for the single-phase PUC5-LCL inverter [47]. In single-phase LQR methods, the defined cost functions may not have a clear correlation with state variables of the tracking problem. Hence, the weight matrix of the LQR method should be selected by a long trial-and-error process in most of the methods and the result may not be optimal.

To address the current tracking problem and the mentioned issues in a single-phase grid-connected inverter, a design procedure is developed in [48], where the state-space model of the tracking problem is transformed to a new state space whose cost function can be minimized by the proposed linear quadratic tracking (LQT) approach that is based on LQR. An LQT design procedure based on the procedure introduced in [48] is proposed in this thesis for the control system of a standalone single-phase inverter. The control system has a nested-loop structure and contains

voltage, current, and harmonic control loops. The voltage and current controllers ensure high-quality reference tracking performance. Moreover, the selective harmonics controller rejects the unwanted harmonics from the inverter voltage.

1.2 Grid-Forming Inverter System Efficiency Improvement

As mentioned earlier, parallel GFM inverter systems are preferred to a single inverter in many applications due to various advantages. As higher number of inverters can have various operating modes, their operations and design have more flexibility to be optimized compared to a single large inverter. This has motivated researchers to improve the overall system efficiency of GFM inverters leading to a significant amount of energy savings and reducing the operation costs [11]. Control strategies proposed in the literature to improve the system efficiency of GFM inverters in microgrids and other applications can be classified into three categories as follows:

1.2.1 Optimization-Based Methods

The first category includes optimization algorithms used to minimize the losses and enhance the system efficiency. An adaptive control method based on an exhaustive optimization algorithm is presented in [12] to enhance the reliability and efficiency of parallel wind power converters by optimizing the power sharing. A hybrid control structure to optimize the system efficiency is proposed in [16], where an average power control method is utilized to determine the power-sharing ratio that enhances the efficiency of blocks of interconnected inverters. Furthermore, the loss minimization problem of parallel inverters is solved in [49] by particle swarm optimization algorithm to achieve optimal power sharing among the units. A similar method is proposed in [11], where the current reference of each inverter is determined by particle swarm

optimization with the purpose of optimizing the overall system efficiency.

1.2.2 Hierarchical-Control-Based Methods

The second category includes efficiency-improvement methods through hierarchical control strategies. Hierarchical control strategies with multiple control levels are commonly used in microgrids as per the ANSI/ISA-95 standard [50,51]. Each level has a separate control objective, and the reference signals of the lower levels are provided by the higher levels [22, 52–55]. In the context of efficiency improvement, a forward-backward sweep method based on the tertiary level of hierarchical control strategy is developed in [10] to determine the optimal power sharing of parallel inverters. In addition to efficiency enhancement, such tertiary-level control can also stabilize the voltage using the hierarchical control framework [56]. The efficiency and reliability [57] improvements can also be achieved by the secondary control level of hierarchical control schemes, where finite state machine model is utilized in [58] to find the optimal number of inverters to share the required load power.

Although the methods of the first and second categories are beneficial for efficiency optimization, their main drawback is the need for communication links among the units, which require expensive infrastructure especially in remote areas, may lead to system instability in case of communication disconnection, and decrease the system reliability due to time delays and data dropouts that could cause oscillations and even collapse of the system [59–62].

1.2.3 Droop-Based Methods

The third category is based on the droop control strategy, which has not been fully investigated in the literature. Optimal conditions to obtain the maximum system efficiency are derived using Lagrange multiplier method in [63], where the droop parameters of the inverters are retuned to adjust the power sharing among the inverters

and increase the overall efficiency. A similar adaptive droop strategy is proposed in [64], where the authors improve the method of [63] by incorporating both active and reactive powers and achieving optimal reactive power sharing, using a dynamic impedance compensation loop.

Despite the benefits of the aforementioned droop-based methods, the methods have several drawbacks, such as the optimal system efficiency dependency on the system component variations, efficiency improvement for nonidentical converter cases only, and the lack of a clear strategy to optimally turn on and off the inverters at light loads.

1.2.4   Proposed Strategy for Efficiency Improvement

Traditionally, the droop control method has been used to share the load power demand among parallel inverters. The most common approach in droop strategy is that the inverters should share the power proportional to their power ratings. For instance, if the full-load power of an inverter is twice the full-load power of another inverter, the power injection of the former is twice the power injection of the latter. The mentioned approach, however, leads to an inefficient power sharing especially at light loads, where the inverters should operate at a low power that corresponds to a low efficiency according to the typical efficiency curve of an inverter. Fig. 1.4(a) shows three parallel GFM inverters connected to a light load, where the power sharing among the inverters is based on the conventional droop method, and all inverters are supplying a low amount of power. However, as depicted in Fig. 1.4(b), if the power sharing among the inverters is modified such that only one of the inverters supplies the load and the others do not share any power, the power of the load-supplying inverter will be kept within a proper range corresponding to a high efficiency. Therefore, the overall efficiency will be higher than the case where all of the inverters supplied the load. Nevertheless, none of the inverters can operate within the desired power range
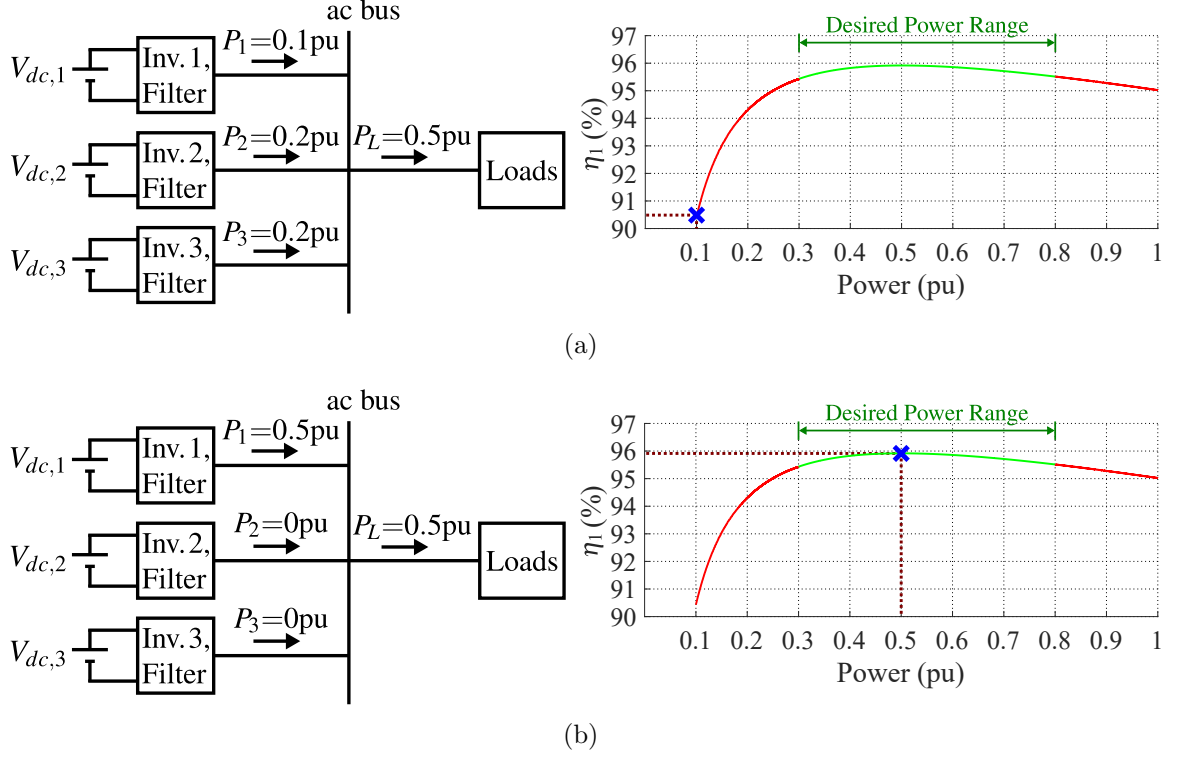
Figure 1.4: Power sharing of three parallel GFM inverters in the (a) conventional droop and (b) modified droop strategy.

at very-light load situations, while the efficiency improvement can be more significant at such loads if a minimum number of inverters supply the loads. Therefore, the online inverters in the system should be detected and the inverter with the lowest power rating should supply the load solely to achieve a higher efficiency.

1.3 Online-Inverter Detection and Efficiency Improvement

As discussed earlier, to achieve a higher system efficiency at very-light loads, each inverter should be able to detect and interact with other online inverters in the system and the unnecessary inverters should be turned off. The interaction among parallel inverters can be realized through communication-based or decentralized schemes

11

which are explained below:

1.3.1 Communication-Based Schemes

Conventionally, centralized schemes are used for continuous communication among inverters to ensure an optimized operation. However, such schemes rely on a central controller, which is a single point of failure. Moreover, the communication system requires additional infrastructure and regular maintenance [65, 66]. In another approach, wireless monitoring and diagnostic systems are used to optimize power systems management [67]. Although such systems provide more reliability and efficiency compared with the centralized schemes, they still require transmitters and receivers at different stages, which need regular maintenance [68]. Furthermore, possible time delays and data dropouts might cause oscillations in the system due to the low bandwidth of such communication systems.

1.3.2 Decentralized Schemes

In decentralized approaches, there is no need for communication facilities, and the interactions among the inverters are realized through variation of the line voltage or frequency [69]. While in dc microgrids the voltage signaling methods are mostly adopted, in ac microgrids the frequency is commonly used instead of voltage due to higher signaling accuracy [70, 71]. A voltage injection method is presented in [68], where a signal with a specific frequency is injected into the ac bus to determine the presence of particular DG units. A similar approach is employed in [72], where a coordination structure is proposed for islanded ac microgrids to control the energy storage systems based on a bus-signaling method that ensures the DGs have information regarding the microgrid operation. Moreover, frequency bus-signaling schemes are used in [69, 73] for standalone microgrids comprising of energy storage and PV systems to ensure that the energy storage systems do not charge or discharge beyond

a particular limit.

1.3.3 Proposed Online-Inverter Detection Method

Frequency is a global variable among parallel GFM inverters operating in standalone mode. Therefore, if inverters make any changes to their droop no-load frequencies, the new system frequency at steady-state conditions can be measured by every inverter. As a result, inverters can interact with each other by applying certain deviations to the frequency using the droop equations. By adopting the mentioned method, the online inverters can be detected through applying two small pulses to the no-load frequency of each inverter, and computing the corresponding frequency deviation ratio. It is worth mentioning that the pulse amplitudes are designed such that the frequency deviation ratio is a unique number for every set of online inverters.

The proposed online-inverter detection (OID) method can be used to detect the online inverters at very-light loads and select a minimum number of inverters with the lowest rated powers to supply the loads and improve the overall system efficiency, as discussed in Section 1.2. Owing to the modularity of the OID, if new inverters should be installed in the system, the existing inverters do not need to be reprogrammed. Furthermore, there is no single point of failure since the OID considers all of the possible online inverter cases, and remains operational even if some of the inverters become offline.

1.4 Thesis Objectives

The main objective of this thesis is to propose a decentralized, modular, and reliable modified droop method to improve the overall system efficiency of parallel GFM inverter systems. To achieve this goal, a droop-based control system is proposed to adjust the power sharing among parallel inverters such that the active power of

each inverter is maintained within a proper range corresponding to a high efficiency. Appropriate state-space models and control design procedures are developed for the inverter controllers. Moreover, a communicationless online-inverter detection (OID) method is developed to detect the online inverters in specific light-load situations, and select a minimum number of inverters with the lowest rated powers to supply the loads to obtain a higher system efficiency. Briefly, the main objectives of this thesis are:

1. To derive a state-space model for a single-phase inverter operating in standalone mode and to propose a nested-loop control structure for the inverter based on the linear quadratic tracking optimal control method to achieve proper reference tracking performance and disturbance rejection.

2. To propose and develop a decentralized modified droop strategy to improve the overall system efficiency of parallel GFM inverters by maintaining the output power of the inverters within a desired range by reducing the power of the unnecessary inverters to zero.

3. To conduct a stability verification of the system within the designed operating range of the no-load frequencies of the inverters to ensure that the proposed control system operates in a stable region.

4. To propose a communicationless online-inverter detection method to detect the online inverters at specific light-load conditions such that a minimum number of inverters with the lowest rated powers can supply the loads and a higher system efficiency is achieved.

5. To verify the system design and analysis using simulation and experimental results.

1.5 Thesis Outline

Chapter 2 introduces a state-space model and nested-loop control structure for a single-phase inverter operating in standalone mode. The control system includes current, voltage, and harmonic rejection control loops, and is designed based on the linear quadratic tracking (LQT) optimal control method. According to the load types, two design procedures are presented for the control system. The first design considers the harmonics controller in the design procedure such that in cases where nonlinear loads are connected to the system, the unwanted harmonics are rejected. The first design is also suitable for linear loads. The second design ignores the harmonics controller in the design procedure, which makes it more simple and suitable for only linear loads. Simulation results verify the satisfactory performance of both designs.

Chapter 3 presents a modified droop strategy to enhance the system efficiency of parallel GFM inverters by adjusting the inverters power sharing such that an optimal number of inverters process fractions of the power demand resulting in a higher efficiency considering the efficiency curve of the inverters. A parallel inverter system comprised of three single-phase inverters is studied, modeled, and designed in this chapter. After deriving the state-space models of the control system components, the proposed method is described by considering the efficiency curve of a single inverter. Then, the proposed controller and different system operating modes are discussed. Furthermore, the system parameters are designed, and the stability of the system within the designed operating range of the no-load frequencies is verified. Ultimately, experimental results are provided to validate the proposed method.

In Chapter 4, an online-inverter detection (OID) method is proposed such that each inverter can detect the other online inverters in very-light load situations by applying two temporary pulses to the no-load frequency. As a result, a minimum number of inverters with the lowest rated powers solely supply the loads while operating at higher power levels and thus, at a higher efficiency in comparison with

the conventional proportional power sharing. To investigate the effectiveness of the method, the OID is integrated with the proposed control system in Chapter 3, and applied to the corresponding three-inverter system. It is observed that the OID features the advantages of parallel inverters such as modularity, flexibility, and reliability. Therefore, if new inverters are added to the system, the existing inverters do not need to be reprogrammed, and there is also no single point of failure. Elaborate simulation and experimental results are provided to assess the performance of the control system including the OID in improving the system efficiency.

Finally, the thesis is concluded in Chapter 5 and suggestions for the future work of this research are presented.

Chapter 2

Single Inverter Control

2.1   Introduction

This chapter proposes a state-space model and a nested-loop control system for a single-phase inverter operating in standalone mode. Based on the load types, two different control designs are presented. The first design which is suitable for both nonlinear and linear loads, includes harmonics controller in the design procedure such that if nonlinear loads are connected to the system, the unwanted harmonics are rejected. The second design, however, is more simple and ignores the harmonics controller in the design procedure, which makes it suitable for linear loads, and it will be used in the next chapters of the thesis. Simulation results verify the satisfactory performance of both designs.

2.2   System Description

As depicted in Fig. 2.1, the circuit configuration of the system consists of a single-phase inverter that is connected to the loads via an LCL filter. The control structure of the inverter is chosen as a nested-loop control system to provide protection against overcurrents and shape the current dynamics as well as voltage dynamics. Further-
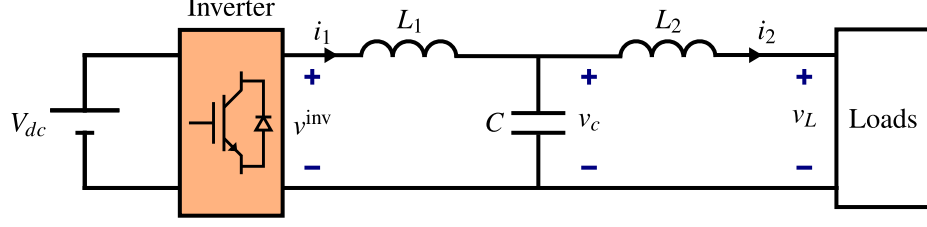
Figure 2.1: Circuit configuration of a single-phase inverter operating in standalone mode.
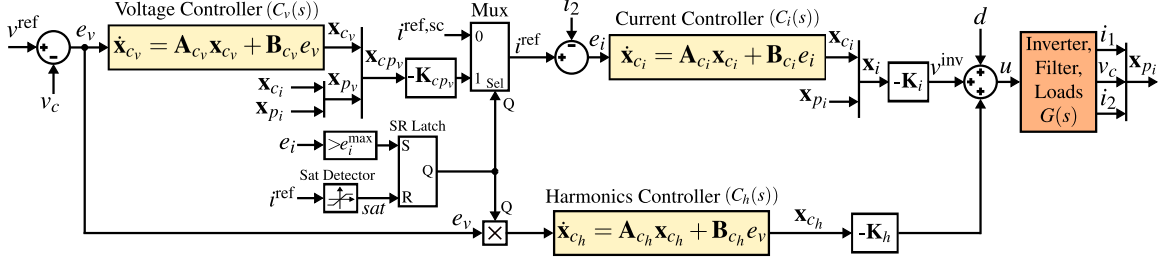
Figure 2.2: Nested-Loop control system of the inverter.

more, the nested-loop structure enables voltage harmonic rejection by incorporating harmonic rejection compensators. Hence, the control system of the inverter, shown in Fig. 2.2, includes current, voltage, and harmonics control loops. Moreover, an SR latch is needed to protect the system against overcurrents. When there is an overcurrent or the load is shorted, the inverter current starts to increase until it reaches the maximum allowable current, which enables the saturation signal, sat. The saturation signal resets the SR latch so that the harmonics loop is removed. The output of the SR latch Q is also the selector of a multiplexer that removes the voltage loop to protect the system in case of faults. Once the fault is over, the current error e_i increases which eventually sets Q to one and the control loops return to normal operation.

The control system is designed based on the linear quadratic tracking (LQT) optimal control method [33, 48]. The LQT method converts the tracking and disturbance rejection problem to a regulating problem that can be solved using the well-known linear quadratic regulator (LQR) method. Since the cost function of this method includes all of the system states, the weights associated with the states can be designed

18

in a systematic way to ensure a high-quality performance. Additionally, the LQT method offers high robustness against system parameter uncertainties and nonlinearities.

2.3 State-Space Modeling

In the following, state-space models of the current and voltage control loops are derived. It is worth mentioning that the harmonics controller is considered as a part of the voltage control loop. Hereinafter, the indices "i", "v", "h", "p", "c", and "L" represent the signals and variables of the current control loop, voltage control loop, harmonics, plants, controllers, and loads.

2.3.1 Current Control Loop

For the current controller, the inverter and LCL filter are considered as the plant. The state-space equation of the current control loop plant is given by:

$$\dot{\mathbf{x}}_{p_i} = \mathbf{A}_{p_i}\mathbf{x}_{p_i} + \mathbf{B}_{p_i}v^{\text{inv}} + \mathbf{B}_{p_L}v_L, \tag{2.1}$$

where $\mathbf{x}_{p_i} = [i_1\ v_c\ i_2]^T$, and i_1, v_c, i_2, and v^{inv} refer to the current of the inverter-side inductor L_1, voltage of the capacitor C, current of the load-side inductor L_2, and inverter voltage, respectively. Moreover, $\mathbf{A}_{p_i}$, $\mathbf{B}_{p_i}$, and $\mathbf{B}_{p_L}$ are defined as follows:

$$\mathbf{A}_{p_i}=\begin{bmatrix} 0 & \frac{-1}{L_1} & 0 \\ \frac{1}{C} & 0 & \frac{-1}{C} \\ 0 & \frac{1}{L_2} & 0 \end{bmatrix}, \mathbf{B}_{p_i}=\begin{bmatrix} \frac{1}{L_1} \\ 0 \\ 0 \end{bmatrix}, \mathbf{B}_{p_L}=\begin{bmatrix} 0 \\ 0 \\ \frac{-1}{L_2} \end{bmatrix}. \tag{2.2}$$

The current controller is assumed to be a resonant controller with the following state-space equation:

$$\dot{\mathbf{x}}_{c_i} = \mathbf{A}_{c_i}\mathbf{x}_{c_i} + \mathbf{B}_{c_i}e_i, \tag{2.3}$$

19

where $\mathbf{x}_{c_i}$ is the state vector of the current controller and $e_i = i^{\text{ref}} - i_2$ is the current tracking error. Moreover, considering the nominal frequency of the inverter as $\omega_{\text{nom}} = 2\pi 60 \text{ rad/s}$, $\mathbf{A}_{c_i}$ and $\mathbf{B}_{c_i}$ are:

$$\mathbf{A}_{c_i} = \begin{bmatrix} 0 & -\omega_{\text{nom}} \\ \omega_{\text{nom}} & 0 \end{bmatrix}, \ \mathbf{B}_{c_i} = \begin{bmatrix} 0 \\ 1 \end{bmatrix}. \tag{2.4}$$

Assuming $\mathbf{x}_i = [\mathbf{x}_{c_i} \ \mathbf{x}_{p_i}]^T$ as the current control loop state vector and $v^{\text{inv}} = -\mathbf{K}_i \mathbf{x}_i$, where $\mathbf{K}_i$ is the current control loop gain vector, (2.1)-(2.4) form the state-space equation of the current control loop as:

$$\dot{\mathbf{x}}_i = \left(\mathbf{A}_i - \mathbf{B}_i^{v^{\text{inv}}} \mathbf{K}_i \right) \mathbf{x}_i + \mathbf{B}_i i^{\text{ref}} + \mathbf{B}_{v_L} v_L,$$

$$\mathbf{A}_i = \begin{bmatrix} \mathbf{A}_{c_i} & -\mathbf{B}_{c_i} \mathbf{C}_{p_i} \\ \mathbf{0} & \mathbf{A}_{p_i} \end{bmatrix}, \mathbf{B}_i^{v^{\text{inv}}} = \begin{bmatrix} \mathbf{0} \\ \mathbf{B}_{p_i} \end{bmatrix}, \mathbf{B}_{v_L} = \begin{bmatrix} \mathbf{0} \\ \mathbf{B}_{p_L} \end{bmatrix}, \mathbf{B}_i = \begin{bmatrix} \mathbf{B}_{c_i} \\ \mathbf{0} \end{bmatrix}, \mathbf{C}_{p_i} = \begin{bmatrix} \mathbf{0} & 1 \end{bmatrix}, \tag{2.5}$$

where $\mathbf{K}_i$ is optimally designed using the LQT method. It is worth remarking that the current control loop is designed at the fundamental frequency. Therefore, the harmonics resonant controller does not have any impact on the design of the current loop since the controller is tuned at harmonic frequencies. Nevertheless, the harmonics controller is considered as a part of the voltage loop and its effect on the poles of the entire system is taken into account.

2.3.2 Voltage Control Loop

For the voltage control loop, the current loop represented by (2.5) is considered as a new plant with state variables $\mathbf{x}_{p_v} = [\mathbf{x}_{c_i} \ \mathbf{x}_{p_i}]^T$, and state matrices $\mathbf{A}_{p_v} = \mathbf{A}_i - \mathbf{B}_i^{v^{\text{inv}}} \mathbf{K}_i$, $\mathbf{B}_{p_v} = \mathbf{B}_i$. The voltage controller is a resonant controller, with the following state-space equation:

$$\dot{\mathbf{x}}_{c_v} = \mathbf{A}_{c_v} \mathbf{x}_{c_v} + \mathbf{B}_{c_v} e_v, \tag{2.6}$$

where $\mathbf{x}_{c_v}$ is the state vector of the voltage controller, and $e_v = v^{\text{ref}} - v_c$ denotes the voltage tracking error. Furthermore, $\mathbf{A}_{c_v}$ and $\mathbf{B}_{c_v}$ are equal to $\mathbf{A}_{c_i}$ and $\mathbf{B}_{c_i}$ in (2.4), respectively.

In addition to the voltage controller, a selective harmonics controller is utilized in the voltage control loop to reject the harmonics caused by the disturbance d, as illustrated in Fig. 2.2. The disturbance d represents the nonlinearities of the loads. Similar to the voltage controller, the harmonics controller is a resonant controller tuned at selected harmonics, i.e. 3rd, 5th, and 7th. Hence, the state-space equation of the harmonics controller is given by:

$$\dot{\mathbf{x}}_{c_h} = \mathbf{A}_{c_h}\mathbf{x}_{c_h} + \mathbf{B}_{c_h}e_v,$$

$$\mathbf{A}_{c_h} = \begin{bmatrix} \mathbf{A}_{c_{h_3}} & \mathbf{0} & \mathbf{0} \\ \mathbf{0} & \mathbf{A}_{c_{h_5}} & \mathbf{0} \\ \mathbf{0} & \mathbf{0} & \mathbf{A}_{c_{h_7}} \end{bmatrix}, \ \mathbf{B}_{c_h} = \begin{bmatrix} \mathbf{B}_{c_{h_3}} \\ \mathbf{B}_{c_{h_5}} \\ \mathbf{B}_{c_{h_7}} \end{bmatrix},$$

$$\mathbf{A}_{c_{h_3}} = \begin{bmatrix} 0 & -3\omega_{\text{nom}} \\ 3\omega_{\text{nom}} & 0 \end{bmatrix}, \ \mathbf{A}_{c_{h_5}} = \begin{bmatrix} 0 & -5\omega_{\text{nom}} \\ 5\omega_{\text{nom}} & 0 \end{bmatrix}, \ \mathbf{A}_{c_{h_7}} = \begin{bmatrix} 0 & -7\omega_{\text{nom}} \\ 7\omega_{\text{nom}} & 0 \end{bmatrix}$$

$$\mathbf{B}_{c_{h_3}} = \mathbf{B}_{c_{h_5}} = \mathbf{B}_{c_{h_7}} = \begin{bmatrix} 0 \\ 1 \end{bmatrix},$$

$$(2.7)$$

where $\mathbf{x}_{c_h} = [\mathbf{x}_{c_{h_3}} \ \mathbf{x}_{c_{h_5}} \ \mathbf{x}_{c_{h_7}}]^T$ is the state vector of the harmonics controller.

According to the control system structure shown in Fig. 2.2, by considering the gain vectors as part of controllers, the following transfer functions from the reference (v^{ref}) and disturbance (d) to the output (v_c) are obtained:

$$T_{\text{ref}} = \frac{V_c(s)}{V^{\text{ref}}(s)} = \frac{(C_v(s).C_i(s) + C_h(s))G(s)}{1 + (C_v(s).C_i(s) + C_h(s))G(s)},$$

$$T_D = \frac{V_c(s)}{D(s)} = \frac{G(s)}{1 + (C_v(s).C_i(s) + C_h(s))G(s)},$$

$$(2.8)$$

where $C_v(s)$, $C_i(s)$, $C_h(s)$, and $G(s)$ refer to the voltage controller, current controller, harmonics controller, and the current control loop plant as shown in Fig. 2.2. Since $C_v(s)$ and $C_i(s)$ are resonant controllers, they have an infinite gain at the fundamental frequency. Similarly, $C_h(s)$ has an infinite gain at the harmonic frequencies. Therefore, T_{ref} has a unity gain and T_D is zero at the fundamental and harmonic frequencies, respectively. As a result, the control system tracks the fundamental and harmonic components of the reference v^{ref} and rejects them from the disturbance d.

Ultimately, assuming $\mathbf{x}_v = [\mathbf{x}_{c_h} \ \mathbf{x}_{c_v} \ \mathbf{x}_{p_v}]^T$, (2.5)-(2.7) are augmented to form the state-space equation of the voltage control loop as:

$$\dot{\mathbf{x}}_v = \left(\mathbf{A}_v - \mathbf{B}_v^{i^{\text{ref}}} \mathbf{K}_v \right) \mathbf{x}_v + \mathbf{B}_v v^{\text{ref}},$$

$$\mathbf{A}_v = \begin{bmatrix} \mathbf{A}_{c_h} & \mathbf{0} & -\mathbf{B}_{c_h}\mathbf{C}_{p_v} \\ \mathbf{0} & \mathbf{A}_{c_v} & -\mathbf{B}_{c_v}\mathbf{C}_{p_v} \\ \mathbf{0} & \mathbf{0} & \mathbf{A}_{p_v} \end{bmatrix}, \mathbf{B}_v^{i^{\text{ref}}} = \begin{bmatrix} \mathbf{0} \\ \mathbf{0} \\ \mathbf{B}_{p_v} \end{bmatrix}, \mathbf{B}_v = \begin{bmatrix} \mathbf{B}_{c_h} \\ \mathbf{B}_{c_v} \\ \mathbf{0} \end{bmatrix}, \mathbf{C}_{p_v} = \begin{bmatrix} 0 & 0 & 0 & 1 & 0 \end{bmatrix}, \quad (2.9)$$

where $\mathbf{K}_v = [\mathbf{K}_h \ \mathbf{K}_{cp_v}]^T$ is the voltage control loop gain vector and is optimally designed using the LQT method.

2.4 Controller Design

The controllers are designed in two different scenarios. In the first scenario, a nonlinear load is connected to the system to evaluate the performance of the harmonics controller in rejecting the unwanted harmonics in the voltage. The second scenario involves linear loads that do not produce harmonics, and thus, the harmonics controller is not considered in this case.
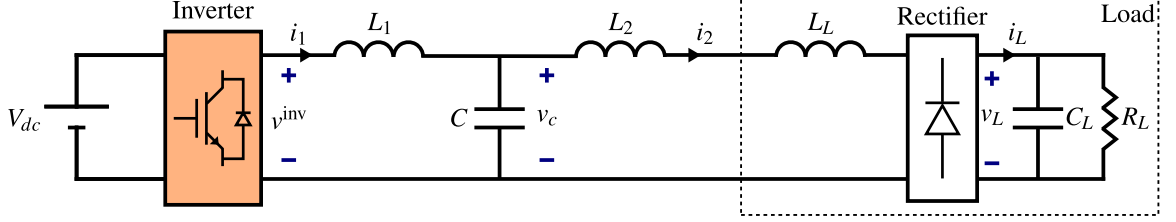
Figure 2.3: Circuit configuration of a single-phase inverter connected to a nonlinear load.

Table 2.1: System parameters.

Parameter	Value	Parameter	Value
V_{dc}	200 V	P^{fl}	1 kW
ω_{nom}	$2\pi 60$ $\mathrm{rad/s}$	V_{nom}	$120\sqrt{2}$ V
L_1	2 mH	L_2	2 mH
C	2.2 µF	L_L	5 mH
C_L	3 mF	R_L	38 Ω

2.4.1 Controller Design with Harmonics Controller

The circuit configuration of the case study in the first scenario is depicted in Fig. 2.3. The nonlinear load contains an inductive filter L_L and a full-bridge rectifier connected to a capacitor C_L and resistor R_L. The parameters of the system are shown in Table 2.1. The controllers are designed using the LQT method to obtain proper tracking response, disturbance rejection, and high-quality current and voltage. The details of the LQT design procedure can be found in [33, 48]. A summary of the method is provided below:

2.4.1.1 Current Controller Design

The current control loop gain vector $\mathbf{K_i}$ is designed based on (2.1)-(2.5). Matrix $\mathbf{Q_1} = \mathrm{diag}[q_{11} \ q_{12} \ ... \ q_{15}]$ is considered as the weight matrix of the LQR cost function $J = \int_0^\infty \left(\mathbf{z^T Q_1 z} + v^2 \right) dt$, where $\mathbf{z}$ and v refer to the transformed state vector $\mathbf{x_i}$ and transformed control signal v^{inv} from the LQT problem, respectively. Moreover, q_{11} and
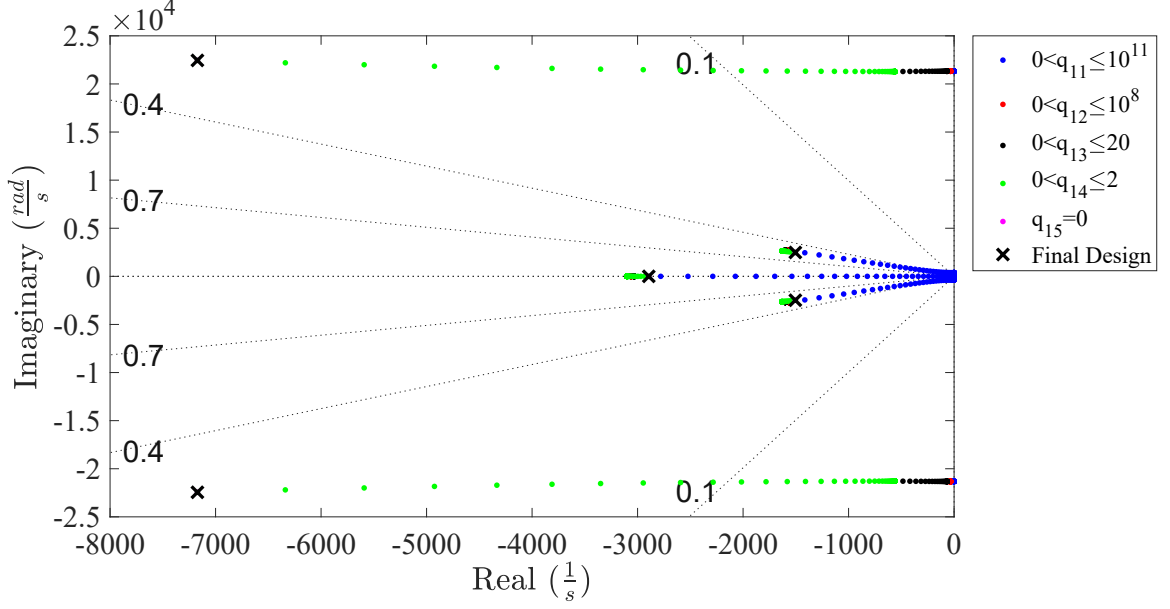
Figure 2.4: Designing the current control loop poles using the LQT method.

q_{12} are the weight factors of the current error e_i and $\frac{de_i}{dt}$, respectively. Additionally, q_{13}, q_{14}, and q_{15} are the weight factors of the current loop plant state variables, i.e. i_1, v_c, and i_2. By solving the LQR problem, the poles of the current control loop can be mapped to appropriate places in the s-plane. Fig. 2.4 shows the displacement and final locations of the current control loop poles by variations in the weight factors. As a result, the current control loop gain vector is obtained by:

$$\mathbf{K_i} = [3.04 \times 10^5 \ \text{-}8.6 \times 10^4 \ 40.5 \ 0.9 \ \text{-}9.3] \tag{2.10}$$

2.4.1.2 Voltage and Harmonics Controllers Design

The voltage and harmonics controllers are designed using (2.6)-(2.9). While the weight matrix of the voltage control loop is defined as $\mathbf{Q_2} = \mathrm{diag}[q_{2_1} \ q_{2_2} \ ... \ q_{2_{13}}]$, the design procedure of the voltage controller is similar to the current controller. In matrix $\mathbf{Q_2}$, q_{21} to q_{26} correspond to the state variables of the harmonics controller. Moreover, the other weight factors correspond to state variables of the voltage controller $\mathbf{x}_{c_v}$ and voltage loop plant $\mathbf{x}_{p_v}$, respectively. Fig. 2.5 depicts the displacement and final

24
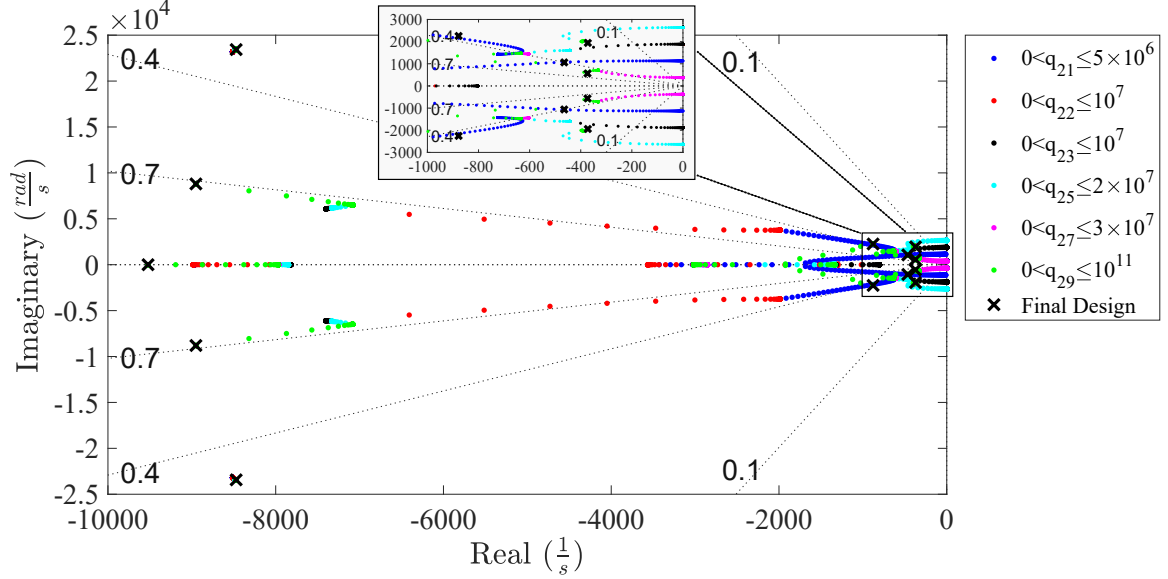
Figure 2.5: Designing the voltage control loop poles using the LQT method.

locations of the voltage control loop poles with respect to variations in the weight factors. It is worth remarking that only the nonzero weight factors are presented in the figure. Consequently, the voltage control loop gain vector is given by:

$$\mathbf{K_v} = [2557.4 \ \text{-}2908.55 \ 2863.02 \ \text{-}1342.8 \ 4299.36 \ 1231.04 \ 3091.8$$
$$\text{-}4521.16 \ \text{-}136102.88 \ 21096.35 \ 3.98 \ 0.19 \ \text{-}7.59]$$

(2.11)

2.4.1.3 Simulation Results

The inverter system with the parameters shown in Table 2.1 and the designed controllers is simulated to evaluate the performance of the control system in rejecting the unwanted harmonics and supplying the load. Fig. 2.6(a) illustrates the tracking and harmonic rejection performances of the control system in the LCL filter capacitor voltage. Furthermore, the voltage and current of the load are shown in Fig. 2.6(b) and Fig. 2.6(c), respectively. To further investigate the performance of the harmonics controller, the harmonic spectrum of the LCL filter capacitor voltage v_c is presented in Fig. 2.7. As can be seen from the harmonic spectrum, there is almost no 3rd, 5th, and 7th harmonic components in the voltage, since the mentioned harmonics are

25

rejected by the control system. Moreover, the total harmonic distortion (THD) of v_c is 1.65%, which shows the satisfactory performance of the harmonics controller.
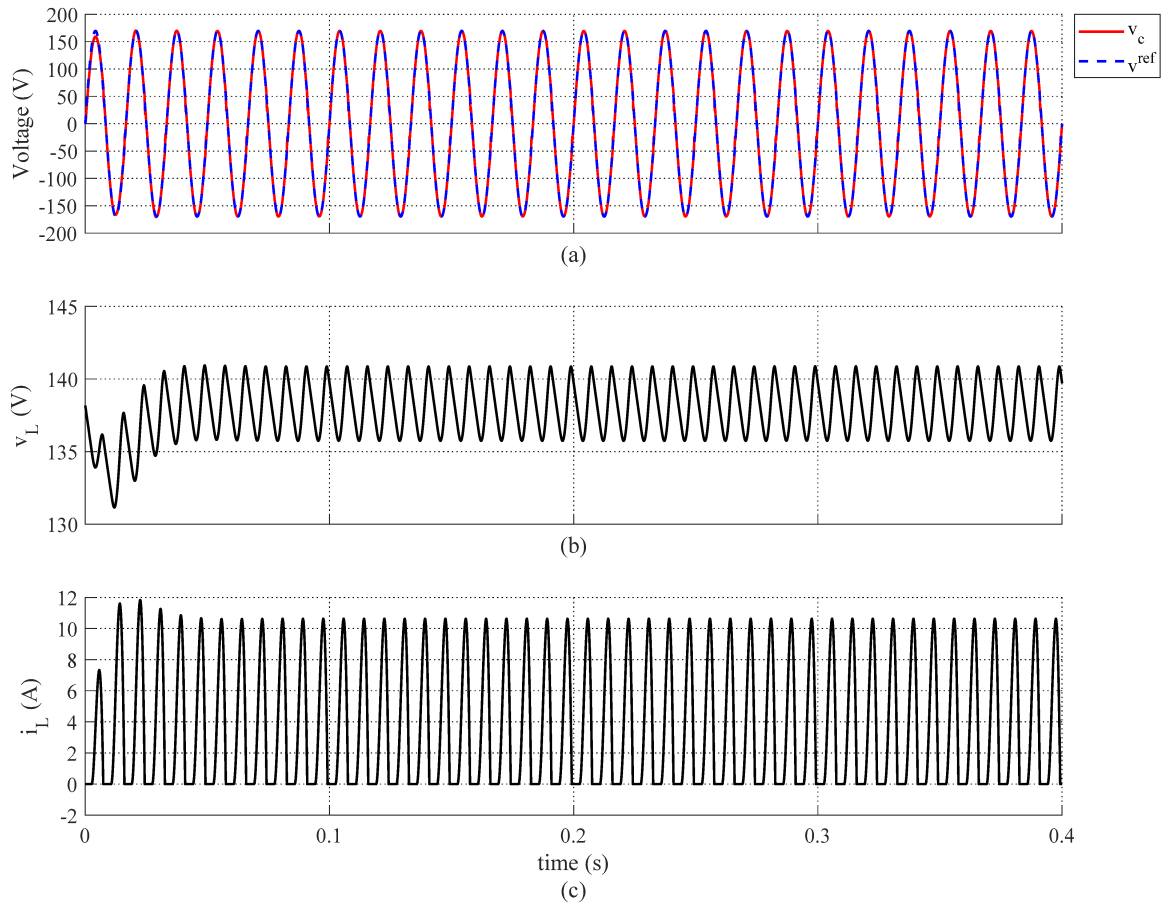
Figure 2.6: Simulation results: (a) LCL filter capacitor voltage (b) load voltage (c) load current.
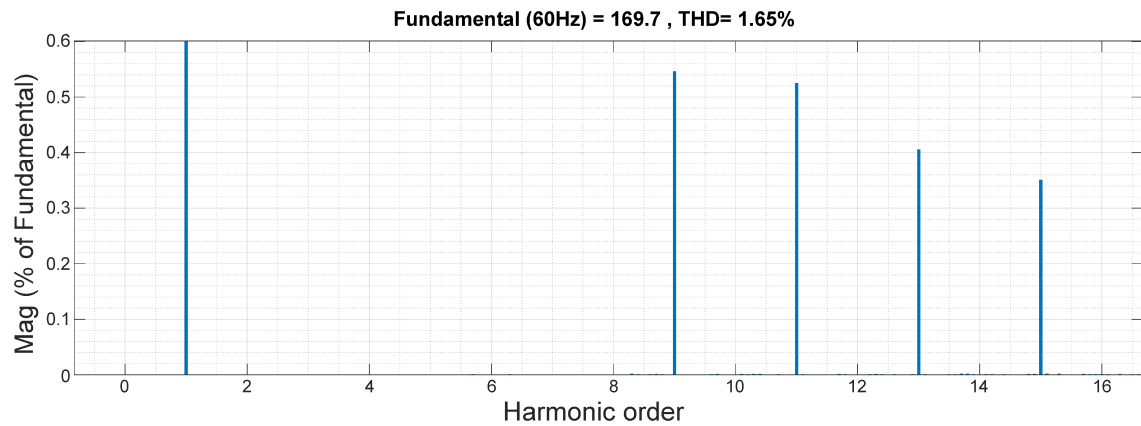
Figure 2.7: Harmonic spectrum of the LCL filter capacitor voltage.

2.4.2 Controller Design without Harmonics Controller

In the second scenario, the controllers are designed only for linear loads, i.e. the harmonics controller is removed. For the sake of simplicity and without loss of generality, the design method presented in the second scenario is selected for the rest of the thesis. Moreover, the controllers are designed with per unit values so that the design procedure can be generalized in the rest of the thesis, where more inverters will be added to the system. The parameters of the system are the same as Table 2.1 except for the load which is a linear resistive load $R_L = 1$ pu. Similar to the first scenario, the controllers are designed using the LQT method [33, 48]. A summary of the method is provided below:

2.4.2.1 Current Controller Design

The current control loop gain vector $\mathbf{K_i}$ is designed based on (2.1)-(2.5). Matrix $\mathbf{Q_1} = \mathrm{diag}[q_{11}\ q_{12}\ ...\ q_{15}]$ is considered as the weight matrix of the LQR cost function $J = \int_0^\infty \left(\mathbf{z^T Q_1 z} + v^2\right) dt$. By solving the LQR problem, the poles of the current control loop can be relocated to desired places in the s-plane. Fig. 2.8 shows the
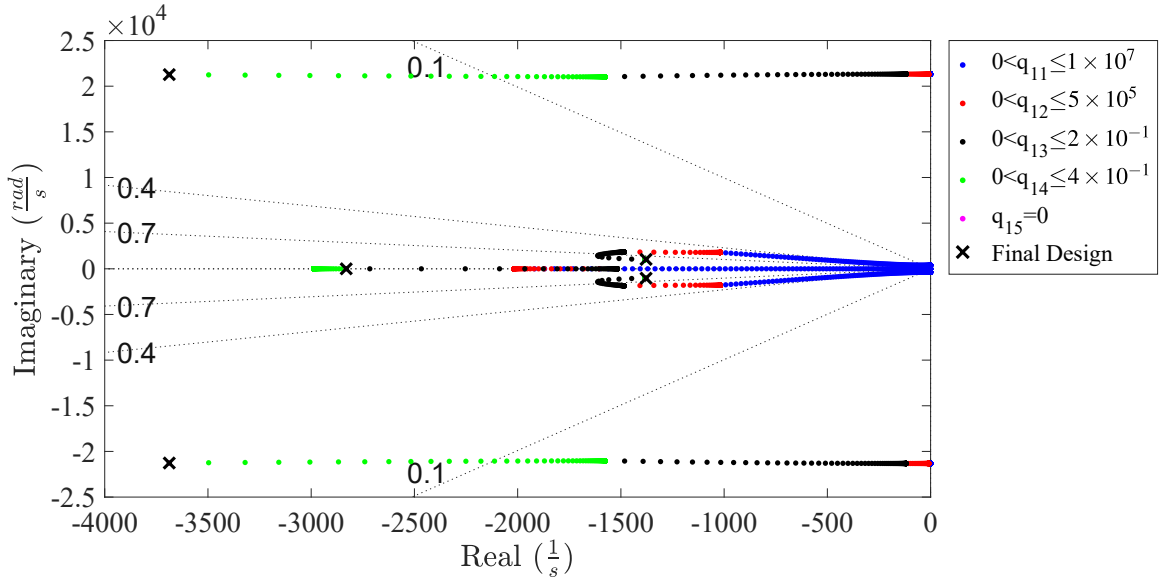
Figure 2.8: Displacement of current control loop poles by variations in weight factors.

displacement and final locations of the current control loop poles by variations in the weight factors. As a result, the current control loop gain vector is obtained by:

$$\mathbf{K_i} = [8.23 \times 10^4 \ \text{-}4.40 \times 10^4 \ 25.92 \ 0.28 \ \text{-}2.26] \tag{2.12}$$

2.4.2.2 Voltage Controller Design

As mentioned earlier, the harmonics controller is not considered as a part of the voltage control loop in the second scenario. The voltage controller is designed using (2.6)-(2.9). The weight matrix of the voltage control loop is defined as $\mathbf{Q_2} = \text{diag}[q_{21} \ q_{22} \ ... \ q_{27}]$, and the design procedure is similar to the current controller. In the weight matrix $\mathbf{Q_2}$, q_{21} and q_{22} correspond to the voltage error e_v and its derivative, respectively. Moreover, the other weight factors correspond to state variables of the voltage loop plant $\mathbf{x}_{p_v}$. Fig. 2.9 depicts the displacement and final locations of the voltage control loop poles with respect to variations in the weight factors. Hence, the voltage control loop gain vector is given by:

$$\mathbf{K_v} = [214.67 \ \text{-}189.47 \ \text{-}4177.11 \ 3044.96 \ 0.14 \ \text{-}1.20 \times 10^{-3} \ \text{-}0.17] \tag{2.13}$$
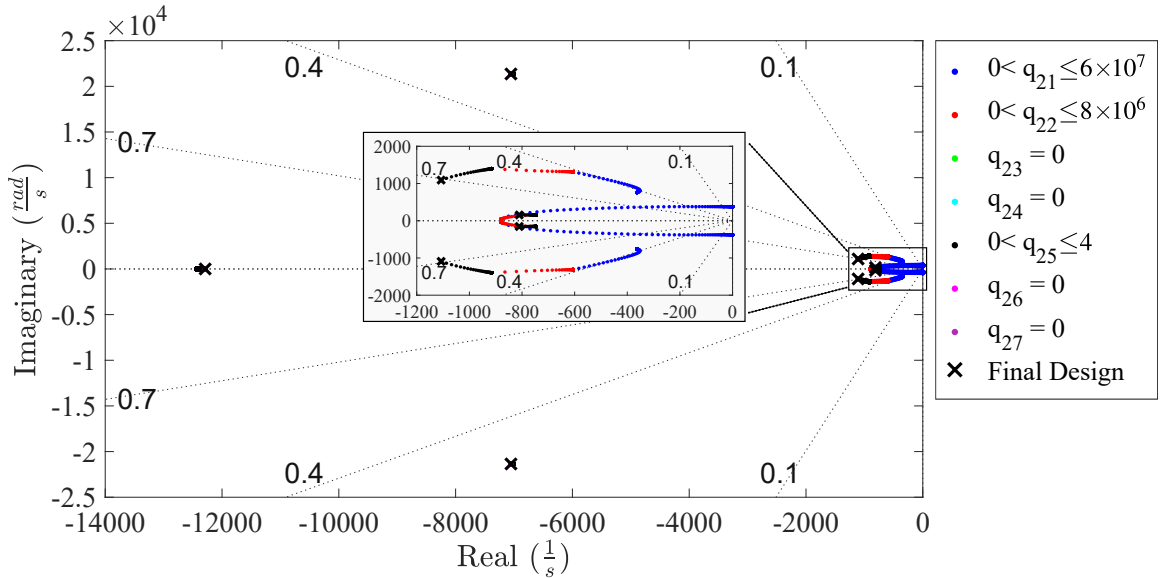
Figure 2.9: Displacement of voltage control loop poles by variations in weight factors.

2.4.2.3 Simulation Results

The inverter system with the designed controllers is simulated to evaluate the performance of the control system. As illustrated in Fig. 2.10, both the voltage and current controllers have satisfactory tracking performances at half and full-load powers, namely 500 W and 1000 W loads. It is also observed that the inverter power injection has a fast and smooth response in case of changes in the load.
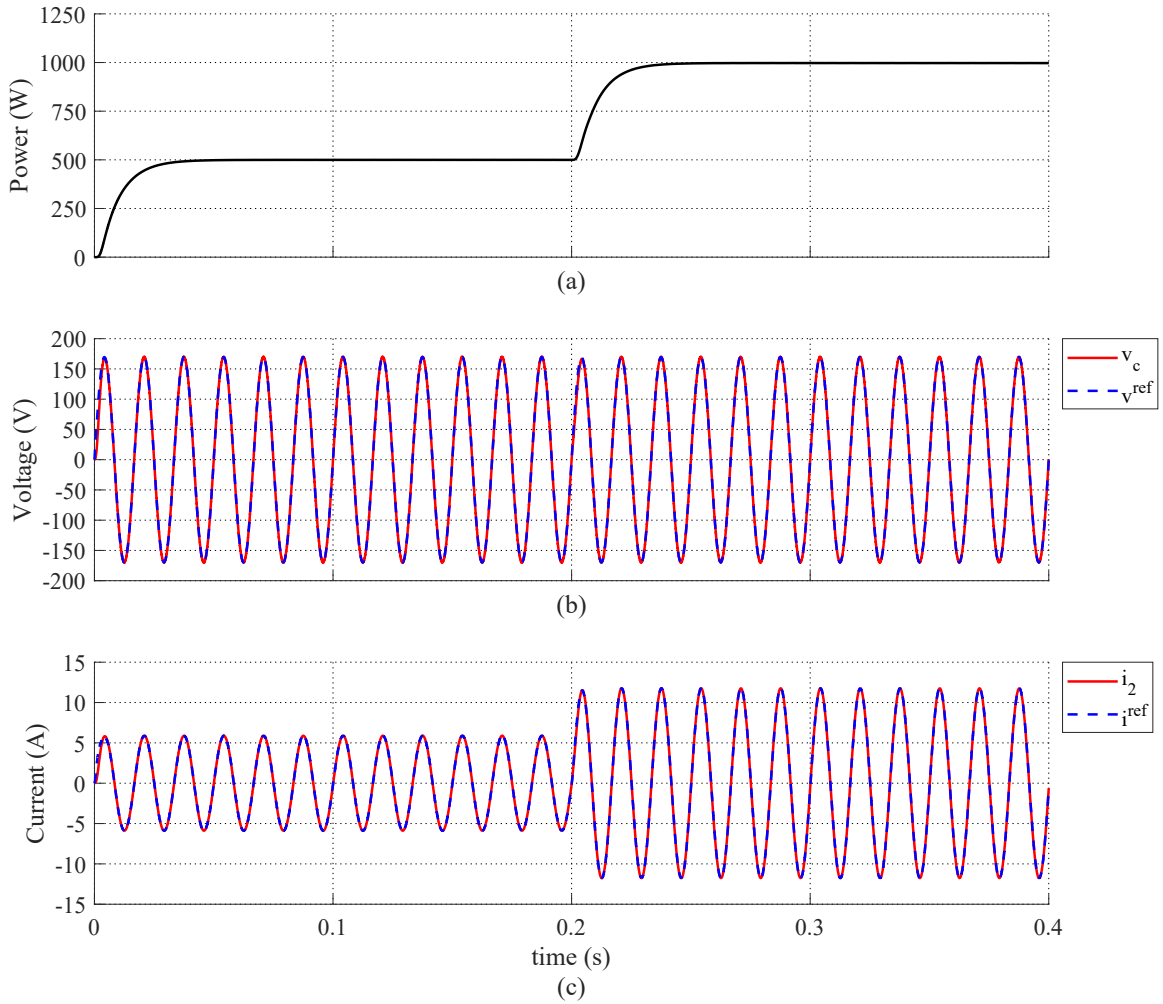
Figure 2.10: Simulation results: (a) inverter power injection (b) LCL filter capacitor voltage (c) load-side inductor current.

2.5 Summary

In this chapter, the modeling and control system design procedure for a single-phase inverter operating in standalone mode is presented, which is based on the linear quadratic tracking (LQT) optimal control method. As the control system has a nested-loop structure, first, the state-space model of the current control loop is obtained. Then, the entire current loop is considered as the plant of the voltage control loop, and the models of the voltage and harmonics controllers are derived. By augmenting the current loop equations with the voltage and harmonics controllers, the state-space model of the voltage control loop is obtained. Afterwards, based on the type of the load connected to the system, two scenarios are considered. In the first one, a nonlinear load is connected to the system that injects unwanted harmonics to the voltage. Therefore, the current and voltage control loops are designed using the LQT method to obtain proper tracking response and disturbance rejection. Simulation results verify the satisfactory performance of the controllers in rejecting the unwanted harmonics. In the second scenario, however, the harmonics controller is removed and the controllers are designed only for linear loads. Simulation results show that the designed control system has a satisfactory performance in tracking both the voltage and current.

Chapter 3

Grid-Forming Inverter System Efficiency Improvement

3.1 Introduction

Parallel GFM inverters are used in many modern applications, and thus, improving the inverter system efficiency plays a key role in energy savings. The conventional droop strategy used for power sharing among inverters, however, leads to a low efficiency especially at light loads, as the low power demand is divided among inverters, forcing them to process a fraction of the low power at a low efficiency according to their efficiency curve, as shown in Fig. 3.1(a). To avoid such operating conditions, a decentralized modified droop strategy is proposed in this chapter to select an optimal number of inverters to process fractions of the power demand that leads to a higher system efficiency considering the efficiency curve of the inverters, as depicted in Fig. 3.1(b). A parallel inverter system including three single-phase inverters with nested-loop control systems is studied, modeled, and designed in this chapter. Moreover, experimental results are provided to verify the performance of the proposed control system. Since one of the system operating modes is explained in Chapter 4,

(a) Load power using the conventional droop method: $P_L = \sum\limits_{k=1}^{3} P_k = 0.5$ pu.

(b) Load power using the proposed method: $P_L = P_1 = 0.5$ pu.
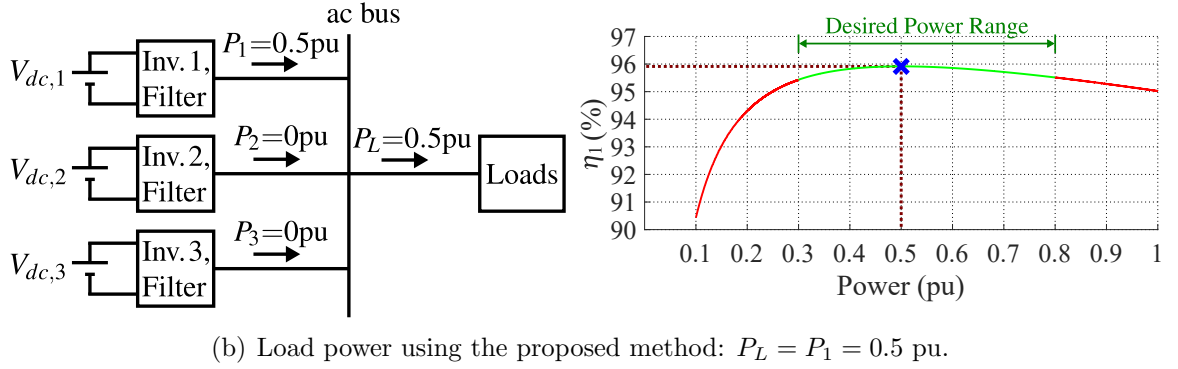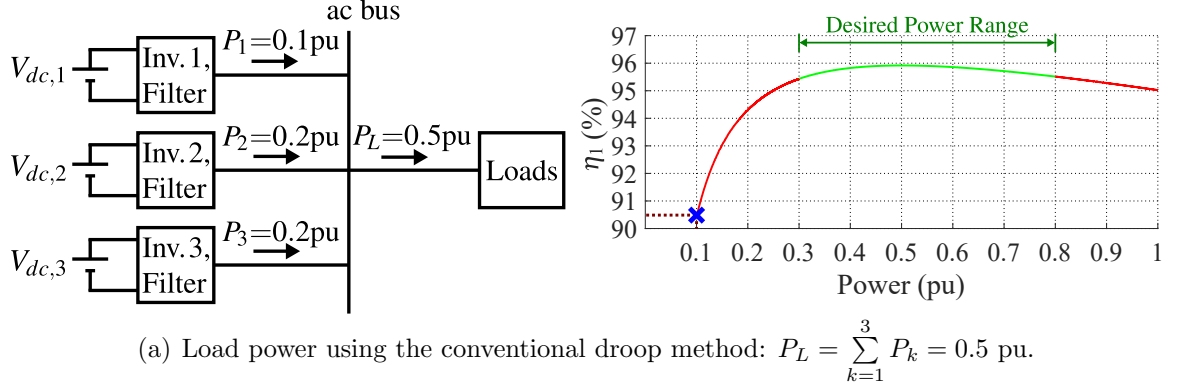
Figure 3.1: Power sharing and inverter efficiency comparison of three parallel GFM inverters in the (a) conventional droop and (b) proposed method.

more detailed simulation and experimental results are provided in the next chapter.

3.2 Droop Control Method

The power sharing among parallel inverters is realized through the droop control strategy without the need of communication links [24, 25, 52]. By assuming an inductive impedance between the inverters and loads, active and reactive powers of each inverter can be controlled by the frequency and amplitude of the inverter output voltage, respectively [23]. Fig. 3.2 depicts the droop characteristics of the kth inverter in a parallel inverter configuration. Thus, the frequency and voltage droop equations are given by:

$$\omega_k = \omega_k^{nl} - m_k P_k, \ V_k = V_k^{nl} - n_k Q_k, \tag{3.1}$$
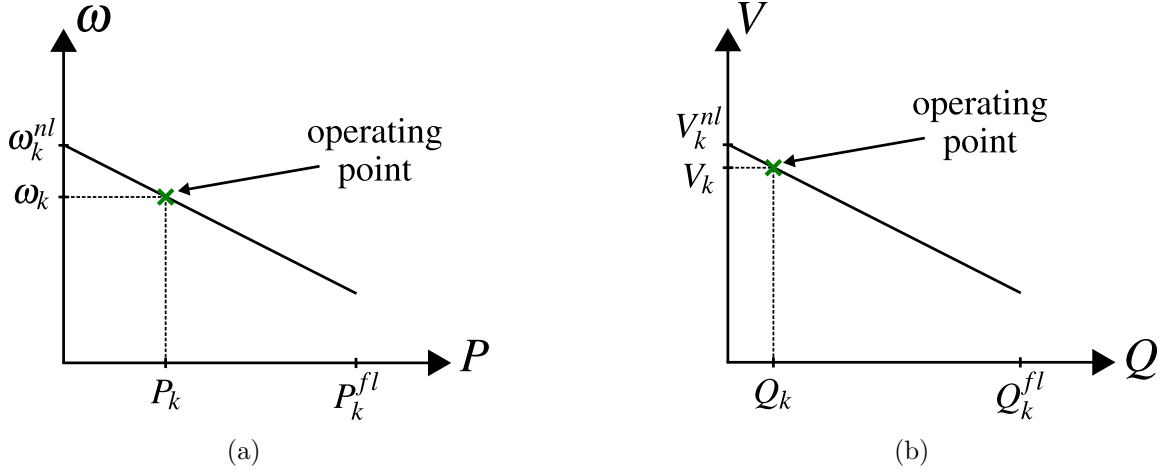
Figure 3.2: Droop characteristics of the kth inverter: (a) frequency-droop curve, and (b) voltage-droop curve.

where ω_k, ω_k^{nl}, m_k, and P_k denote the reference frequency, no-load frequency, frequency-droop coefficient, and filtered active power, respectively. Moreover, V_k, V_k^{nl}, n_k, and Q_k refer to the reference voltage amplitude, no-load voltage amplitude, voltage-droop coefficient, and filtered reactive power, respectively.

3.3 System Configuration and Single Inverter Control System

The parallel GFM inverter system configuration is illustrated in Fig. 3.3. It consists of three parallel single-phase inverters that are connected to the loads via LCL filters. To verify the performance of the proposed method in different scenarios where identical or nonidentical inverters are online in the system, the full-load powers of Inverter 2 and Inverter 3 are assumed to be twice the full-load power of Inverter 1, i.e. $P_3^{fl} = P_2^{fl} = 2P_1^{fl} = 2$ kW.

Each inverter has a decentralized nested-loop control system shown in Fig. 3.4. The inner loops control the voltage and current of the inverter. The outer loops, including the frequency restoration loop, proposed controller, and conventional droop
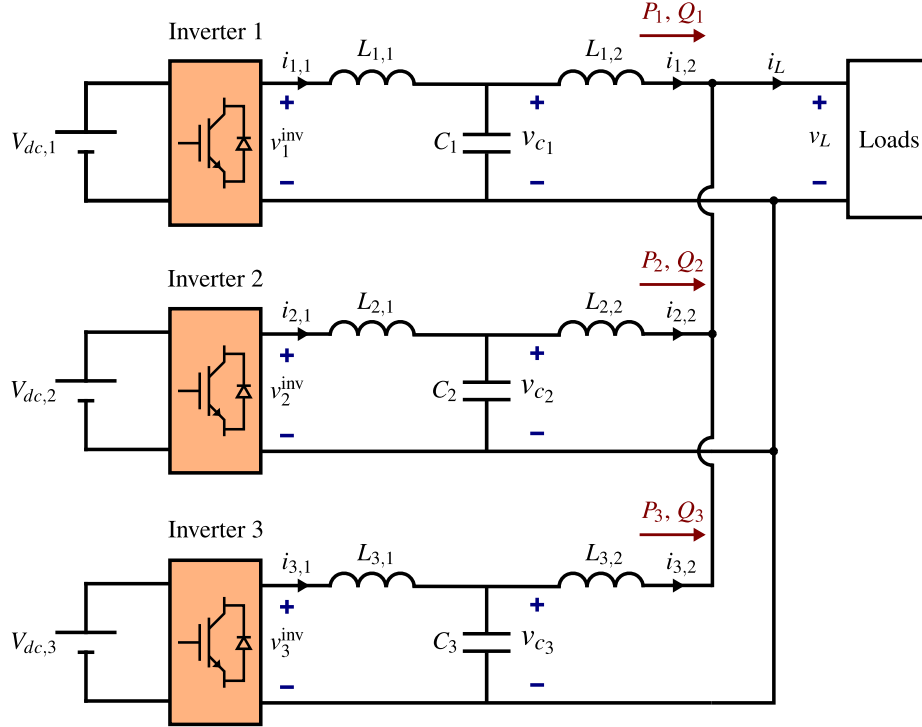
Figure 3.3: parallel GFM inverter system configuration.

controller generate the reference voltage of the inner loops. As depicted in Fig. 3.4, the proposed controller determines the no-load frequency ω_k^{nl} of the droop controller to modify the contribution of the kth inverter in the power sharing. More details on the principles of operations of the proposed controller and how it interacts with other controllers is provided in Section 3.4. In the following, state-space models of the load and k^{th} inverter are derived. Since the models of the voltage and current
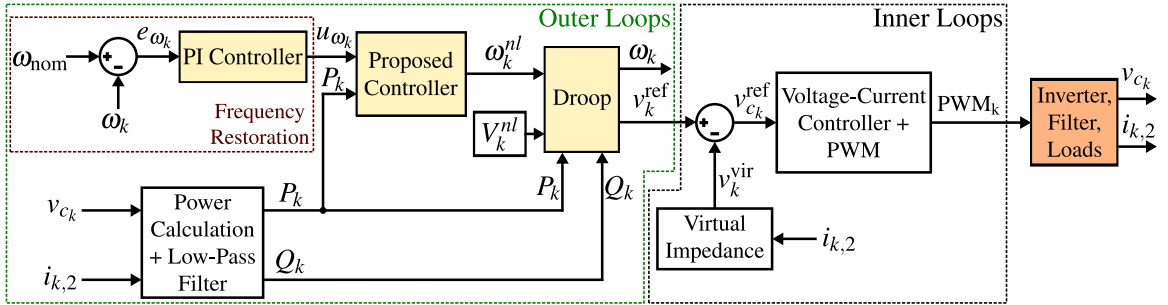
Figure 3.4: Control system structure of the kth inverter.

control loops of the inverter were derived in Chapter 2, their models are not discussed in this chapter. Hereinafter, the index "k" represents the signals and variables of the kth inverter.

3.3.1 System Load

The system load can be a combination of series resistive R_L, inductive L_L, and capacitive C_L components. Therefore, the load voltage is calculated as $v_L = R_L i_L + L_L \frac{di_L}{dt} + v_{c_L}$, where v_{c_L} and i_L are the capacitive part of the load voltage and the load current, respectively, given by:

$$v_{c_L} = \frac{1}{C_L} \int i_L dt, \ i_L = \sum_{k=1}^{3} i_{k,2}. \tag{3.2}$$

According to (3.2) and $\frac{di_{k,2}}{dt} = \frac{v_{c_k} - v_L}{L_{k,2}}$, the load voltage is rewritten as:

$$v_L = \frac{R_L \sum_{k=1}^{3} i_{k,2} + L_L \sum_{k=1}^{3} \frac{v_{c_k}}{L_{k,2}} + v_{c_L}}{1 + L_L \sum_{k=1}^{3} \frac{1}{L_{k,2}}}. \tag{3.3}$$

3.3.2 Virtual Impedance

A virtual impedance L_k^{vir} is used to improve the stability of the system and ensure inductive impedance between the inverter and the loads [22, 74]. Considering $i_{k,2}$ and v_k^{vir} as the input and output of the virtual impedance block, respectively, the voltage drop across the impedance is $v_k^{\text{vir}} = L_k^{\text{vir}} \frac{di_{k,2}}{dt}$.

3.3.3 Low-Pass Filter

A low-pass filter (LPF) is used besides the power calculation block to provide virtual inertia and improve the stability of the inverter similar to virtual synchronous machines [75–78]. For a first-order LPF with the transfer function $G_{lp}(s) = \frac{\omega_{cf}}{s + \omega_{cf}}$, where ω_{cf} is the cut-off frequency, the state-space equations are:

$$\dot{\mathbf{x}}_{lp_k} = \mathbf{A}_{lp_k}\mathbf{x}_{lp_k} + \mathbf{B}_{lp_k}\mathbf{u}_{lp_k}, \ \ \mathbf{y}_{lp_k} = \mathbf{C}_{lp_k}\mathbf{x}_{lp_k},$$
$$\mathbf{A}_{lp_k} = -\omega_{cf}\mathbf{I}_2, \ \ \mathbf{B}_{lp_k} = \omega_{cf}\mathbf{I}_2, \ \ \mathbf{C}_{lp_k} = \mathbf{I}_2, \tag{3.4}$$

where $\mathbf{I}_2$ is the identity matrix, $\mathbf{u}_{lp_k} = [p_k \ q_k]^T$, and $\mathbf{x}_{lp_k} = \mathbf{y}_{lp_k} = [P_k \ Q_k]^T$. In addition, p_k, q_k, P_k, and Q_k refer to the instantaneous and filtered active and reactive powers.

3.3.4 Frequency Controller

Ultimately, a proportional-integral (PI) controller is utilized in the frequency restoration loop as follows:

$$u_{\omega_k} = b_k^{\mathrm{prop}}e_{\omega_k} + b_k^{\mathrm{int}}\int e_{\omega_k}dt, \tag{3.5}$$

where u_{ω_k}, e_{ω_k}, b_k^{prop}, and b_k^{int} refer to the controller output, frequency error, proportional gain, and integral gain.

3.4 Proposed Method

The main idea of the proposed method is to maintain the output power of the inverters within a desired range, corresponding to a high efficiency, by reducing the output power of the unnecessary inverters to zero. In addition to efficiency improvement, the inverter lifetimes can be extended by the proposed method as explained in the following.

3.4.1 Efficiency Improvement

The efficiency curve of the ABB 2-kW solar inverter [79] is considered as the typical efficiency curve of the inverters. To derive a mathematical model for the efficiency curve, the quadratic power loss model [80] is used as follows:

$$P_k^{\mathrm{loss}} = a_0 + a_1 P_k + a_2 P_k^2, \tag{3.6}$$
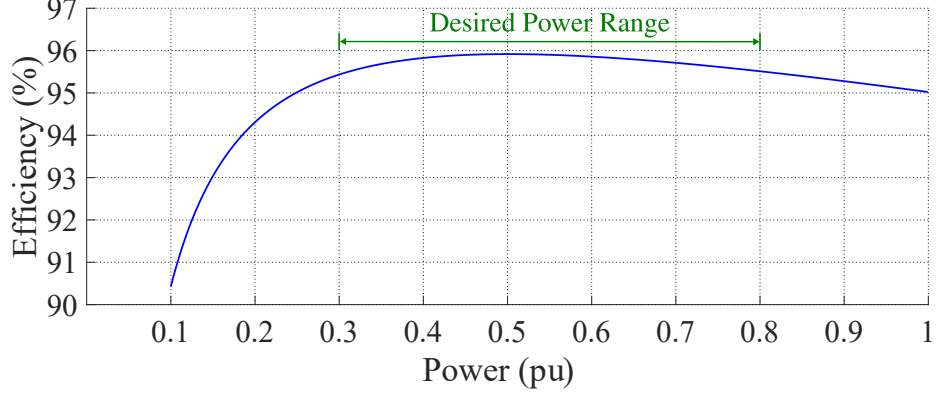
Figure 3.5: Typical efficiency curve of an inverter.

where a_0, a_1, and a_2 are constant parameters that can be obtained via efficiency curve fitting, as depicted in Fig. 3.5 for active powers from 0.1 pu to 1 pu, where 1 pu corresponds to the full-load power, P_k^{fl}. According to the curve, the efficiency is lower in both light and full loads and peaks when the output power is around $0.5P_k^{fl}$. In addition, a high efficiency of more than 95.5% is obtained for active powers between $0.3P_k^{fl}$ and $0.8P_k^{fl}$. Thus, if the output power of each inverter is maintained within $0.3P_k^{fl}$ and $0.8P_k^{fl}$, i.e. the desired power range, the inverter efficiency will be higher than 95.5%. Since the overall system efficiency is given by:

$$\eta = \frac{\sum_{k=1}^{3} P_k}{\sum_{k=1}^{3} (P_k + P_k^{\text{loss}})}, \tag{3.7}$$

by improving the efficiency of every inverter, the overall efficiency of the system will be improved.

3.4.2 Inverter Lifetime Extension

It is shown in the literature that there is a correlation between the lifetime consumption of the inverters and how long they contribute to power sharing [81–83]. Therefore, the capability of the proposed method in extending the lifetimes of the inverters

should be investigated. According to the proposed method, to improve the system efficiency, the inverters with smaller power ratings supply the light loads and the inverters with higher power ratings will be added to the system to supply heavy loads. In light-load cases, the inverters with smaller power ratings can be reprogrammed on a regular basis, e.g. every month, such that different inverters are turned on at lighter loads every month and their lifetimes are extended. Furthermore, the inverters with higher power ratings are more expensive and are considered as valuable assets of the system. Such inverters are only added to the system at heavier loads while operating at a high efficiency with a low loss. Hence, their lifetime is automatically extended by operating in an optimum range instead of sharing power at all times.

3.4.3 Implementation of the Proposed Method

Fig. 3.6 presents the details of the proposed controller of the kth inverter, where the no-load frequency ω_k^{nl} of the droop controller is determined through a multiplexer (Mux). If the inverter power is within the desired range, the output of the Mux is equal to the output of the frequency controller u_{ω_k}, and the frequency is restored at 60 Hz; otherwise, ω_k^{nl} is set to $\omega_{\mathrm{nom}} = 2\pi 60$ rad/s. In other words:

$$
\omega_k^{nl} =
\begin{cases}
\omega_{\mathrm{nom}} & Sel_k = 1 \\[2mm]
u_{\omega_k} & Sel_k = 2
\end{cases}
\tag{3.8}
$$

where Sel_k is the selector signal of the Mux, which is determined as follows:

$$
Sel_k = Hys_{k,1} + Hys_{k,2},
\tag{3.9}
$$

where $Hys_{k,1}$ and $Hys_{k,2}$ are the output of Hysteresis-k_1 and Hysteresis-k_2, respectively. Hysteresis-k_1 determines whether the power of the kth inverter is below or above $0.3P_k^{fl}$. Hence, the hysteresis bands $(h_{k,1}^{\mathrm{min}}, h_{k,1}^{\mathrm{max}})$ should be around the afore-
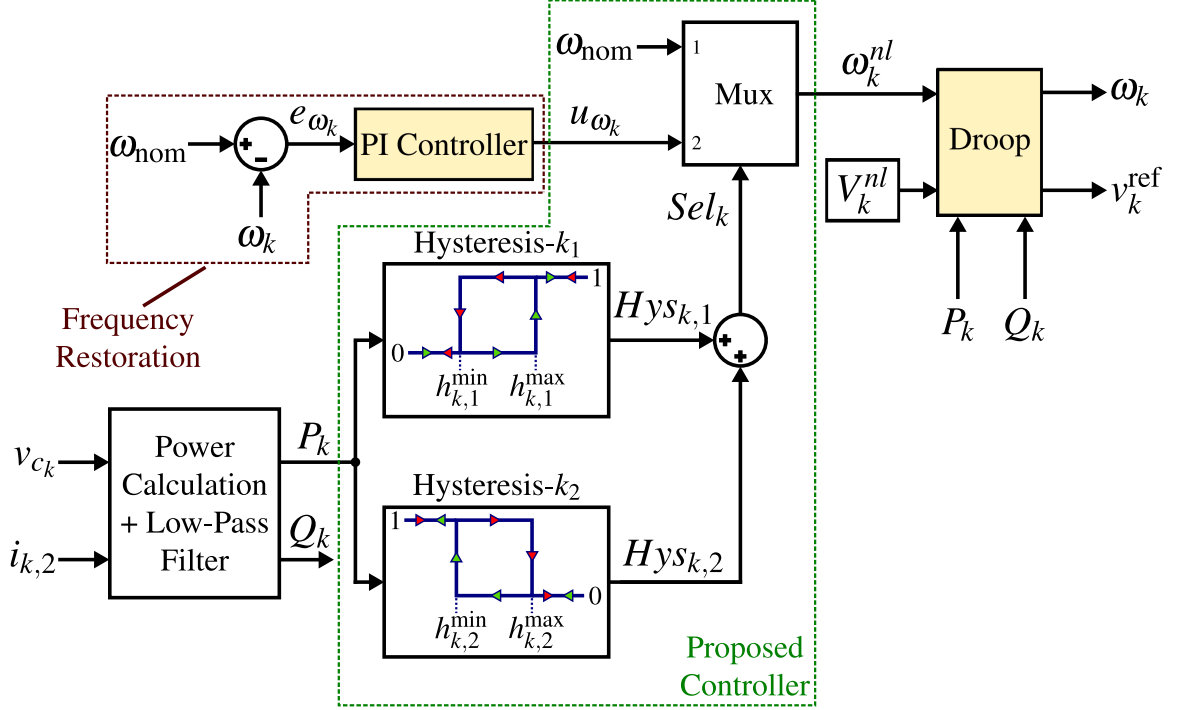
Figure 3.6: Proposed controller of the kth inverter.

mentioned point. Variations of $Hys_{k,1}$ with respect to the inverter power levels are demonstrated in Table 3.1, which is compatible with the directions of Hysteresis-k_1 shown in Fig. 3.6. Additionally, Hysteresis-k_2 determines whether the power of the kth inverter is below or above $0.8P_k^{fl}$. Thus, the hysteresis bands $(h_{k,2}^{\min}, h_{k,2}^{\max})$ should be around the aforementioned point. Variations of $Hys_{k,2}$ with respect to the inverter power levels are represented in Table 3.2, which matches the directions of Hysteresis-k_2 shown in Fig. 3.6. It is worth noting that Hysteresis-k_1 and Hysteresis-k_2 have opposite directions to ensure that when the inverter is operating within the desired power range, Sel_k is set to two.

Considering $P_3^{fl} = P_2^{fl} = 2P_1^{fl} = 2kW$, and taking the possible load levels into account, the system operates in 3 different modes.

Table 3.1: Variations of $Hys_{k,1}$ with respect to the inverter power levels.

P_k	Previous State of $Hys_{k,1}$	$Hys_{k,1}$
$P_k < h_{k,1}^{\min}$	0,1	0
$h_{k,1}^{\min} \leq P_k \leq h_{k,1}^{\max}$	0	0
$h_{k,1}^{\min} \leq P_k \leq h_{k,1}^{\max}$	1	1
$h_{k,1}^{\max} < P_k$	0,1	1

Table 3.2: Variations of $Hys_{k,2}$ with respect to the inverter power levels.

P_k	Previous State of $Hys_{k,2}$	$Hys_{k,2}$
$P_k < h_{k,2}^{\min}$	0,1	1
$h_{k,2}^{\min} \leq P_k \leq h_{k,2}^{\max}$	0	0
$h_{k,2}^{\min} \leq P_k \leq h_{k,2}^{\max}$	1	1
$h_{k,2}^{\max} < P_k$	0,1	0

3.4.3.1 Mode 1: Normal Condition

At least one of the inverters operates within the desired power range and restores the system frequency at 60 Hz. In this mode, the injected power by the inverters operating out of the desired power range would be zero since their no-load frequencies ω_k^{nl} are equal to the system frequency at ω_{nom}. Fig. 3.7(a) depicts the droop curves of inverters operating in *Mode 1* when a light load is connected to the system. Since P_{L_1} only lies within the desired power range of Inverter 1, this inverter solely supplies the load. In Fig. 3.7(b), the load increases to an amount more than $0.8P_1^{fl}$. Thus, Inverter 2 starts to supply the load. It is worth noting that in case that two or more inverters have the same rated power, the inverter with the smallest assigned number "k" supplies the load before the others. Finally, as shown in Fig. 3.7(c), when the load increases to an amount more than $0.8P_1^{fl} + 0.8P_2^{fl}$, all three inverters supply the load, while operating within the desired power range.

(a) $0.3P_1^{fl} \leqslant P_{L_1} \leqslant 0.8P_1^{fl} \Rightarrow Sel_1 = 2, Sel_2 = Sel_3 = 1 \Rightarrow P_{L_1} = P_1$: *Mode 1.*

(b) Load increases to $P_{L_2} > 0.8P_1^{fl} \Rightarrow Sel_1 = Sel_2 = 2, Sel_3 = 1 \Rightarrow P_{L_2} = P_1 + P_2$: *Mode 1.*

(c) Load increases to $P_{L_3} > 0.8P_1^{fl} + 0.8P_2^{fl} \Rightarrow Sel_1 = Sel_2 = Sel_3 = 2 \Rightarrow P_{L_3} = P_1 + P_2 + P_3$: *Mode 1.*

(d) Load increases to very-heavy load $\sum_{k=1}^{3} 0.8P_k^{fl} < P_{L_4} \leqslant \sum_{k=1}^{3} P_k^{fl} \Rightarrow Sel_1 = Sel_2 = Sel_3 = 1 \Rightarrow P_{L_4} = P_1 + P_2 + P_3$: *Mode 2.*
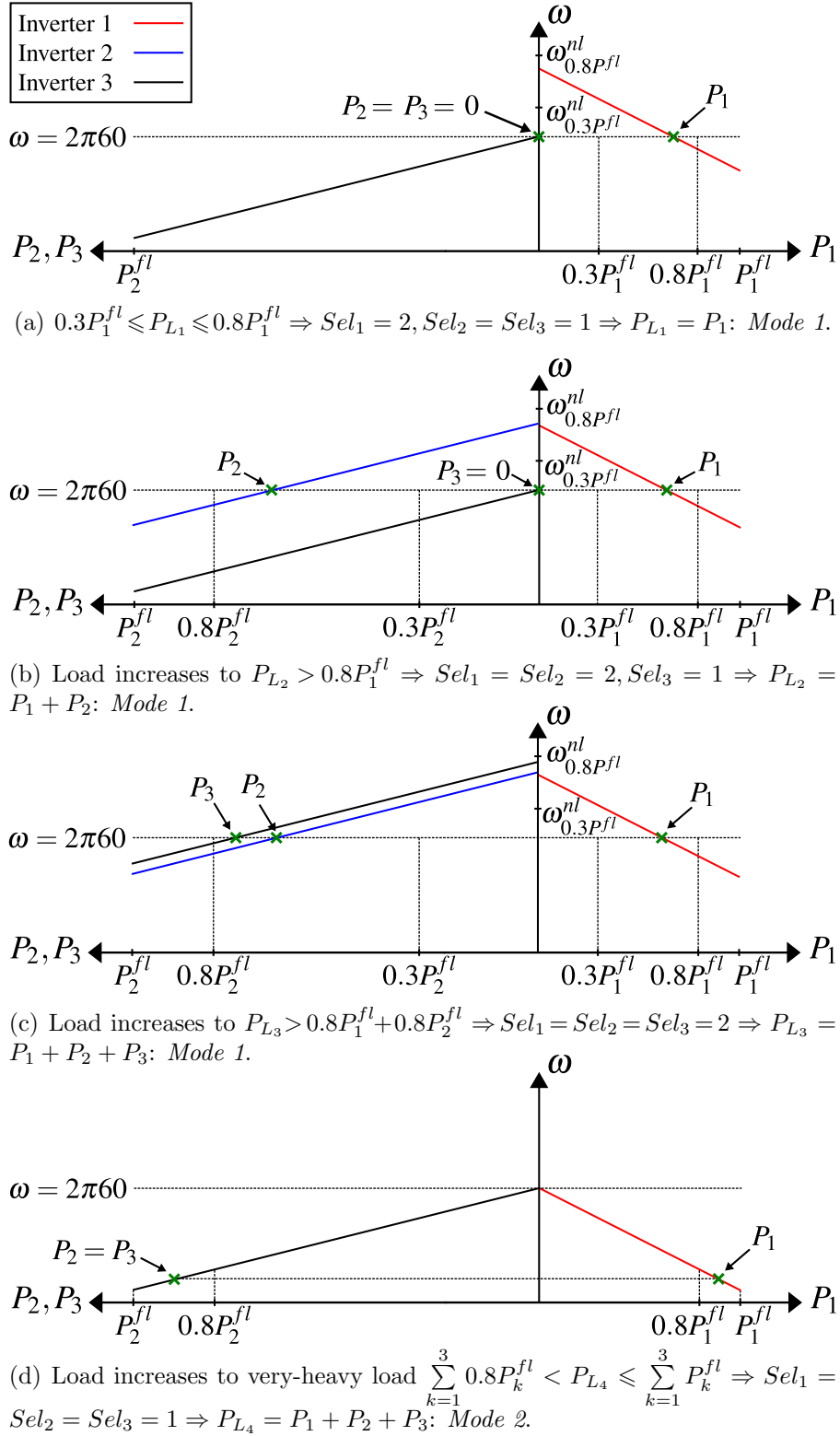
Figure 3.7: Droop characteristics of the inverters operating in *Mode 1* and *Mode 2* at different load profiles.

3.4.3.2 Mode 2: Very-Heavy Load

In this mode, all inverters operate above the desired power range, i.e. $0.8 P_k^{fl} < P_k \leqslant P_k^{fl}$, $k = 1, 2, 3$. Therefore, the no-load frequency of each inverter ω_k^{nl} is set to ω_{nom} to operate similar to the conventional droop, and the loads demand is shared among the inverters proportional to their power ratings. Fig. 3.7(d) illustrates the droop characteristics of the inverters when a very-heavy load is connected to the system, with a power such that $\sum_{k=1}^{3} 0.8 P_k^{fl} < P_L \leqslant \sum_{k=1}^{3} P_k^{fl}$.

3.4.3.3 Mode 3: Very-Light Load

This mode happens if all inverters operate below the desired power range, i.e. $P_k < 0.3 P_k^{fl}$, $k = 1, 2, 3$. In this case, all online inverters should be detected, so that the inverter with the lowest rated power restores the frequency at 60 Hz and supplies the loads, while the other inverters share no power. The operation details of this mode are discussed in Chapter 4.

3.5   Design of System Parameters

A step-by-step design procedure is described in this section to find the optimal values of the system parameters. First, the droop coefficients are determined such that the frequency and voltage drops caused by the droop strategy lie within an acceptable range. Afterwards, the LPF cut-off frequency ω_{cf} is tuned to filter the high-frequency components in the instantaneous power signals and provide virtual inertia for the inverters. Once ω_{cf} is tuned, the virtual impedances and the frequency controllers can be designed, respectively. Finally, the hysteresis bands are designed so that the proposed controller can check whether the active power lies within the desired power range or not.

3.5.1 Droop Coefficients

As the deviations of voltage amplitude and frequency at different load levels are dependent on the droop coefficients, m_k and n_k should be designed properly to maintain the deviations within an acceptable range. Considering the system operating modes, the maximum frequency is $f_{\text{nom}} = 60$ Hz. Moreover, when the system is operating in *Mode 2*, the frequency drops to its minimum value at full load, as shown in Fig. 3.8(a), where the no-load frequency and power injection of Inverter k are $\omega_k^{nl} = 2\pi 60$ $^{\text{rad}}/_{\text{s}}$ and $P_k = P_k^{fl}$, respectively. Assuming the minimum allowable frequency, ω_k^{fl}, to be 1% below $2\pi 60$ $^{\text{rad}}/_{\text{s}}$, the frequency-droop coefficient is obtained from (3.1) as follows:

$$m_k = \frac{\omega_k^{nl} - \omega_k^{fl}}{P_k^{fl}}. \tag{3.10}$$

Similarly, the voltage-droop coefficient can be derived by assuming a maximum of 3% voltage deviation around the nominal value, as shown in Fig. 3.8(b), where $V_k^{nl} = 120\sqrt{2}$ V, and $Q_k = Q_k^{fl}$. Therefore, according to (3.1), the voltage-droop coefficient is given by:

$$n_k = \frac{V_k^{nl} - V_k^{fl}}{Q_k^{fl}}. \tag{3.11}$$

To sum up, the designed values of droop coefficients are:

(a)   (b)
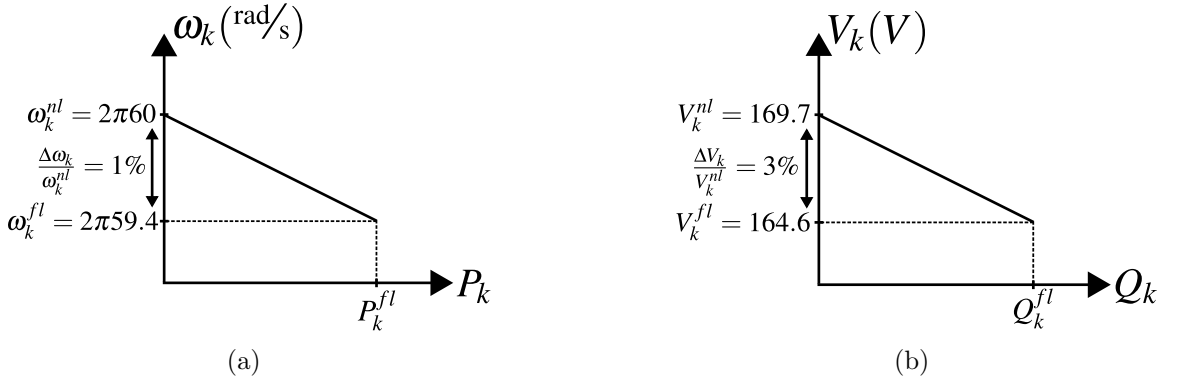
Figure 3.8: Designing the voltage and frequency-droop coefficients: (a) $P - \omega$ droop curve with the maximum frequency deviation, and (b) $Q - V$ droop curve with the maximum voltage deviation.

$$m_1 = 0.0038 \text{ rad/w.s}, m_2 = m_3 = 0.0019 \text{ rad/w.s}, \tag{3.12}$$

$$n_1 = 0.0051 \text{ V/VAr}, n_2 = n_3 = 0.0025 \text{ V/VAr}. \tag{3.13}$$

3.5.2 LPF Cut-Off Frequency

LPFs are used to filter out the high-frequency components in the active and reactive power measurements. Additionally, the LPFs help to improve the stability of the system and provide virtual inertia similar to virtual synchronous machines (VSM) [75–77].

A VSM emulates the inertial characteristic and oscillation damping feature of a synchronous machine (SM) [84]. For this purpose, the equation of the VSM must be derived from the swing equation of the SM. Therefore, the swing equation of the VSM in the Laplace domain is given by:

$$T_a.s.\omega_{\text{VSM}} = P_{\text{in}} - P_{\text{out}} - k_d(\omega_{\text{VSM}} - \omega_g), \tag{3.14}$$

where ω_{VSM}, P_{in}, P_{out}, k_d, and ω_g refer to the virtual rotating speed of the VSM, the emulated mechanical input power, the emulated mechanical output power, the damping coefficient, and the grid frequency, respectively. Furthermore, T_a and H are the mechanical time constant and the inertia constant of a SM, respectively, and they are related to each other as $T_a = 2H$. According to (3.14), Fig. 3.9(a) depicts the

(a)   (b)
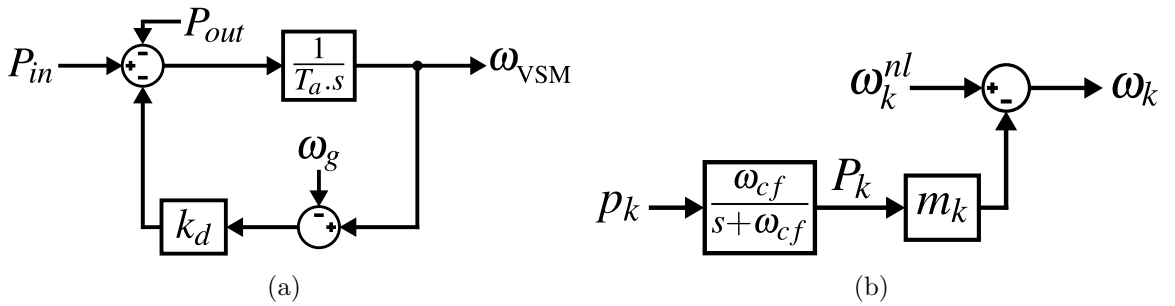
Figure 3.9: Block diagram of (a) a typical VSM, and (b) a frequency droop controller with an LPF.

block diagram of a typical VSM.

On the other hand, Fig. 3.9(b) illustrates the block diagram of a frequency droop controller with a low-pass filter. The corresponding droop equation can be written as follows:

$$\frac{1}{m_k \omega_{cf}}.s.\omega_k = -p_k - \frac{1}{m_k}\left(\omega_k - \omega_k^{nl}\right),$$ (3.15)

where p_k is the instantaneous power. Comparing (3.14) and (3.15) results in $T_a = \frac{1}{m_k \omega_{cf}}$ and $k_d = \frac{1}{m_k}$. In this thesis, it is assumed that all inverters have the same ω_{cf}, and T_a of Inverter 2 and Inverter 3 is selected twice the T_a of Inverter 1 so that more inertia is provided by the inverters with higher rated powers. Considering Inverter 1, if $H = 1s$, then $T_a = 2s$ and $\omega_{cf} = 131.58$ rad/s.

3.5.3 Virtual Impedances

The virtual impedance is used to improve the stability of the system and make the output impedance of the inverters more inductive to make sure the droop equations are valid [23]. The design objective of tuning the virtual impedances is to minimize the active power oscillations caused by load variations. To tune the virtual impedances and perform per unit calculations, the nominal voltage and power of Inverter 1 are considered as the base values, i.e. $V_b = 120\sqrt{2}\ V$ and $P_b = 1\ kW$. Since the inverters with higher rated powers have higher voltage drops at their output, the virtual impedances are assumed to be related to the rated powers as follows:

$$L_1^{\mathrm{vir}} P_1^{fl} = L_2^{\mathrm{vir}} P_2^{fl} = L_3^{\mathrm{vir}} P_3^{fl}.$$ (3.16)

The design procedure includes two steps. In the first step, the effect of the virtual impedance variations on the system dominant poles is observed, and a proper parameter range, in which the system is stable, is selected. In the next step, the system is simulated with different values of the virtual impedance to monitor its im-

pact on the active power oscillations. Considering the mode changes introduced in Section 3.4, the loads and no-load frequencies should change simultaneously to realize the worst-case scenario that can cause oscillations in the active power. Thus, while the proposed controller shown in Fig. 3.6 is disconnected, a load is connected at $t = 0s$ and an arbitrary step signal is applied to the no-load frequencies at the same time. The power error is defined as $e_{P_k} \triangleq P_{k_{ss}} - P_k$, where $P_{k_{ss}}$ is the steady-state value of the active power, and P_k is the average active power at any point of time. Then, the integral of absolute error (IAE) performance index for the kth inverter, IAE_k, and the entire system, IAE_{total}, are obtained as follows:

$$IAE_k = \int_0^\infty |e_{P_k}(t)|dt, \ \ IAE_{\text{total}} = \sum_{k=1}^{3} IAE_k. \tag{3.17}$$

The virtual impedance at which IAE_{total} is minimized is selected as the optimum value.

According to (3.16), if L_1^{vir} is tuned, L_2^{vir} and L_3^{vir} are obtained automatically. Fig. 3.10 illustrates the displacement of the dominant poles of the system with respect to variations in L_1^{vir} from 0 to 3.75×10^{-4} pu. Hence, the proper range for L_1^{vir} is
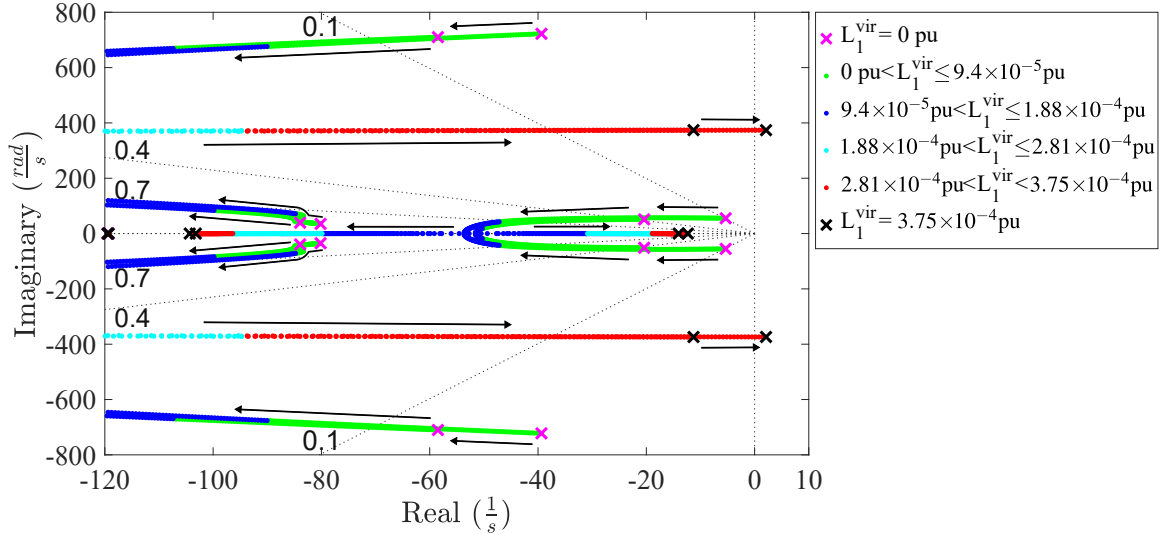
Figure 3.10: Step 1 of designing L_1^{vir}: selecting the proper range according to the root locus of the system dominant poles by variations in L_1^{vir}.
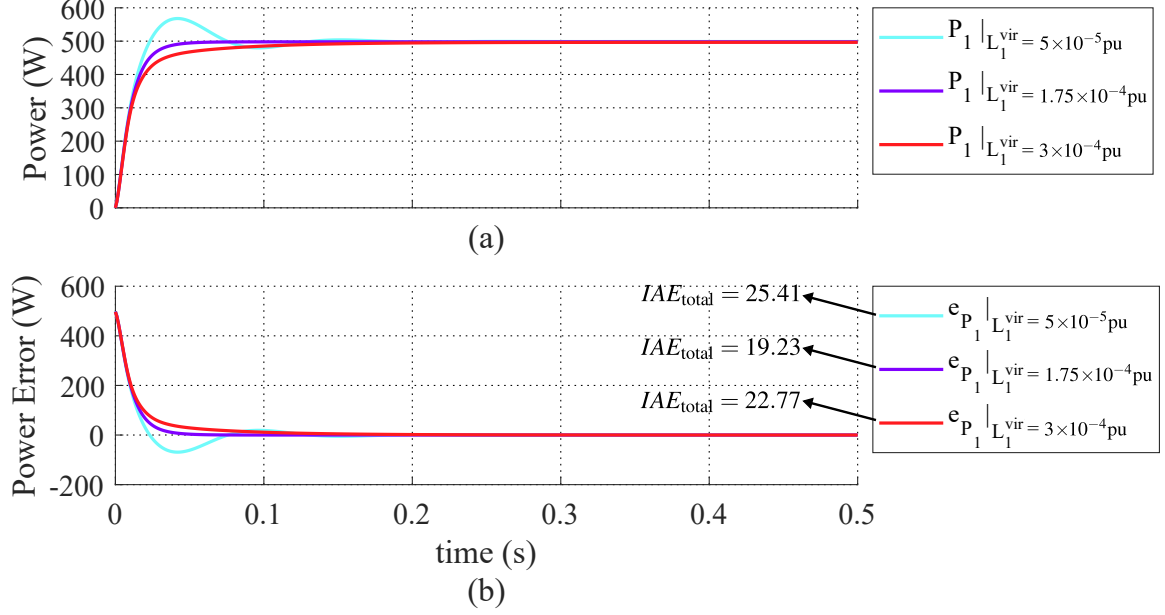
Figure 3.11: Step 2 of designing L_1^{vir}: obtaining the optimum value of L_1^{vir} by minimizing the IAE index; (a) active power characteristics of Inverter 1 in response to a simultaneous step change in the loads and no-load frequencies of the inverters, and (b) power errors of Inverter 1.

selected from 0.5×10^{-4} pu to 3×10^{-4} pu. As the next step, Fig. 3.11(a) depicts the active power responses of Inverter 1 in the worst-case scenario with respect to changes in L_1^{vir}, and the corresponding power errors are presented in Fig. 3.11(b). The optimum value of L_1^{vir} that minimizes IAE_{total} is found to be 1.75×10^{-4} pu, corresponding to the purple lines in Fig. 3.11.

3.5.4 Frequency Controllers

To design the frequency controllers, it is assumed that the system is operating in *Mode 1*, and the controllers should be designed such that the power oscillations are minimized. Since the inverters with lower rated powers are supposed to supply the lighter loads, their frequency restoration process needs to be faster. Thus, the controller parameters are assumed to be related to the rated powers as follows:

$$b_1^{\text{prop}} P_1^{fl} = b_2^{\text{prop}} P_2^{fl} = b_3^{\text{prop}} P_3^{fl}, \tag{3.18}$$

47

$$b_1^{\text{int}} P_1^{fl} = b_2^{\text{int}} P_2^{fl} = b_3^{\text{int}} P_3^{fl}. \tag{3.19}$$

The design procedure of the frequency controllers is the same as the virtual impedances with the exception that in the second step, the step change is only applied in the load since the no-load frequencies are controlled by the frequency controllers.

Fig. 3.12 shows the displacement of the dominant poles of the system with respect to variations in b_1^{prop} from 0 to 5. The proper range for b_1^{prop} is selected from 0 to 1.25 since this range corresponds to a faster and more stable system according to the pole locations. As the second step, Fig. 3.13(a) depicts the active power responses of Inverter 1 with respect to changes in b_1^{prop}, and the corresponding power errors are presented in Fig. 3.13(b). It is worth remarking that since the frequency controllers are changing the droop no-load frequencies, the steady-state powers of the inverters will be different for different values of b_1^{prop}. The optimum value of b_1^{prop} that minimizes IAE_{total} is found to be 0.8, whose response is shown by the purple lines in Fig. 3.13.

The optimum value of b_1^{int} can be found by the same procedure. Fig. 3.14 shows the displacement of the dominant poles of the system with respect to variations in
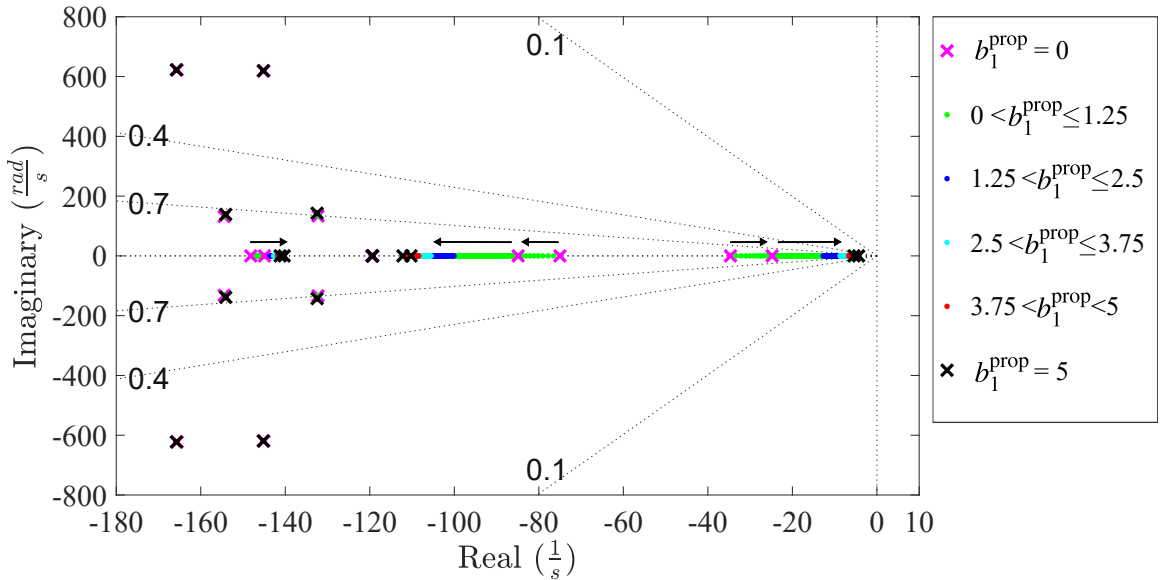
Figure 3.12: Step 1 of designing b_1^{prop}: selecting the proper range according to the root locus of the system dominant poles by variations in b_1^{prop}.
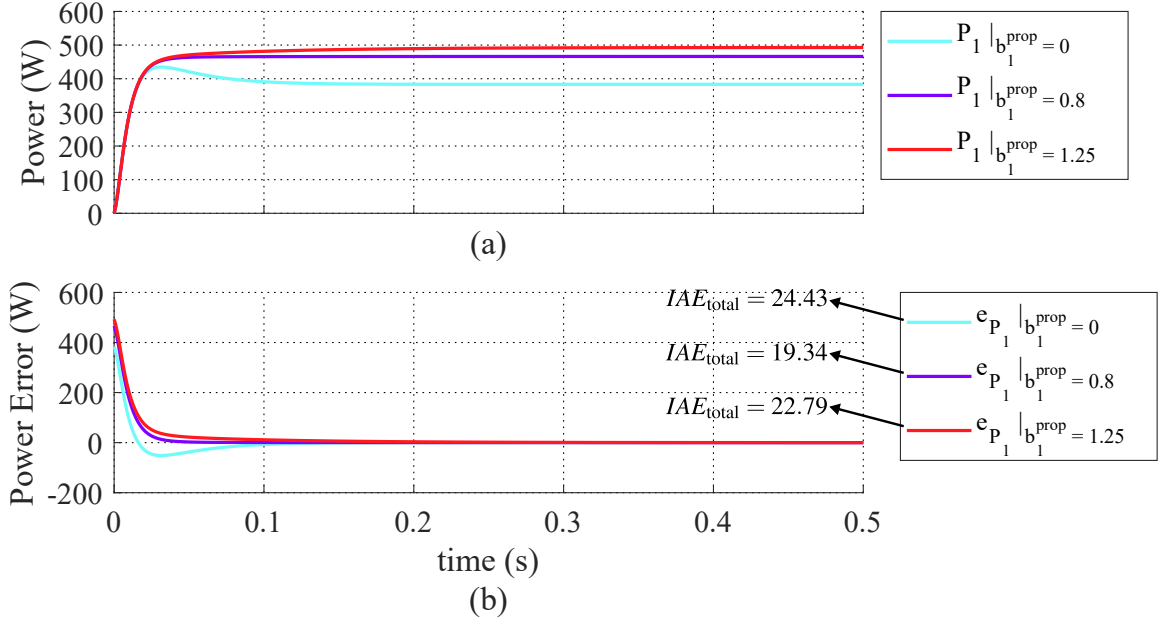
Figure 3.13: Step 2 of designing b_1^{prop}: obtaining the optimum value of b_1^{prop} by minimizing the IAE index; (a) active power characteristics of Inverter 1 in response to a step change in the load, and (b) power errors of Inverter 1.

b_1^{int} from 0 to 400. The proper range for b_1^{int} is selected from 100 to 300. As the second step of design, Fig. 3.15(a) depicts the active power responses of Inverter 1 with respect to changes in b_1^{int}, and the corresponding power errors are presented in
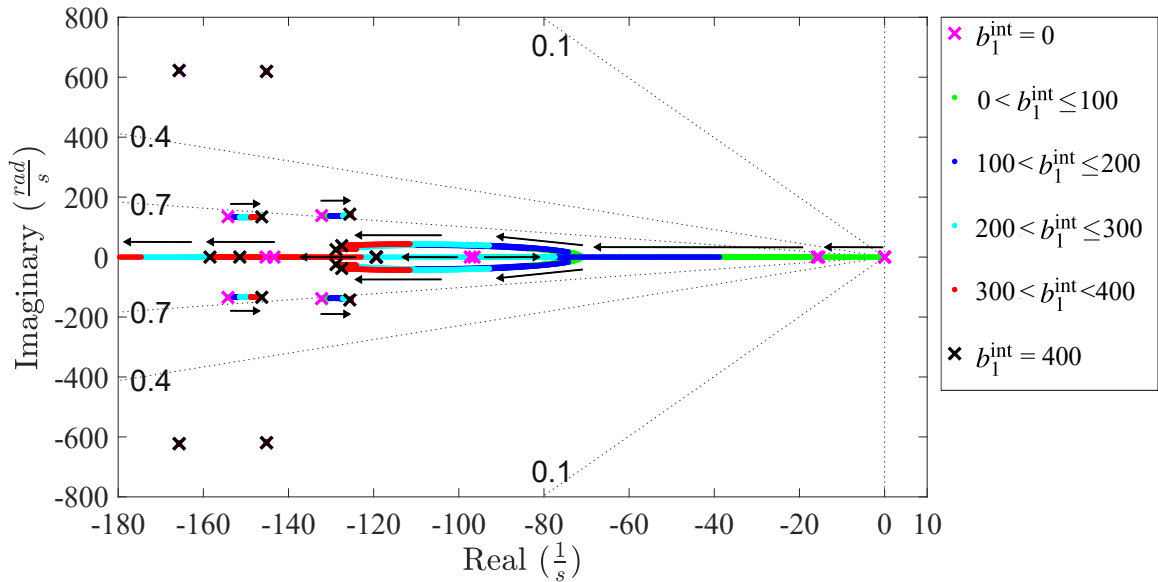
Figure 3.14: Step 1 of designing b_1^{int}: selecting the proper range according to the root locus of the system dominant poles by variations in b_1^{int}.
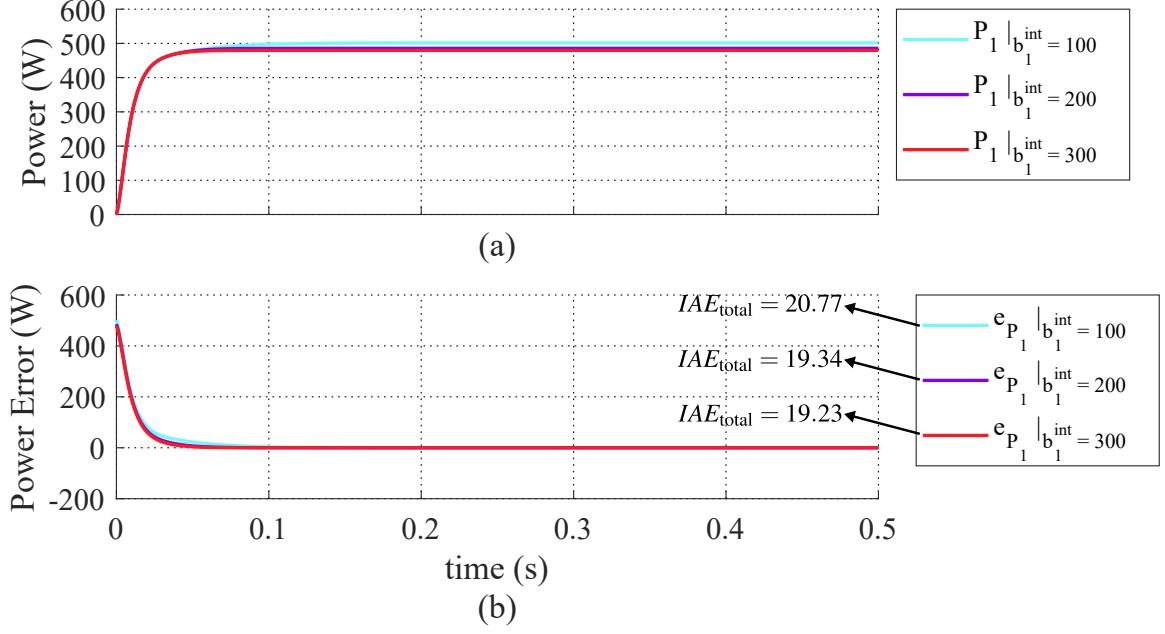
Figure 3.15: Step 2 of designing b_1^{int}: obtaining the optimum value of b_1^{int} by minimizing the IAE index; (a) active power characteristics of Inverter 1 in response to a step change in the load, and (b) power errors of Inverter 1.

Fig. 3.15(b). The optimum value of b_1^{int} that minimizes IAE_{total} is found to be 300, which corresponds to the red lines in Fig. 3.15.

3.5.5 Hysteresis Bands

The hysteresis blocks check whether or not the active powers of inverters lie within the desired power range. Considering (3.9), the hysteresis bands should be selected such that redundant activations and deactivations of the inverters due to changes in the hysteresis outputs are avoided. Thus, supposing a margin of $\pm 10\%$ around $0.3 P_k^{fl}$ and $0.8 P_k^{fl}$, the upper and lower bands of Hysteresis-k_1 and Hysteresis-k_2 are given by:

$$h_{k,1}^{\min} = 0.9(0.3 P_k^{fl}), \ h_{k,1}^{\max} = 1.1(0.3 P_k^{fl}), \tag{3.20}$$

$$h_{k,2}^{\min} = 0.9(0.8 P_k^{fl}), \ h_{k,2}^{\max} = 1.1(0.8 P_k^{fl}). \tag{3.21}$$

3.6 Stability Verification

The stability of the parallel GFM inverter system considering variations in the no-load frequencies, $f_k^{nl} = \frac{\omega_k^{nl}}{2\pi}$, is studied in this section. As $\omega_1^{nl,\max} = \omega_{\mathrm{nom}} + m_1 P_1^{fl}$ according to (3.1), the maximum and minimum amounts of the no-load frequency of Inverter 1 are $f_1^{nl,\max} = 60.67$ Hz and $f_1^{nl,\min} = f_{\mathrm{nom}} = 60$ Hz, respectively. Therefore, the operating range of the no-load frequency of Inverter 1 is 60 Hz $\leq f_1^{nl} \leq 60.67$ Hz. To examine the system stability in the operating range, displacement of system dominant poles due to variations in f_1^{nl} from 60 Hz to 63.5 Hz is investigated, as shown in Fig. 3.16. The poles in the operating range, depicted with green stars, are all located in the left-half plane, implying a stable system. Moreover, as the no-load frequency increases, the poles that are closer to the origin start to move to the right. At $f_1^{nl} = 63.295$ Hz, one of the poles crosses the imaginary axis, and the system becomes unstable for no-load frequencies higher than $f_1^{nl} = 63.295$ Hz.

The operating range of the no-load frequencies of Inverter 2 and Inverter 3 can be derived by a similar approach as 60 Hz $\leq f_2^{nl} = f_3^{nl} \leq 60.67$ Hz. Fig. 3.17 depicts the displacement of the dominant poles of the system by varying f_2^{nl} and f_3^{nl} from 60 Hz
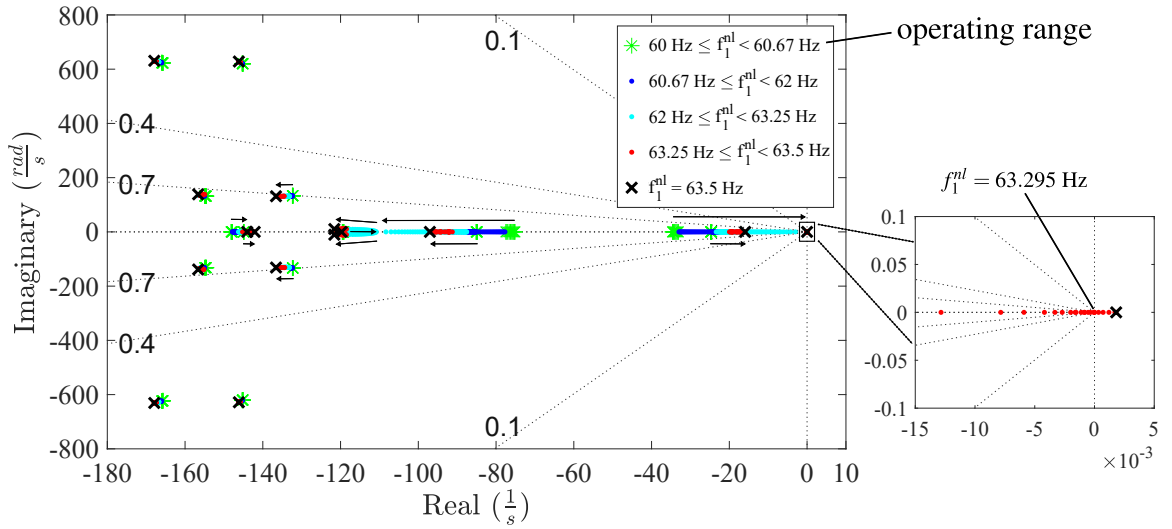
Figure 3.16: Displacement of the dominant poles due to variations in f_1^{nl} from 60 Hz to 63.5 Hz.

51
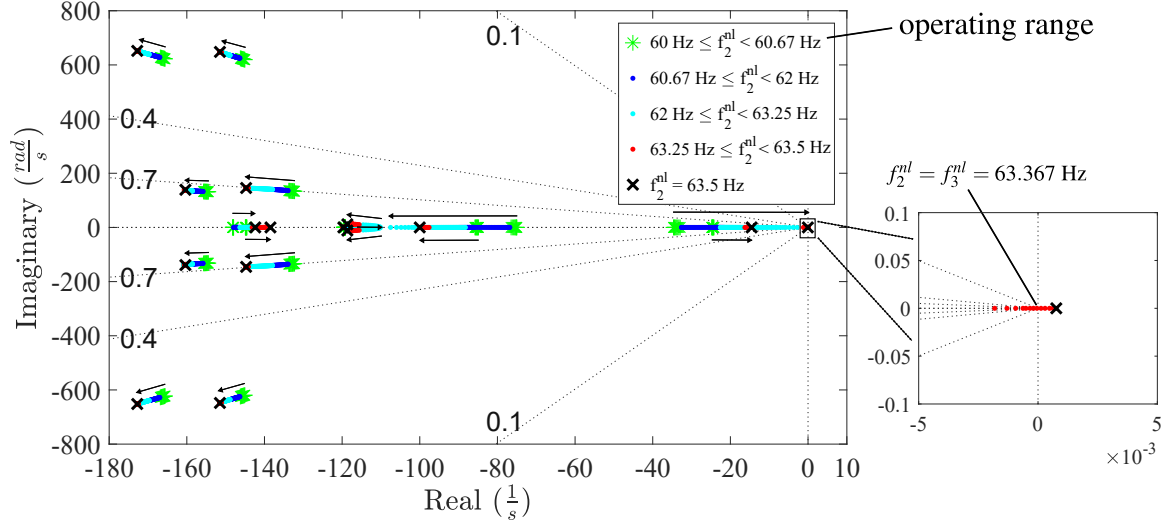
Figure 3.17: Displacement of the dominant poles due to variations in f_2^{nl} and f_3^{nl} from 60 Hz to 63.5 Hz.

to 63.5 Hz. The green stars represent the poles in the operating range, which are located in the left-half plane, implying a stable system. Furthermore, by increasing the no-load frequencies, the poles that are closer to the origin start to move to the right. At $f_2^{nl} = f_3^{nl} = 63.367$ Hz, one of the poles crosses the imaginary axis, and the system becomes unstable for no-load frequencies higher than the mentioned value.

3.7   Experimental Results

In the experimental setup, depicted in Fig. 3.18, two single-phase parallel inverters with power ratings of $P_1^{fl} = 200$ W and $P_2^{fl} = 400$ W are connected to the loads via LCL filters. A switch is used to connect Inverter 2 to the system after synchronization. The dc supplies are implemented with Chroma programmable dc power supply 62012P and Sorensen programmable power supply SGX500X10C. Furthermore, the inverter controllers are implemented on dSPACE MicroLabBox (RTI 1202).

Fig. 3.19 illustrates the experimental results when the inverters are operating in *Mode 1*. Initially, the load is 100 W that lies within the desired power range of Inverter 1. As shown in Fig. 3.19, only Inverter 1 contributes to supply the load,
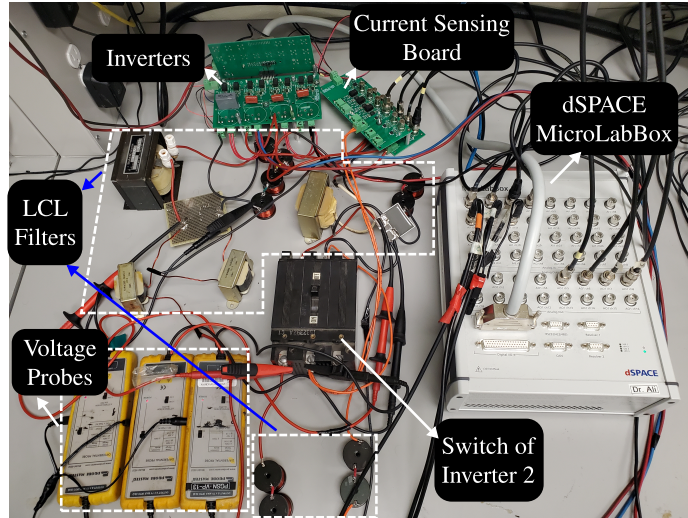
Figure 3.18: Experimental setup.

and the system operates in *Mode 1*. Next, the load changes to 240 W. In this case, Inverter 2 cooperates with Inverter 1 in feeding the load. Finally, the load returns to 100 W. Consequently, the proposed controller of Inverter 2 reduces its power injection, and Inverter 1 keeps supplying the load merely.
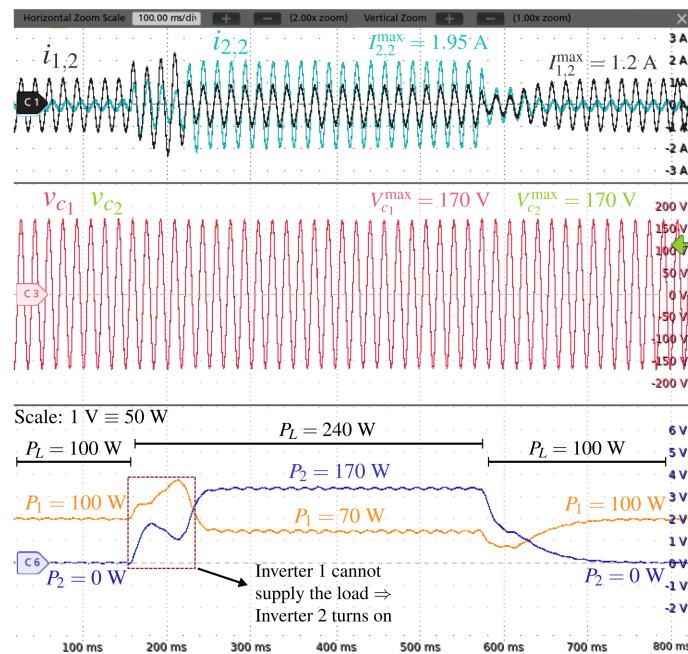
Figure 3.19: Experimental results: performance of the proposed controller in improving the efficiency by deactivating the unnecessary inverter in *Mode 1*.

53

3.8   Summary

A communicationless modified droop strategy is proposed in this chapter to improve the overall system efficiency of parallel GFM inverters. A system with three parallel single-phase inverters is studied to evaluate the performance of the proposed controller in enhancing the system efficiency. Once the state-space models of the control system components are derived, the proposed method is explained based on the efficiency curve of a single inverter. The main idea is to maintain the output power of the inverters within a desired range that corresponds to a high efficiency by reducing the power of the unnecessary inverters to zero. Subsequently, the proposed controller to obtain the aforementioned objective is described, and different system operating modes are explained. Next, the system parameters are designed, and the stability of the system within the designed operating range of the no-load frequencies is studied. Finally, experimental results are provided to verify the proposed method. More simulation and experimental results will be provided in Chapter 4, where the proposed controller accounts for the very-light load situations and improves the system efficiency in such cases, as well.

Chapter 4

Online-Inverter Detection and Efficiency Improvement

4.1 Introduction

In Chapter 3, a decentralized modified droop strategy was proposed to improve the overall system efficiency of parallel GFM inverters. Under the proposed method, the system had three operating modes. The third mode which included very-light load situations is discussed in this chapter.

This chapter presents a decentralized online-inverter detection (OID) method based on a transient coded frequency deviation such that each inverter detects the other online inverters in very-light load situations, and a minimum number of inverters with the lowest rated powers supply the loads to improve the overall efficiency. As a result, all the selected inverters will operate at higher power levels and thus, at a higher efficiency compared with the case where all of the inverters shared the power and operated at low power levels. To study the effectiveness of the method, the OID is integrated with the proposed control system in Chapter 3, and applied to the inverter system described in Chapter 3. It is shown that the OID retains the

advantages of parallel inverters such as modularity, flexibility, and reliability. There-fore, to add new inverters to the system, there is no need to reprogram the existing inverters. Detailed simulation and experimental results are provided to evaluate the performance of the developed control system containing the OID in improving the system efficiency.

4.2   Online-Inverter Detection (OID) Method

A decentralized online-inverter detection (OID) method is proposed in this section to detect the online inverters in a parallel GFM inverter system at very-light loads, where all of the inverters operate below the desired power range derived in Chapter 3. There is no direct method to detect the online inverters in the system without using communication links. Therefore, an indirect method is proposed, which is based on a transient coded frequency deviation.

Frequency is a common variable among all inverters. Hence, when a step signal is applied to the inverter no-load frequencies, its steady-state impact on the frequency can be observed by all inverters. According to the frequency-droop equation (3.1), the amount of the frequency deviation in the steady-state condition is given by:

$$
\begin{aligned}
\Delta\omega_1 &= \Delta\omega_1^{nl} - m_1\Delta P_1 = \Delta\omega, \\
\Delta\omega_2 &= \Delta\omega_2^{nl} - m_2\Delta P_2 = \Delta\omega, \\
\Delta\omega_3 &= \Delta\omega_3^{nl} - m_3\Delta P_3 = \Delta\omega.
\end{aligned}
\tag{4.1}
$$

Furthermore, assuming the loads have not changed during the step application, it is concluded that $\Delta P_1 + \Delta P_2 + \Delta P_3 = 0$. Solving the system of four equations, the frequency deviation is obtained by:

$$\Delta\omega = \frac{\frac{\Delta\omega_1^{nl}}{m_1} + \frac{\Delta\omega_2^{nl}}{m_2} + \frac{\Delta\omega_3^{nl}}{m_3}}{\frac{1}{m_1} + \frac{1}{m_2} + \frac{1}{m_3}}. \tag{4.2}$$

Moreover, since m_k is inversely proportional to the full-load power of the inverter, P_k^{fl}, (4.2) can be rewritten as:

$$\Delta\omega = \frac{P_1^{fl}\Delta\omega_1^{nl} + P_2^{fl}\Delta\omega_2^{nl} + P_3^{fl}\Delta\omega_3^{nl}}{P_1^{fl} + P_2^{fl} + P_3^{fl}}. \tag{4.3}$$

The main idea behind the proposed OID is that each inverter generates two coded pulses and applies the pulses to its no-load frequency in case a very-light load situation is detected. Thus, two transient deviations are observed in the system frequency, and the measured frequency deviation ratio $\frac{\Delta\omega'}{\Delta\omega}$ by the inverters yields a unique number that corresponds to a specific set of online inverters in a lookup table. Consequently, the online-inverter vector is obtained.

Fig. 4.1 indicates how the developed method detects the online inverters. It should be noted that the proposed controller of each inverter contains the OID, and the process does not need any communication among the inverters. Overall, the OID consists of four consecutive steps. In Step 1, the control system of each inverter detects the very-light load situation by checking two conditions, i.e. saturation of the frequency controller, and the active power being less than $0.3P_k^{fl}$ ($Hys_{k,1} = 0$). If the mentioned conditions are met, two pulses with a time-delay difference, $VLP_{k,1}$ and $VLP_{k,2}$, are generated. It is worth mentioning that in practice, the pulses of different inverters might not be applied simultaneously. Therefore, the pulse widths and the time delay between the pulses should be selected sufficiently wide so that the controllers of all inverters can measure the frequency at the final steady-state conditions, where all the inverters have applied their pulses.

In Step 2, the amplitudes of both pulses are coded. According to (4.3), the
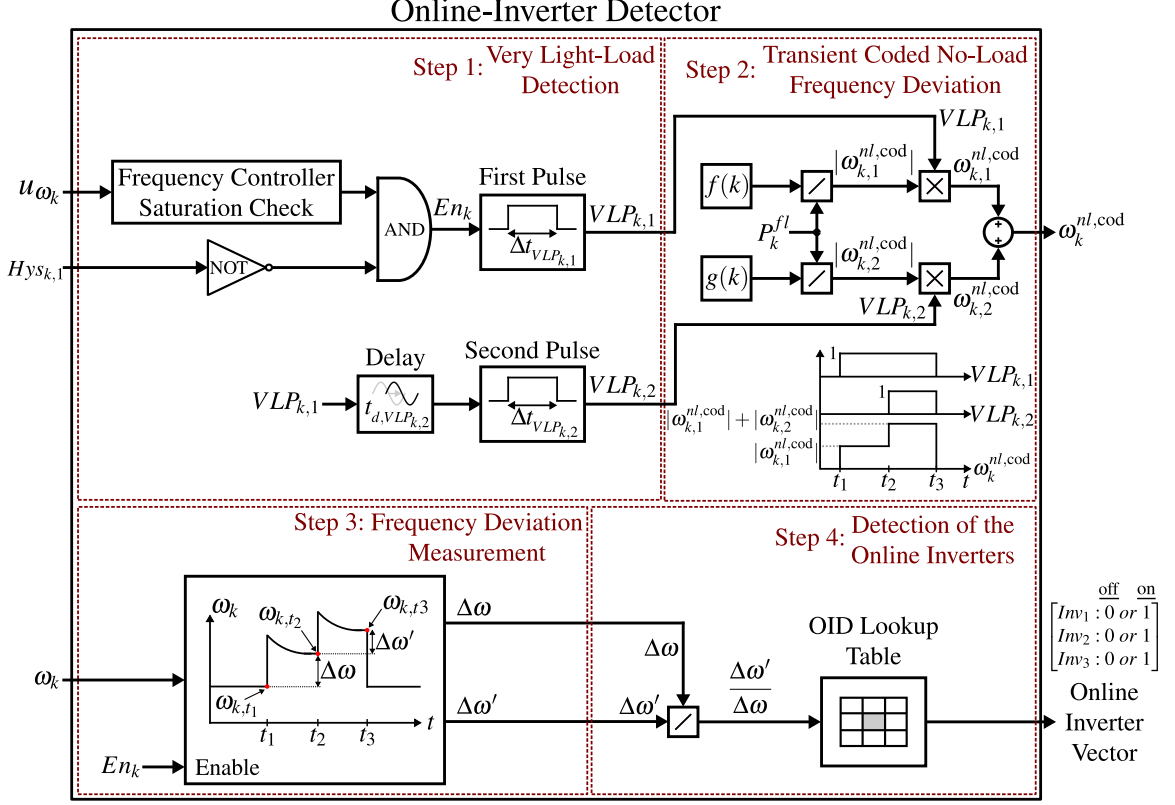
Figure 4.1: Online-Inverter detector of the kth inverter.

frequency deviation caused by the coded pulses can be calculated as:

$$\Delta\omega = \frac{\sum\limits_{k=1}^{3} P_k^{fl}|\omega_{k,1}^{nl,\text{cod}}|}{\sum\limits_{k=1}^{3} P_k^{fl}} \ , \ \Delta\omega' = \frac{\sum\limits_{k=1}^{3} P_k^{fl}|\omega_{k,2}^{nl,\text{cod}}|}{\sum\limits_{k=1}^{3} P_k^{fl}}. \tag{4.4}$$

Hence, the frequency deviation ratio is given by:

$$\frac{\Delta\omega'}{\Delta\omega} = \frac{\sum\limits_{k=1}^{3} P_k^{fl}|\omega_{k,2}^{nl,\text{cod}}|}{\sum\limits_{k=1}^{3} P_k^{fl}|\omega_{k,1}^{nl,\text{cod}}|}. \tag{4.5}$$

To eliminate the effect of P_k^{fl} in (4.5), the amplitudes of the pulses are chosen as:

$$|\omega_{k,1}^{nl,\text{cod}}| = \frac{f(k)}{P_k^{fl}}, \ |\omega_{k,2}^{nl,\text{cod}}| = \frac{g(k)}{P_k^{fl}}. \tag{4.6}$$

In (4.6), $f(k)$ and $g(k)$ are functions of the inverter assigned number, k, to code the amplitude of the pulses. Substituting (4.6) in (4.5) yields:

$$\frac{\Delta\omega'}{\Delta\omega} = \frac{\sum\limits_{k=1}^{3} g(k)}{\sum\limits_{k=1}^{3} f(k)}. \tag{4.7}$$

As the frequency deviation ratio is given by (4.7), $f(k)$ and $g(k)$ should be monotonically increasing or decreasing to produce disperse values for different inverter numbers, k, so that a unique frequency deviation ratio is obtained for each set of online inverters. Thus, it is assumed that $f(k)$ and $g(k)$ are natural logarithm functions, where $f(k)$ is monotonically decreasing, and $g(k)$ is monotonically increasing. The maximum values of the pulse amplitudes should be chosen carefully to avoid a large change in the system frequency. Additionally, the minimum values of the pulse amplitudes should be chosen sufficiently large such that the frequency change can be measured by the inverters. Therefore, the minimum and maximum values of pulse amplitudes are assumed to be 0.005 rad/s and 1 rad/s, respectively. Hence, according to (4.6), the minimum and maximum values of $f(k)$ and $g(k)$ are found to be 10 and 1000, respectively. Furthermore, it is assumed that the functions have an offset of 500 to achieve more dispersed values. As a result, the functions can be written as $f(k) = 500 + a\ln(k)$, $g(k) = 500 + b\ln(k)$, where $f(3) = 10$ and $g(3) = 1000$. Therefore,

$$f(k) = 500 - 446.02\ln(k),$$
$$g(k) = 500 + 455.12\ln(k), \tag{4.8}$$

which are shown in Fig. 4.2. When the pulse amplitudes are coded by (4.6) and (4.8), the sum of pulses forms $\omega_k^{nl,\text{cod}}$ as shown in Fig. 4.1. Then, $\omega_k^{nl,\text{cod}}$ is added to the no-load frequency of the corresponding inverter, ω_k^{nl}.

Each pulse creates a frequency deviation, which is measured in Step 3. The
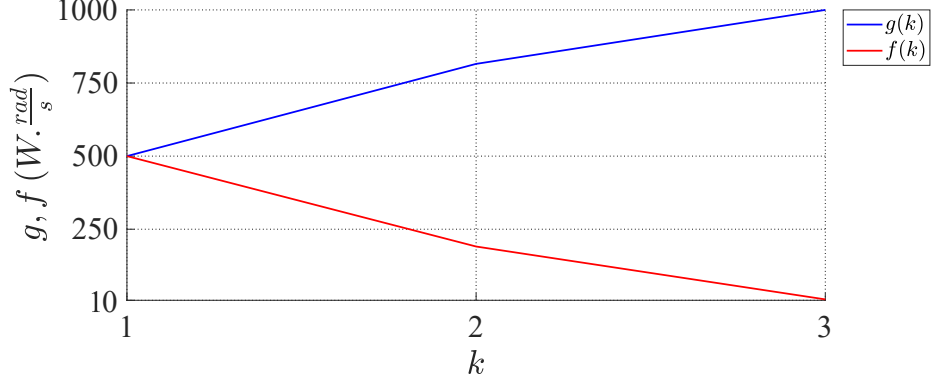
Figure 4.2: $f(k)$ and $g(k)$ functions in the second step of OID.

frequency deviation measurement is enabled by the very-light load detection in Step 1, which changes the enable signal En_k to one.

Finally, in Step 4, the frequency deviation ratio is calculated, which approximately matches a row in the lookup table of the online inverters, shown in Table 4.1. Thus, the vector of the online inverters is obtained. It is worth mentioning that the lookup table is obtained offline according to (4.7), and it may contain as many cases as needed depending on the total number of inverters, which already exist in the system or will be possibly added in the future. In case that some inverters are offline, their corresponding amounts of $f(k)$ and $g(k)$ are set to zero in the calculation of (4.7).

Table 4.1: Lookup table for OID.

Case	Inverter 1	Inverter 2	Inverter 3	$\dfrac{\Delta\omega'}{\Delta\omega}$
1	1	0	0	1
2	0	1	0	4.2729
3	0	0	1	100
4	1	1	0	1.9041
5	1	0	1	2.9412
6	0	1	1	9.0392
7	1	1	1	3.3038

60

For instance, Case 6 of Table 4.1 is given by:

$$\frac{\Delta\omega'}{\Delta\omega} = \frac{g(2) + g(3)}{f(2) + f(3)} = 9.0392. \tag{4.9}$$

4.3 Application of OID in System Efficiency Improvement

Fig. 4.3 illustrates how the proposed OID is integrated with the decentralized control system presented in Chapter 3 to detect the online inverters in very-light load situations and enhance the system efficiency. Once the online inverters are detected, the inverter with the lowest rated power, e.g. the jth inverter, should solely supply the loads and restore the frequency at 60 Hz. For this purpose, as illustrated in Fig. 4.3,
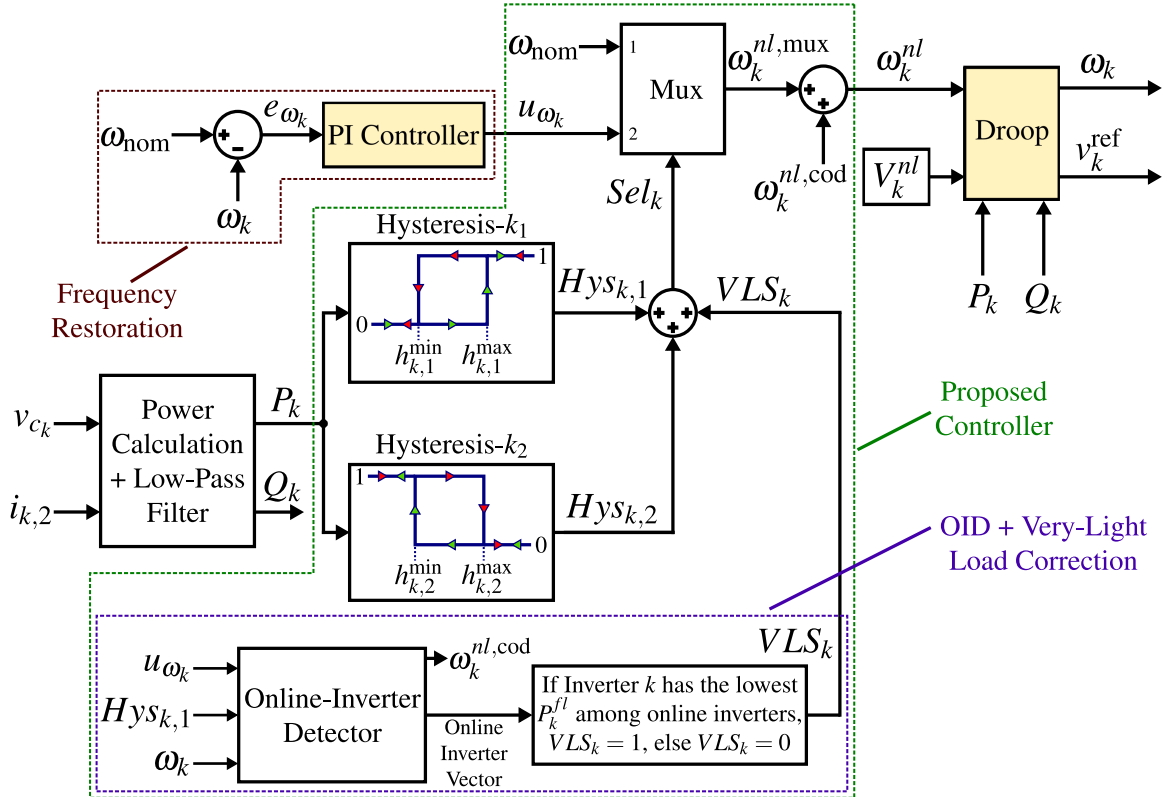
Figure 4.3: Proposed controller of the kth inverter integrated with OID and very-light load correction.

the very-light load correction signal of that inverter VLS_j changes from 0 to 1, and the Mux selector Sel_j is set to 2. In this case, $\omega_j^{nl} = u_{\omega_j}$, and the frequency is restored at 60 Hz by Inverter j.

Fig. 4.4 illustrates the droop characteristics of the inverters in the very-light load situation. First, the inverters start to share the power proportionally, as depicted in Fig. 4.4(a). Then, the OID is activated to detect the online inverters, where Case 7 of Table 4.1 is detected, which means all three inverters are online. Since Inverter 1 has the lowest rated power, $VLS_1 = 1 \Rightarrow Sel_1 = 2$. Hence, only Inverter 1 supplies the load, as shown in Fig. 4.4(b).

(a) $P_k < 0.3P_k^{fl} \Rightarrow P_L = P_1 + P_2 + P_3$.

(b) $VLS_1 : 0 \to 1 \Rightarrow Sel_1 : 1 \to 2 \Rightarrow P_L = P_1,\ P_2 = P_3 = 0$.
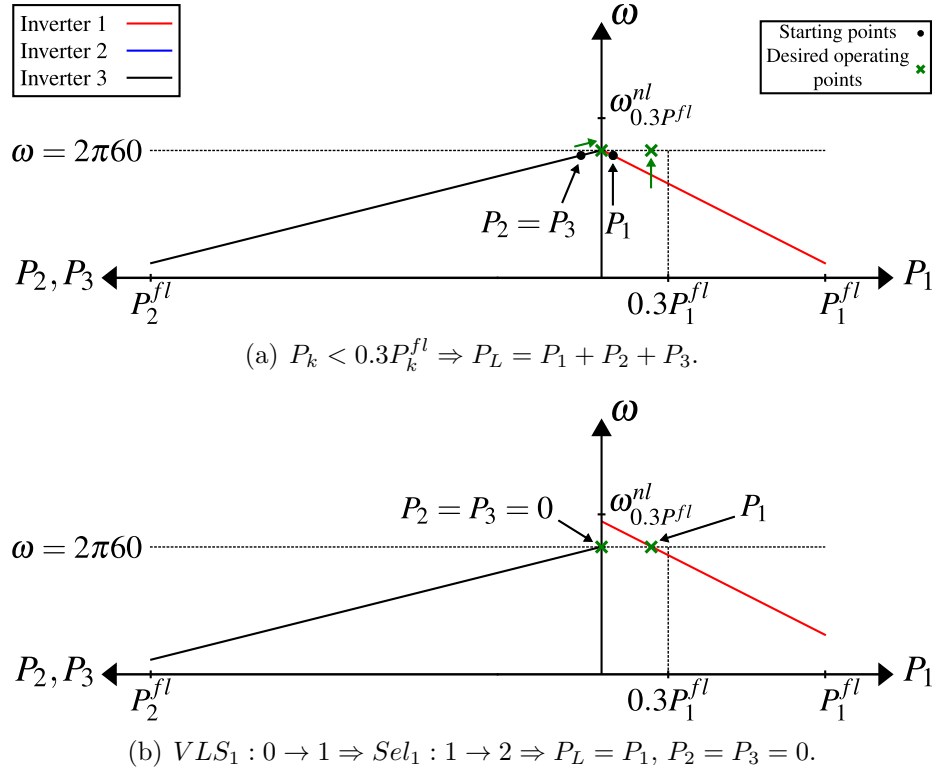
Figure 4.4: Droop characteristics of the inverters operating in a very-light load situation at (a) the beginning, and (b) the final operating points.

4.4 Simulation Results

A grid-forming inverter system with three single-phase parallel inverters with the parameter values represented in Table 4.2 is simulated at three different online-inverter scenarios to evaluate the performance of the proposed controller in improving the overall system efficiency. Since Inverter 3 is identical to Inverter 2, its parameters are the same as that of Inverter 2. Moreover, the efficiencies of the conventional and proposed methods are obtained and compared using (3.6), (3.7).

Table 4.2: System parameters.

Parameter	Value	Parameter	Value
ω_{nom}	$2\pi 60$ rad/s	ω_{cf}	131.58 rad/s
P_1^{fl}	1 kW	P_2^{fl}	2 kW
$V_{dc,1}$	200 V	$V_{dc,2}$	200 V
$L_{1,1}$	2 mH	$L_{2,1}$	3 mH
$L_{1,2}$	2 mH	$L_{2,2}$	2 mH
C_1	2.2 µF	C_2	1 µF
V_1^{nl}	$120\sqrt{2}$ V	V_2^{nl}	$120\sqrt{2}$ V
m_1	0.0038 rad/W.s	m_2	0.0019 rad/W.s
n_1	0.0051 V/VAr	n_2	0.0025 V/VAr
L_1^{vir}	5.04 mH	L_2^{vir}	2.52 mH
b_1^{prop}	0.8	b_2^{prop}	0.4
b_1^{int}	300	b_2^{int}	150
$h_{1,1}^{\text{min}}$	270 W	$h_{2,1}^{\text{min}}$	540 W
$h_{1,1}^{\text{max}}$	330 W	$h_{2,1}^{\text{max}}$	660 W
$h_{1,2}^{\text{min}}$	720 W	$h_{2,2}^{\text{min}}$	1440 W
$h_{1,2}^{\text{max}}$	880 W	$h_{2,2}^{\text{max}}$	1760 W

4.4.1   First Scenario: Three Online Inverters

The first scenario involves three online parallel inverters. As shown in Fig. 4.5, initially, the inverters are connected to a 0.2 kW load at $t = 0.2$ s. Then, the load increases to 1.2 kW, 3 kW, and 5 kW at $t = 3$ s, $t = 5$ s, and $t = 6$ s, respectively. Afterwards, the load drops to 1.5 kW at $t=7$ s. Finally, at $t=8$ s, the load becomes 0.5 kW.

Fig. 4.5(a) compares the overall efficiency of the system operating under the proposed and conventional load-sharing methods. It is observed that during the steady-state conditions, the efficiency of the proposed method is higher than or equal to that of the conventional method. In light-load situations, i.e. at $1\ s \leq t \leq 3\ s$ and $9\ s \leq t \leq 11\ s$, the efficiency improvement can be as much as 14%. Additionally, at $5\ s \leq t \leq 6\ s$, the efficiencies of both methods are close to the maximum value of 96%, and from $t=6\ s$ to $t=7\ s$, all of the inverters are operating at almost full-load power. Hence, the efficiency cannot be further improved in the mentioned time intervals. Nevertheless, there are two types of transient efficiency drops in the proposed method. The first type is during OID detection periods and is resolved quickly when the online inverters are detected. The second type, which occurs for a very short period of time, is during the activation and deactivation of the inverters.

Fig. 4.5(b) illustrates the active power characteristics of the inverters for the conventional and proposed methods. At $t=0.2$ s, a 0.2 kW load, considered as a very-light load, is connected to the system and the system initially operates in *Mode 3*. The OID detects the very-light load situation, and it is automatically activated at $t \approx 0.6$ s to detect the online inverters. Since this scenario corresponds to Case 7 of Table 4.1, i.e. all of the inverters are online, Inverter 1 which has the lowest rated power supplies the load. At $t=3$ s, the load jumps to 1.2 kW. In this case, Inverter 1 cannot solely supply the load, and Inverter 2 is activated due to having a smaller inverter number than Inverter 3 [85]. Next, the load changes to 3 kW at $t=5$ s. In this case,
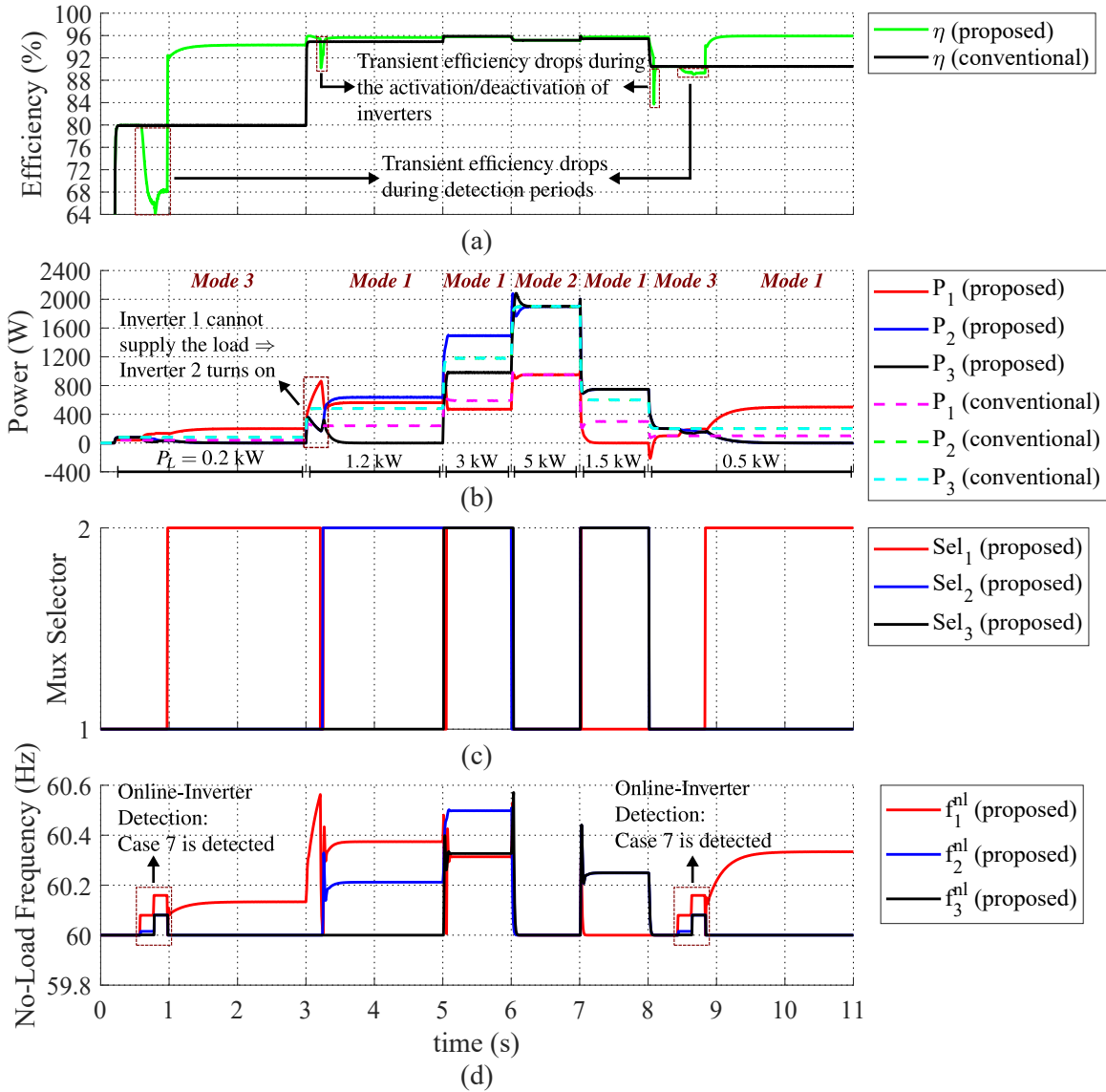
Figure 4.5: Efficiency comparison between the proposed and conventional methods at different load levels when all inverters are online: (a) system efficiencies, (b) inverter active power injections, (c) Mux selector signals, and (d) inverter no-load frequencies.

all three inverters are activated to supply the load; since all inverters operate within the desired power range, the system is in *Mode 1.* Then, the load increases to 5 kW at $t = 6$ s, which is considered as a very-heavy load. Now, the mode of the system changes to *Mode 2.* Thus, the inverters share the power proportionally similar to the conventional droop method. Furthermore, at $t = 7$ s, the load drops to 1.5 kW. It is observed that the power of Inverter 1 drops below $h_{1,1}^{\min}$, and the inverter power is reduced to zero. On the other hand, Inverter 2 and Inverter 3 inject 0.75 kW each to supply the load. Eventually, the load turns to 0.5 kW at $t=8$ s. In this situation, the load is initially considered to be very light since $P_k < 0.3P_k^{fl}$. Hence, the OID is activated and detects Case 7 of Table 4.1. Thus, Inverter 1 solely supplies the load, and when P_1 enters the desired power range, the mode changes to *Mode 1.*

Fig. 4.5(c) depicts the Mux selector signals Sel_k. During the very-light load situations that Inverter 1 supplies the load, according to Fig. 4.3, it is concluded that $Hys_{1,2} = 1$, $VLS_1 = 1$, and $Sel_1 = 2$. Moreover, when the system is in *Mode 1*, the Mux selector signals are set to $Sel_k=2$ for the inverters operating within the desired power range. Additionally, in *Mode 2*, the selector signals of all multiplexers are set to one, i.e. $Sel_k=1$, for $k=1,2,3$.

Fig. 4.5(d) demonstrates the inverter no-load frequencies. The proposed controller of each inverter alters its no-load frequency to restore the frequency at 60 Hz if the inverter operates within the desired power range. However, when the 5 kW load is connected at $t=6$ s, the system mode changes to *Mode 2* where the no-load frequencies of all inverters are set to $\omega_k^{nl} = 2\pi60$ rad/s, $k = 1, 2, 3$. Furthermore, the impacts of the temporary no-load frequency pulses $\omega_k^{nl,\text{cod}}$, generated by the OID, on the no-load frequency characteristics are observed at 0.6 $s \leq t \leq 1$ s and at 8.4 $s \leq t \leq 8.8$ s.

4.4.2 Second Scenario: Two Identical Online Inverters

In the second scenario, Inverter 1 is offline during the entire simulation period, and the identical inverters in the system supply the load. As illustrated in Fig. 4.6, a 0.2 kW load is connected at $t = 0.2$ s. Then, the load increases to 2 kW and 4 kW at $t = 3$ s and $t = 4$ s, respectively. Subsequently, the load drops to 0.5 kW at $t = 5$ s. Fig. 4.6(a) compares the overall efficiency of the system operating under the proposed and conventional load-sharing methods. Similar to the first scenario, the efficiency of the proposed method is higher than or equal to that of the conventional method during the steady-state conditions. In light-load situations, i.e. at $1s \leq t \leq 3s$ and $6s \leq t \leq 8s$, the efficiency can be improved as much as 7.25%. Additionally, during $t = 3s$ and $t = 4s$, both of the efficiencies are equal to the maximum value of 96%; and from $t = 4s$ to $t = 5s$, both of the inverters are operating at almost full-load power. Thus, the efficiency cannot be further improved in the mentioned periods. Compared with the first scenario, it can be seen that the transient efficiency drops in the second scenario are inconspicuous.

The active power characteristics of the inverters under the conventional and proposed methods are shown in Fig. 4.6(b). When a 0.2 kW load is connected at $t = 0.2$ s, the system operates in *Mode 3* since the load implies a very-light load situation. The OID is activated at $t \approx 0.6$ s to detect the online inverters. Since only Inverter 2 and Inverter 3 are online, the OID successfully detects that Case 6 of Table 4.1 has occurred. In this case, since both inverters have the same rated power, only Inverter 2 supplies the load due to having a smaller inverter number compared with Inverter 3 [85]. Next, the load changes to 2 kW at $t = 3$ s, and the system goes to *Mode 1*. Thus, Inverter 3 is activated to contribute to load sharing as well. Subsequently, the load increases to a very-heavy load of 4 kW at $t = 4$ s. Therefore, the system mode changes to *Mode 2*, and the inverters share the power proportionally similar to the conventional droop method. Finally, at $t = 5$ s, the load reduces to
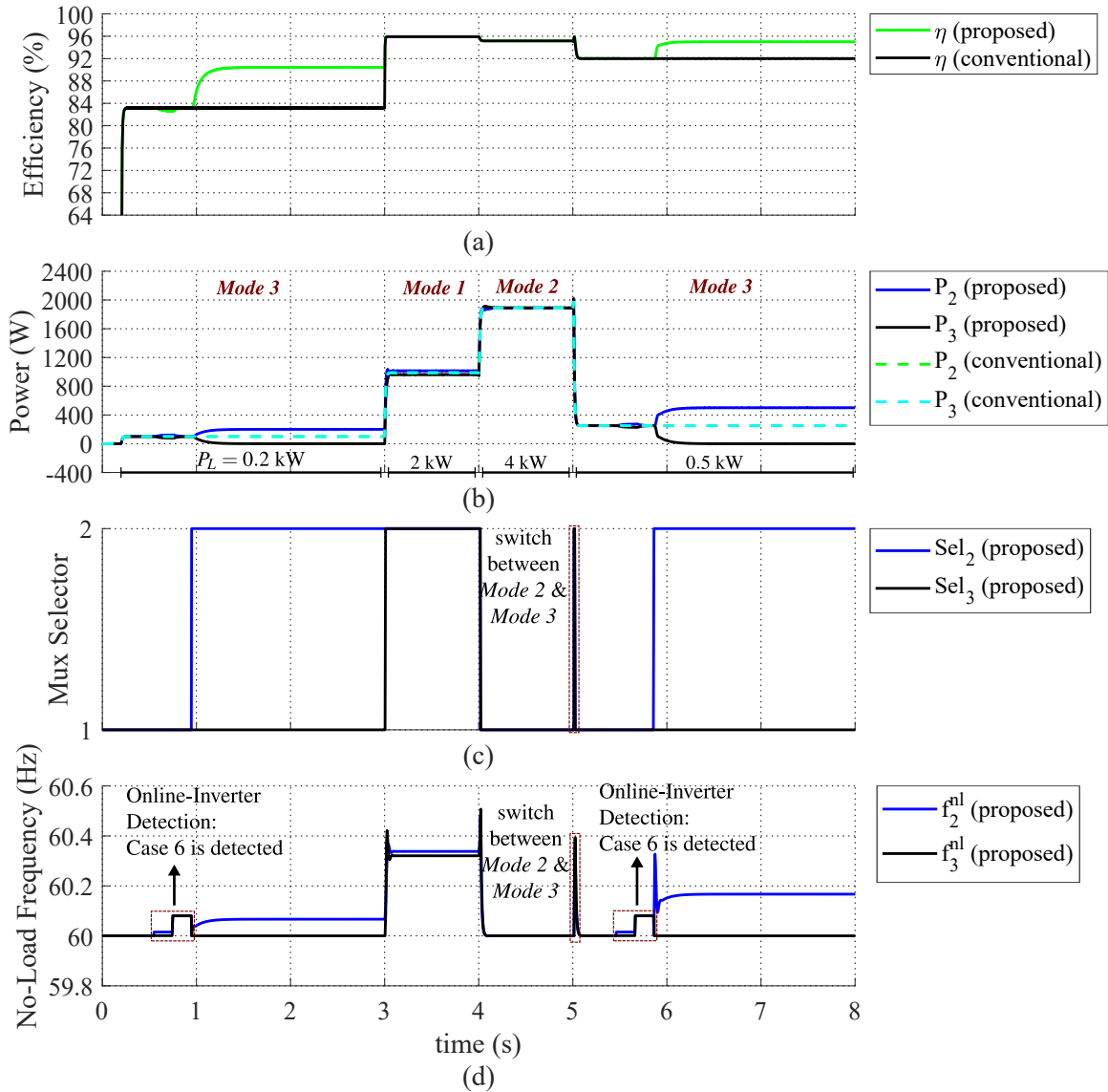
Figure 4.6: Efficiency comparison between the proposed and conventional methods at different load levels, when two identical inverters are online: (a) system efficiencies, (b) inverter active power injections, (c) Mux selector signals, and (d) no-load frequencies.

0.5 kW that is considered as a very-light load for the identical inverters, and the system returns to *Mode 3*. Hence, the OID is activated and detects Case 6 of Table 4.1. Consequently, only Inverter 2 supplies the load.

Fig. 4.6(c) depicts the Mux selector signals. Similar to the first scenario, during the very-light load situations that Inverter 2 supplies the load, $Hys_{2,2}=1$, $VLS_2=1$, and $Sel_2=2$. Also, when the system goes to *Mode 1* at $t=3$ s, the Mux selectors of the online inverters are set to $Sel_2=Sel_3=2$ since they operate within the desired power range. Additionally, from $t=4$ s to $t=5$ s that the system operates in *Mode 2*, the Mux selectors are $Sel_2=Sel_3=1$. As shown in Fig. 4.6(c), at $t=5$ s, the load suddenly changes from 4 kW to 0.5 kW that leads to a mode change from *Mode 2* to *Mode 3*. In this case, P_2 and P_3 first fall below $h_{2,2}^{\min}=h_{3,2}^{\min}$ that results in $Hys_{2,2}=Hys_{3,2}=1$. Thus, the Mux selectors change to $Sel_2=Sel_3=2$. Then, P_2 and P_3 quickly drop below $h_{2,1}^{\min}=h_{3,1}^{\min}$ leading to $Sel_2=Sel_3=1$. Eventually, as mentioned earlier, the OID detects Case 6 of Table 4.1, and Inverter 2 is assigned to solely supply the load, accordingly.

Fig. 4.6(d) shows the inverter no-load frequencies. The dynamics of the no-load frequencies are similar to the first scenario. In addition, the impacts of the temporary frequency pulses $\omega_k^{nl,\text{cod}}$, generated by the OID, on the no-load frequency characteristics can be seen at at 0.6 $s\leq t \leq 1$ s and at 5.4 $s \leq t \leq 5.8$ s.

4.4.3   Third Scenario: Transition from Two to Three Online Inverters

The third scenario is a combination of the first and second scenarios to evaluate the performance of the OID in case that Inverter 1 is back online. As depicted in Fig. 4.7, initially, a 0.2 kW load is connected at $t=0.2$ s. Then, the load increases to 2 kW, at $t=2$ s. Finally, the load reduces to 0.4 kW at $t=3.5s$. Inverter 1 is offline at the beginning of the simulation. It starts synchronizing with the other

inverters at $t = 2.2$ s, and connects to the system at $t = 2.8$ s. The overall system efficiency under the proposed and conventional load-sharing methods are presented in Fig. 4.7(a). Similar to the previous scenarios, the efficiency of the proposed method is higher than or equal to that of the conventional method during the steady-state conditions. Moreover, the two types of the transient efficiency drops explained in the first scenario are repeated in the third scenario. However, they are resolved in a short period of time.

Fig. 4.7(b) depicts the active powers of the inverters under the conventional and proposed methods. Initially, a 0.2 kW load is connected at $t = 0.2$ s, and the system is operating in *Mode 3*. At $t \approx 0.6$ s, the OID generates the temporary frequency pulses to detect the online inverters, and Case 6 of Table 4.1 is detected at $t \approx 1$ s. Thus, Inverter 2 supplies the load merely. Afterwards, the load increases to 2 kW at $t = 2$ s, and the mode changes to *Mode 1*. Hence, Inverter 3 is activated to help supply the load. At $t = 2.8$ s when Inverter 1 is back online, if the proposed method is employed, no change is observed in the active power injections since the frequency is restored at 60 Hz by the other inverters. On the contrary, in the conventional method, as the inverters share the power proportional to their power ratings, Inverter 1 starts to supply the load along with the other inverters. Finally, the load turns to 0.4 kW at $t = 3.5$ s, and the system returns to *Mode 3*. The OID is activated at $t \approx 3.9$ s, and, this time, it detects Case 7 of Table 4.1. Consequently, Inverter 1 solely supplies the load, and the mode changes to *Mode 1*.

The Mux selector signals are shown in Fig. 4.7(c). The operation principles of the signals are the same as the previous scenarios. Furthermore, Fig. 4.7(d) presents the no-load frequencies. The transient pulses produced by the OID can be observed at 0.6 $s \le t \le 1$ s and at 3.9 $s \le t \le 4.3$ s. Moreover, Inverter 1 synchronizes with the system between $t = 2.2$ s and $t = 2.8$ s.
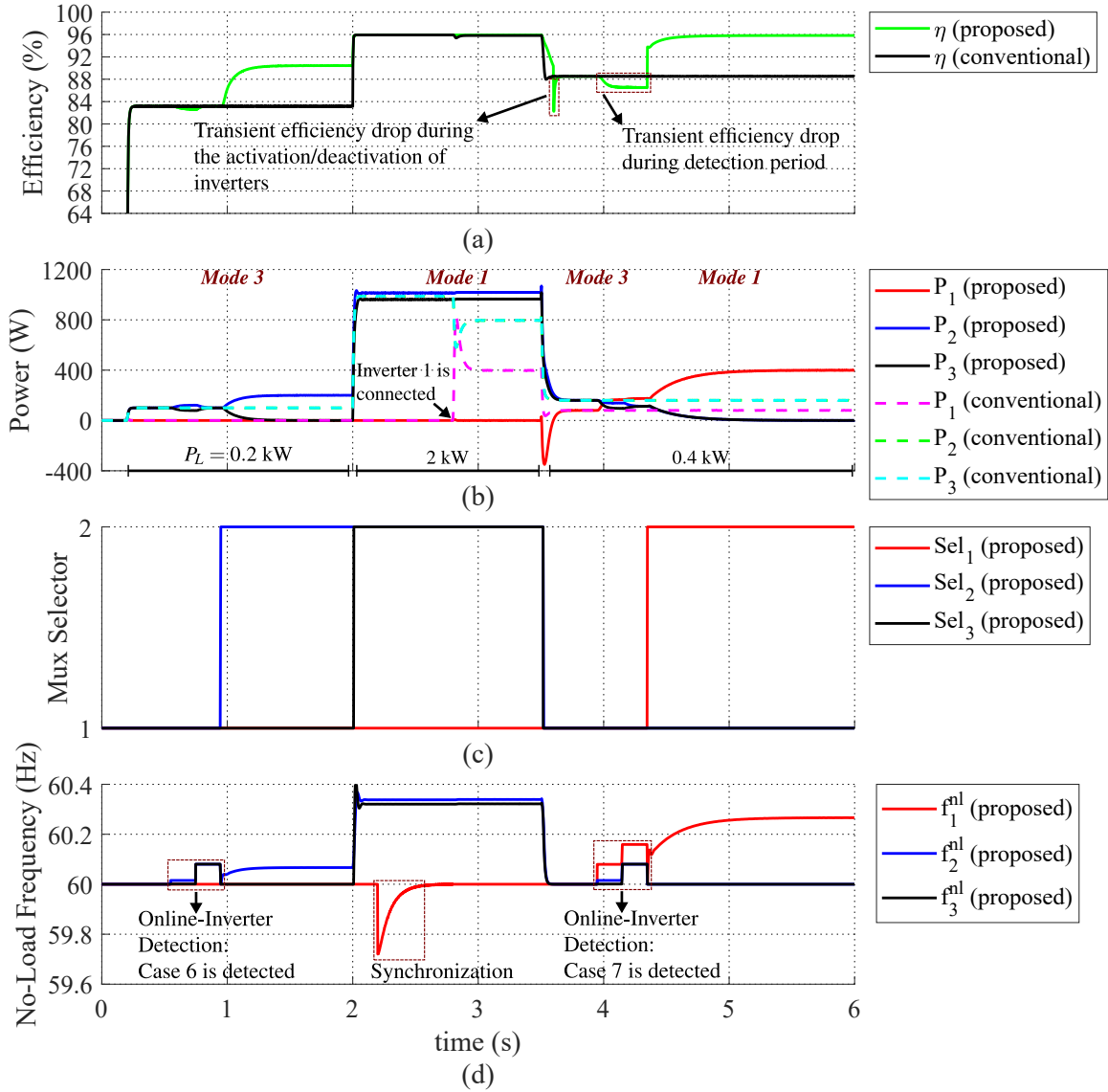
Figure 4.7: Efficiency comparison between the proposed and conventional methods at different load levels during the transition from two to three online inverters: (a) system efficiencies, (b) inverter active power injections, (c) Mux selector signals, and (d) no-load frequencies.

4.4.4 Overall System Efficiency Curve Improvement

Fig. 4.8 compares the overall system efficiency curves of the proposed and conventional methods within the entire range of loads that the system can support with three online inverters, i.e. $0 \text{ kW} \leq P_L \leq 5 \text{ kW}$. The proposed method significantly increases the overall system efficiency at light loads. This is achieved because the proposed method maintains the power injection of each inverter within the proper power range. In other words, in the proposed method, the load-sharing is performed based on the load profile and the rated powers of online inverters. As shown in Fig. 4.8, Inverter 1 solely supplies the load until the inverter power reaches to the maximum amount of its desired range. Then, Inverter 2 is activated to help Inverter 1 supply the load until its power reaches to the maximum amount of its desired range, and so on. It should be noted that at very-heavy loads near 5 kW, the system operates in *Mode 2*, which is similar to the conventional droop strategy, and the efficiency cannot be further improved.
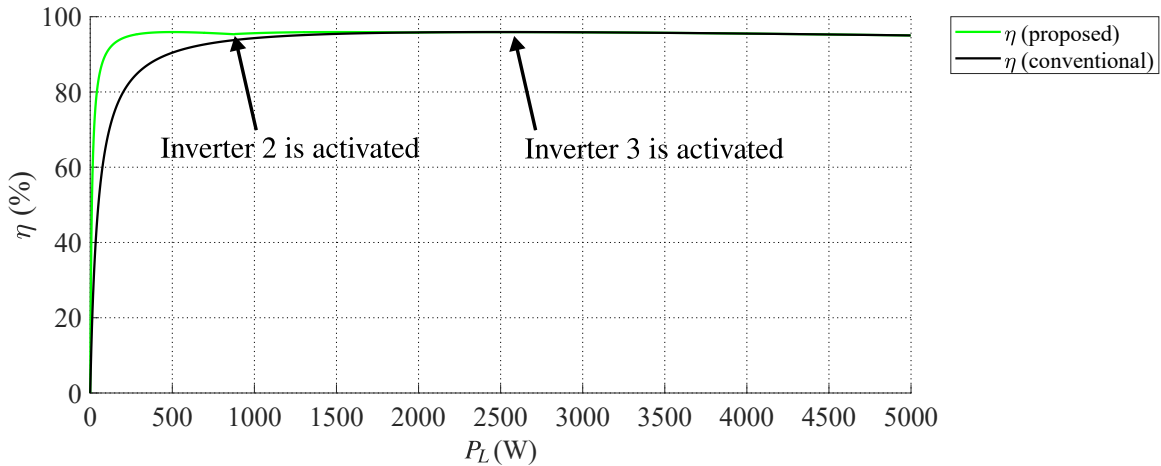
Figure 4.8: Overall system efficiency comparison between the proposed and conventional methods.

4.5   Experimental Results

The experimental results are obtained in two scenarios where two and three inverters are online in the system.

4.5.1   Two Online Inverters

In the first scenario, two single-phase parallel inverters with power ratings of $P_1^{fl} = 200$ W and $P_2^{fl} = 400$ W are connected to the loads via LCL filters. Fig. 4.9 shows the experimental results when the inverters are operating in *Mode 1* and *Mode 3*. In the beginning, the load is 40 W which is considered as a very-light load. Thus, Inverter 1 solely supplies the load, and the system is in *Mode 3*. Next, the load increases to 240 W. Since 240 W is higher than $0.8P_1^{fl}$, Inverter 1 cannot supply the load individually, and a portion of the demanded power is supplied by Inverter 2, indicating that the system is operating in *Mode 1*. Eventually, the load drops to 40 W. As the mode changes from *Mode 1* to *Mode 3*, the OID is activated and detects that both inverters are online. Hence, Inverter 1 starts to solely supply the load due to having the lowest rated power. In addition to the active power injections, the load-side inductor currents, capacitor voltages, and no-load frequencies are shown in Fig. 4.9.

It should be noted that the transient time of turning on Inverter 2, i.e. 400 ms < t < 600 ms, is considered as a fast internal transient which is not sensed externally by the load. Therefore, the load power remains constant during the process of inverters turning on and off since the load is supplied by the sum of P_1 and P_2 by the droop control strategy and the load power reaches its steady-state value much faster than the transient time of turning on Inverter 2. It is worth mentioning that since the inverters proportionally share the power similar to the conventional droop strategy in *Mode 2*, this mode is not included in the experimental results.
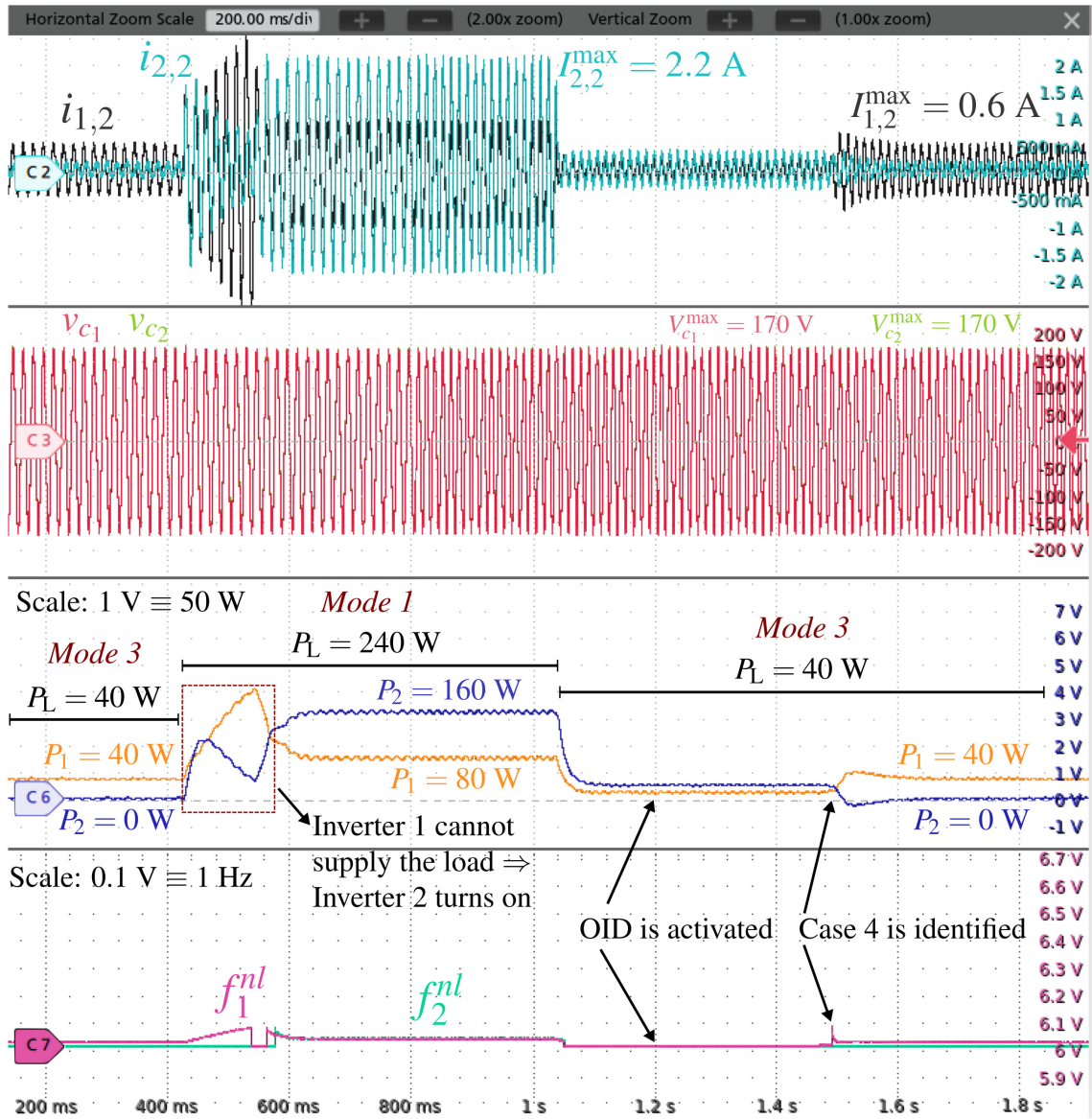
Figure 4.9: Experimental results with two inverters: performance of the OID in improving the efficiency by deactivating the unnecessary inverter in *Mode 3*.

In the experimental results depicted in Fig. 4.9 and Fig. 3.19, it is observed that the power distribution among the inverters is different for the 240 W load. The reason is that the power distribution among the inverters depends on the previous load, system mode, and the changing rate of no-load frequencies. In Fig. 4.9, a very-light load of 40 W is connected at the beginning and Inverter 1 is solely supplying the load in *Mode 3*. Then, the load changes to 240 W and the system mode changes to *Mode 1*, where Inverter 1 and Inverter 2 inject 80 W and 160 W, respectively. In Fig. 3.19, although Inverter 1 is feeding the load at the beginning, its operating mode is *Mode 1*. When the load changes from 100 W to 240 W, while the system remains in *Mode 1*, Inverter 1 injects 70 W and Inverter 2 supplies 170 W.

Considering the efficiency curve depicted in Fig. 3.5, the experimental system efficiency under the proposed and conventional methods can be compared by Table 4.3. It is observed that the system efficiency is improved at light loads in comparison with the conventional power sharing. Furthermore, there is no difference between the system efficiency under the proposed method with respect to the inverter power distributions in Fig. 4.9 and Fig. 3.19 at 240 W.

Table 4.3: Experimental efficiency comparison between the conventional and proposed methods for two inverters.

Efficiency	$P_1 = 40$ W $P_2 = 0$ W	$P_1 = 80$ W $P_2 = 160$ W	$P_1 = 100$ W $P_2 = 0$ W	$P_1 = 70$ W $P_2 = 170$ W
η_1	94.3%	95.8%	96%	95.7%
η_2	-	95.8%	-	95.85%
$\eta_{sys,prop}$	94.3%	95.8%	96%	95.8%
$\eta_{sys,conv}$	86.5%	95.8%	93.6%	95.8%

4.5.2 Three Online Inverters

For the second scenario, three single-phase parallel inverters with power ratings of $P_1^{fl} = 200$ W and $P_2^{fl} = P_3^{fl} = 400$ W are connected to the loads via LCL filters. Fig. 4.10 shows the experimental results of the system with three online inverters operating in *Mode 1* and *Mode 3*. First, the load is 40 W which is considered as a very-light load. Hence, Inverter 1 solely supplies the load, and the system operates in *Mode 3*. Next, the load increases to 240 W. Since Inverter 1 cannot supply the load individually, Inverter 2 starts to supply the load, and the system mode changes to *Mode 1*. Subsequently, the load jumps to 360 W which should be fed by all three inverters. Finally, the load drops to 40 W. As the mode changes from *Mode 1* to *Mode 3*, the OID is activated and detects that all inverters are online. Thus,
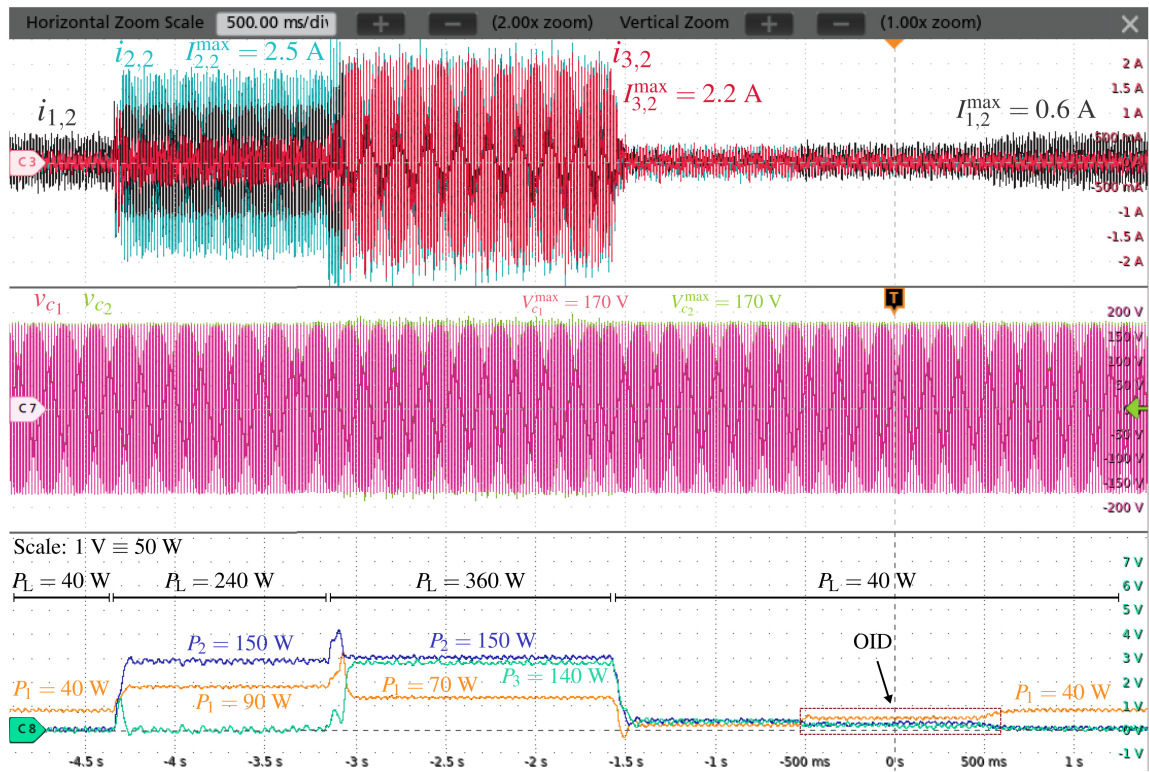
Figure 4.10: Experimental results with three online inverters: performance of the OID and proposed controller in improving the efficiency by deactivating the unnecessary inverters.

Table 4.4: Experimental efficiency comparison between the conventional and proposed methods for three inverters.

Efficiency	$P_1 = 40$ W $P_2 = 0$ W $P_3 = 0$ W	$P_1 = 90$ W $P_2 = 150$ W $P_3 = 0$ W	$P_1 = 70$ W $P_2 = 150$ W $P_3 = 140$ W	$P_1 = 40$ W $P_2 = 0$ W $P_3 = 0$ W
η_1	94.3%	95.9%	95.7%	94.3%
η_2	-	95.75%	95.75%	-
η_3	-	-	95.7%	-
$\eta_{sys,prop}$	94.3%	95.8%	95.72%	94.3%
$\eta_{sys,conv}$	80%	94.9%	95.7%	80%

Inverter 1 starts to supply the load solely due to having the lowest rated power. In addition to the active power injections, the load-side inductor currents and the LCL-filter capacitor voltages are shown in Fig. 4.10.

Considering the efficiency curve depicted in Fig. 3.5, the experimental system efficiency under the proposed and conventional methods can be compared using Table 4.4. It is observed that the efficiency improvement is more significant in the second scenario in comparison with the first scenario.

4.6   Summary

A decentralized online-inverter detection (OID) method is proposed in this chapter to detect the online parallel GFM inverters in very-light load situations, and ensure a minimum number of inverters with the lowest rated powers will supply the loads to achieve a higher efficiency. The proposed method is based on a transient frequency deviation created by the inverters, and features reliability, modularity, and flexibility. Therefore, more inverters can be added to the system without the requirement to reprogram the existing inverters. Furthermore, the proposed method improves the reliability and system efficiency in cases where some of the inverters are offline, im-

plying no single point of failure. The proposed method is integrated with the control system described in Chapter 3, and different simulation scenarios of online inverters along with experimental results are provided to prove the effectiveness of the method.

Chapter 5

Summary and Future Work

In this thesis, modeling, control design, efficiency improvement and experimental verification of grid-forming (GFM) inverter systems operating in standalone mode are presented. The objective of the thesis is to propose a decentralized, reliable, and modular control system to improve the overall system efficiency of parallel inverters based on a modified droop strategy. The main contributions and conclusions of this thesis are summarized below.

5.1   Summary of Contributions

(i) A state-space modeling and control system for a single-phase inverter operating in standalone mode are presented. The nested-loop control system, containing current, voltage, and harmonics controllers, is designed based on the linear quadratic tracking (LQT) optimal control method. The control system exhibits a satisfactory performance in tracking the reference signals and rejecting the unwanted harmonics in case of linear and nonlinear loads. Furthermore, a THD of 1.65% is obtained in a case where a nonlinear load is connected to the system.

(ii) A decentralized modified droop strategy is proposed in this thesis to improve

the overall system efficiency of parallel GFM inverters. The proposed method maintains the output power of the inverters within a desired range that corresponds to a high efficiency by reducing the power of the unnecessary inverters to zero. The proposed method does not need any communication links among the inverters, and it features reliability, modularity, and flexibility. Furthermore, the lifetimes of inverters with higher rated powers are extended by the proposed method. A system with three parallel single-phase inverters is studied in this thesis to evaluate the performance of the proposed method in enhancing the system efficiency.

(iii) The stability verification of the system within the operating range of the no-load frequencies is conducted to ensure that the proposed control system operates in a stable region.

(iv) At very-light load situations, the inverters cannot operate within the desired power range. Therefore, a decentralized online-inverter detection (OID) method is developed and added to the efficiency improvement control system to detect the online inverters and select a minimum number of inverters to supply the loads and achieve a higher efficiency. Since the proposed OID is decentralized and modular, more inverters can be added to the system without the requirement to reprogram the existing inverters. Furthermore, the proposed OID improves the reliability and system efficiency without any single point of failure. Different simulation scenarios of online inverters and experimental results verify the effectiveness of the OID and the modified droop method.

(v) It is observed that the proposed modified droop strategy, integrated with the OID, can improve the system efficiency by up to 14% at light loads compared with the conventional droop method.

5.2 Suggested Future Work

There are a number of directions that this research can be taken to; some of the most promising ones are suggested as follows:

(i) The reference tracking and harmonic rejection performance of the proposed nested-loop controller in Chapter 2 could be investigated in grid-connected mode, and modifications to the structure of the harmonics controller could be made if necessary.

(ii) The application of the proposed efficiency improvement method could be assessed in high-power microgrids by including the line impedances.

(iii) The proposed modified droop strategy could be extended to enhance the efficiency of parallel converters in dc systems as well.

(iv) The OID method is a general approach to detect the online inverters in a standalone microgrid. The extension of OID to other applications such as energy management and cost optimization could be further investigated.

Bibliography

[1] R. Rosso, X. Wang, M. Liserre, X. Lu, and S. Engelken, "Grid-forming converters: an overview of control approaches and future trends," in *2020 IEEE Energy Conversion Congress and Exposition (ECCE)*. IEEE, 2020, pp. 4292–4299.

[2] R. Rosso, X. Wang, M. Liserre, X. Lu, and S. Engelken, "Grid-forming converters: Control approaches, grid-synchronization, and future trends-a review," *IEEE Open Journal of Industry Applications*, 2021.

[3] Q. Shafiee, J. M. Guerrero, and J. C. Vasquez, "Distributed secondary control for islanded microgrids—a novel approach," *IEEE Transactions on power electronics*, vol. 29, no. 2, pp. 1018–1031, 2013.

[4] J. Rocabert, A. Luna, F. Blaabjerg, and P. Rodriguez, "Control of power converters in ac microgrids," *IEEE transactions on power electronics*, vol. 27, no. 11, pp. 4734–4749, 2012.

[5] A. K. Sahoo, K. Mahmud, M. Crittenden, J. Ravishankar, S. Padmanaban, and F. Blaabjerg, "Communication-less primary and secondary control in inverter-interfaced ac microgrid: An overview," *IEEE Journal of Emerging and Selected Topics in Power Electronics*, 2020.

[6] S. Yazdani, M. Ferdowsi, M. Davari, and P. Shamsi, "Advanced current-limiting and power-sharing control in a pv-based grid-forming inverter under unbalanced

grid conditions," *IEEE Journal of Emerging and Selected Topics in Power Electronics*, vol. 8, no. 2, pp. 1084–1096, 2019.

[7] R. H. Lasseter, Z. Chen, and D. Pattabiraman, "Grid-forming inverters: A critical asset for the power grid," *IEEE Journal of Emerging and Selected Topics in Power Electronics*, vol. 8, no. 2, pp. 925–935, 2019.

[8] M. Ebrahimi, S. A. Khajehoddin, and M. Karimi-Ghartemani, "Fast and robust single-phase *dq* current controller for smart inverter applications," *IEEE transactions on power electronics*, vol. 31, no. 5, pp. 3968–3976, 2015.

[9] M. Ebrahimi and S. A. Khajehoddin, "Fixed switching frequency generalized peak current control (gpcc) of dc–ac converters," *IEEE Transactions on Power Electronics*, vol. 32, no. 8, pp. 6605–6616, 2016.

[10] S. Wang, J. Liu, Z. Liu, T. Wu, and B. Liu, "Efficiency-based optimization of steady-state operating points for parallel source converters in stand-alone power system," in *2016 IEEE 8th International Power Electronics and Motion Control Conference (IPEMC-ECCE Asia)*.   IEEE, 2016, pp. 163–170.

[11] J.-H. Teng, S.-H. Liao, W.-H. Huang, and C.-C. Chiang, "Smart control strategy for conversion efficiency enhancement of parallel inverters at light loads," *IEEE Transactions on Industrial Electronics*, vol. 63, no. 12, pp. 7586–7596, 2016.

[12] G. Chen and X. Cai, "Adaptive control strategy for improving the efficiency and reliability of parallel wind power converters by optimizing power allocation," *IEEE Access*, vol. 6, pp. 6138–6148, 2018.

[13] Y. Han, H. Li, P. Shen, E. A. A. Coelho, and J. M. Guerrero, "Review of active and reactive power sharing strategies in hierarchical controlled microgrids," *IEEE Transactions on Power Electronics*, vol. 32, no. 3, pp. 2427–2451, 2016.

[14] S. A. Khajehoddin, M. Karimi-Ghartemani, A. Bakhshai, and P. Jain, "A power control method with simple structure and fast dynamic response for single-phase grid-connected dg systems," *IEEE Transactions on Power Electronics*, vol. 28, no. 1, pp. 221–233, 2012.

[15] S. A. Khajehoddin, M. Karimi-Ghartemani, P. K. Jain, and A. Bakhshai, "Dc-bus design and control for a single-phase grid-connected renewable converter with a small energy storage component," *IEEE Transactions on Power Electronics*, vol. 28, no. 7, pp. 3245–3254, 2012.

[16] X. Yu, A. M. Khambadkone, H. Wang, and S. T. S. Terence, "Control of parallel-connected power converters for low-voltage microgrid—part i: A hybrid control architecture," *IEEE Transactions on Power Electronics*, vol. 25, no. 12, pp. 2962–2970, 2010.

[17] L. Zhang, K. Sun, H. Hu, and Y. Xing, "A system-level control strategy of photovoltaic grid-tied generation systems for european efficiency enhancement," *IEEE transactions on power electronics*, vol. 29, no. 7, pp. 3445–3453, 2013.

[18] SolarEdge. SolarEdge se3000h-us [Datasheets]. [Online]. Available: https://www.solaredge.com

[19] Solar-Edge. SolarEdge inverter efficiency [Datasheets]. [Online]. Available: https://www.solaredge.com

[20] Delta. Delta m6-tl-us [Datasheets]. [Online]. Available: https://www.delta-americas.com

[21] Huawei. Huawei sun2000-10ktl-usl0 [Datasheets]. [Online]. Available: https://shop.frankensolar.ca

[22] J. M. Guerrero, J. C. Vasquez, J. Matas, L. G. De Vicuña, and M. Castilla, "Hierarchical control of droop-controlled ac and dc microgrids—a general approach toward standardization," *IEEE Transactions on industrial electronics*, vol. 58, no. 1, pp. 158–172, 2010.

[23] J. M. Guerrero, J. C. Vasquez, J. Matas, M. Castilla, and L. G. de Vicuña, "Control strategy for flexible microgrid based on parallel line-interactive ups systems," *IEEE Transactions on industrial Electronics*, vol. 56, no. 3, pp. 726–736, 2008.

[24] J. C. Vasquez, J. M. Guerrero, A. Luna, P. Rodríguez, and R. Teodorescu, "Adaptive droop control applied to voltage-source inverters operating in grid-connected and islanded modes," *IEEE transactions on industrial electronics*, vol. 56, no. 10, pp. 4088–4096, 2009.

[25] J. M. Guerrero, L. G. De Vicuna, J. Matas, M. Castilla, and J. Miret, "A wireless controller to enhance dynamic performance of parallel inverters in distributed generation systems," *IEEE Transactions on power electronics*, vol. 19, no. 5, pp. 1205–1213, 2004.

[26] P. C. Loh and D. G. Holmes, "Analysis of multiloop control strategies for lc/cl/lcl-filtered voltage-source and current-source inverters," *IEEE Transactions on Industry Applications*, vol. 41, no. 2, pp. 644–654, 2005.

[27] Z. Li, C. Zang, P. Zeng, H. Yu, S. Li, and J. Bian, "Control of a grid-forming inverter based on sliding-mode and mixed H_2/H_∞ control," *IEEE Transactions on Industrial Electronics*, vol. 64, no. 5, pp. 3862–3872, 2016.

[28] P. Buduma and G. Panda, "Robust nested loop control scheme for lcl-filtered inverter-based dg unit in grid-connected and islanded modes," *IET Renewable Power Generation*, vol. 12, no. 11, pp. 1269–1285, 2018.

[29] J. M. Guerrero, L. G. De Vicuna, J. Matas, M. Castilla, and J. Miret, "Output impedance design of parallel-connected ups inverters with wireless load-sharing control," *IEEE Transactions on industrial electronics*, vol. 52, no. 4, pp. 1126–1135, 2005.

[30] A. Chatterjee and K. B. Mohanty, "A nested control strategy for single phase power inverter integrating renewable energy systems in a microgrid," in *2016 National Power Systems Conference (NPSC)*. IEEE, 2016, pp. 1–6.

[31] N. Saxena, B. Singh, and A. L. Vyas, "Single-phase solar pv system with battery and exchange of power in grid-connected and standalone modes," *IET renewable power generation*, vol. 11, no. 2, pp. 325–333, 2017.

[32] T. C. Green and M. Prodanović, "Control of inverter-based micro-grids," *Electric power systems research*, vol. 77, no. 9, pp. 1204–1213, 2007.

[33] N. A. Ashtiani, S. A. Khajehoddin, and M. Karimi-Ghartemani, "Optimal design of nested current and voltage loops in grid-connected inverters," in *2020 IEEE Applied Power Electronics Conference and Exposition (APEC)*. IEEE, 2020, pp. 2397–2402.

[34] A. Micallef, M. Apap, C. Spiteri-Staines, and J. M. Guerrero, "Mitigation of harmonics in grid-connected and islanded microgrids via virtual admittances and impedances," *IEEE Transactions on Smart Grid*, vol. 8, no. 2, pp. 651–661, 2015.

[35] M. Monfared, S. Golestan, and J. M. Guerrero, "Analysis, design, and experimental verification of a synchronous reference frame voltage control for single-phase inverters," *iEEE Transactions on industrial Electronics*, vol. 61, no. 1, pp. 258–269, 2013.

[36] M. Savaghebi, J. M. Guerrero, A. Jalilian, and J. C. Vasquez, "Mitigation of voltage and current harmonics in grid-connected microgrids," in *2012 IEEE International Symposium on Industrial Electronics*. IEEE, 2012, pp. 1610–1615.

[37] A. Yazdani and R. Iravani, *Voltage-sourced converters in power systems: modeling, control, and applications*. John Wiley & Sons, 2010.

[38] E. Afshari, G. R. Moradi, R. Rahimi, B. Farhangi, Y. Yang, F. Blaabjerg, and S. Farhangi, "Control strategy for three-phase grid-connected pv inverters enabling current limitation under unbalanced faults," *IEEE Transactions on Industrial Electronics*, vol. 64, no. 11, pp. 8908–8918, 2017.

[39] F. Blaabjerg, R. Teodorescu, M. Liserre, and A. V. Timbus, "Overview of control and grid synchronization for distributed power generation systems," *IEEE Transactions on industrial electronics*, vol. 53, no. 5, pp. 1398–1409, 2006.

[40] M. Karimi-Ghartemani, S. A. Khajehoddin, P. Jain, and A. Bakhshai, "Linear quadratic output tracking and disturbance rejection," *International Journal of control*, vol. 84, no. 8, pp. 1442–1449, 2011.

[41] N. Krikelis and E. Papadopoulos, "An optimal design approach for tracking problems and its assessment against classical controllers," *International Journal of Control*, vol. 36, no. 2, pp. 249–265, 1982.

[42] B. Xie, M. Mao, L. Zhou, Y. Wan, and G. Hao, "Systematic design of linear quadratic regulator for digitally controlled grid-connected inverters," *IET Power Electronics*, vol. 13, no. 3, pp. 557–567, 2020.

[43] F. Huerta, D. Pizarro, S. Cobreces, F. J. Rodriguez, C. Giron, and A. Rodriguez, "Lqg servo controller for the current control of *lcl* grid-connected voltage-source converters," *IEEE Transactions on Industrial Electronics*, vol. 59, no. 11, pp. 4272–4284, 2011.

[44] F. Huerta, S. Cobreces, E. Bueno, F. Rodriguez, F. Espinosa, and C. Giron, "Control of voltage source converters with lcl filter using state-space techniques," in *2008 34th Annual Conference of IEEE Industrial Electronics*. IEEE, 2008, pp. 647–652.

[45] N. Arab, B. Kedjar, A. Javadi, and K. Al-Haddad, "A multifunctional single-phase grid-integrated residential solar pv systems based on lqr control," *IEEE Transactions on Industry Applications*, vol. 55, no. 2, pp. 2099–2109, 2018.

[46] S. Khajehoddin, M. Karimi-Gharteman, A. Bakhshai, and P. Jain, "High quality output current control for single phase grid-connected inverters," in *2014 IEEE Applied Power Electronics Conference and Exposition-APEC 2014*. IEEE, 2014, pp. 1807–1814.

[47] N. Arab, H. Vahedi, and K. Al-Haddad, "Lqr control of single-phase grid-tied puc5 inverter with lcl filter," *IEEE Transactions on Industrial Electronics*, vol. 67, no. 1, pp. 297–307, 2019.

[48] S. A. Khajehoddin, M. Karimi-Ghartemani, and M. Ebrahimi, "Optimal and systematic design of current controller for grid-connected inverters," *IEEE Journal of Emerging and Selected Topics in Power Electronics*, vol. 6, no. 2, pp. 812–824, 2017.

[49] R. S. Yallamilli, D. M. R. Korada, L. K. Vedulla, and M. K. Mishra, "Effective current based inverter loss computation and its application for energy savings in a microgrid environment," in *2020 IEEE International Conference on Power Electronics, Smart Grid and Renewable Energy (PESGRE2020)*. IEEE, 2020, pp. 1–6.

[50] Y. P. Kumar and R. Bhimasingu, "Review and retrofitted architectures to form reliable smart microgrid networks for urban buildings," *IET Networks*, vol. 4, no. 6, pp. 338–349, 2015.

[51] O. Palizban and K. Kauhaniemi, "Microgrid control principles in island mode operation," in *2013 IEEE Grenoble Conference.* IEEE, 2013, pp. 1–6.

[52] J. M. Guerrero, M. Chandorkar, T.-L. Lee, and P. C. Loh, "Advanced control architectures for intelligent microgrids—part i: Decentralized and hierarchical control," *IEEE Transactions on Industrial Electronics*, vol. 60, no. 4, pp. 1254–1262, 2012.

[53] T. L. Vandoorn, J. C. Vasquez, J. De Kooning, J. M. Guerrero, and L. Vandevelde, "Microgrids: Hierarchical control and an overview of the control and reserve management strategies," *IEEE industrial electronics magazine*, vol. 7, no. 4, pp. 42–55, 2013.

[54] D. Y. Yamashita, I. Vechiu, and J.-P. Gaubert, "A review of hierarchical control for building microgrids," *Renewable and Sustainable Energy Reviews*, vol. 118, p. 109523, 2020.

[55] A. Abhishek, A. Ranjan, S. Devassy, B. K. Verma, S. K. Ram, and A. K. Dhakar, "Review of hierarchical control strategies for dc microgrid," *IET Renewable Power Generation*, vol. 14, no. 10, pp. 1631–1640, 2020.

[56] S. Wang, J. Liu, Z. Liu, T. Wu, X. Meng, and B. Liu, "A hierarchical operation strategy of parallel inverters for efficiency improvement and voltage stabilization in microgrids," in *2016 IEEE 2nd Annual Southern Power Electronics Conference (SPEC).* IEEE, 2016, pp. 1–6.

[57] Y. Wang, D. Liu, Z. Chen, and P. Liu, "A hierarchical control strategy of microgrids toward reliability enhancement," in *2018 International Conference on Smart Grid (icSmartGrid)*. IEEE, 2018, pp. 123–128.

[58] Y. Wang, P. Liu, D. Liu, F. Deng, and Z. Chen, "Enhanced hierarchical control framework of microgrids with efficiency improvement and thermal management," *IEEE Transactions on Energy Conversion*, 2020.

[59] D. Li and C. N. M. Ho, "A delay-tolerable master–slave current-sharing control scheme for parallel-operated interfacing inverters with low-bandwidth communication," *IEEE Transactions on Industry Applications*, vol. 56, no. 2, pp. 1575–1586, 2019.

[60] Y. Wang, Y. Tan, Z. Chen, X. Wang, and Y. Tian, "A communication-less distributed voltage control strategy for a multi-bus ac islanded microgrid," in *2014 International Power Electronics Conference (IPEC-Hiroshima 2014-ECCE ASIA)*. IEEE, 2014, pp. 3538–3545.

[61] Y. Wang, X. Wang, Z. Chen, and F. Blaabjerg, "Distributed optimal control of reactive power and voltage in islanded microgrids," in *2016 IEEE Applied Power Electronics Conference and Exposition (APEC)*. IEEE, 2016, pp. 3431–3438.

[62] W. Yuan, Y. Wang, X. Ge, X. Hou, and H. Han, "A unified distributed control strategy for hybrid cascaded-parallel microgrid," *IEEE Transactions on Energy Conversion*, vol. 34, no. 4, pp. 2029–2040, 2019.

[63] W. Yuan, Y. Wang, D. Liu, and F. Deng, "Adaptive droop control strategy of autonomous microgrid for efficiency improvement," in *2019 IEEE 10th International Symposium on Power Electronics for Distributed Generation Systems (PEDG)*. IEEE, 2019, pp. 972–977.

[64] W. Yuan, Y. Wang, D. Liu, F. Deng, and Z. Chen, "Efficiency-prioritized droop control strategy of ac microgrid," *IEEE Journal of Emerging and Selected Topics in Power Electronics*, 2020.

[65] X. Lu, K. Sun, J. M. Guerrero, J. C. Vasquez, and L. Huang, "State-of-charge balance using adaptive droop control for distributed energy storage systems in dc microgrid applications," *IEEE Transactions on Industrial electronics*, vol. 61, no. 6, pp. 2804–2815, 2013.

[66] V. C. Gungor, B. Lu, and G. P. Hancke, "Opportunities and challenges of wireless sensor networks in smart grid," *IEEE transactions on industrial electronics*, vol. 57, no. 10, pp. 3557–3564, 2010.

[67] M. Erol-Kantarci and H. T. Mouftah, "Wireless sensor networks for cost-efficient residential energy management in the smart grid," *IEEE Transactions on Smart Grid*, vol. 2, no. 2, pp. 314–325, 2011.

[68] S. Dasgupta, S. N. Mohan, S. K. Sahoo, and S. K. Panda, "A plug and play operational approach for implementation of an autonomous-micro-grid system," *IEEE Transactions on Industrial Informatics*, vol. 8, no. 3, pp. 615–629, 2012.

[69] E. Serban and H. Serban, "A control strategy for a distributed power generation microgrid application with voltage-and current-controlled source converter," *IEEE Transactions on Power Electronics*, vol. 25, no. 12, pp. 2981–2992, 2010.

[70] H. Mahmood, D. Michaelson, and J. Jiang, "Strategies for independent deployment and autonomous control of pv and battery units in islanded microgrids," *IEEE Journal of Emerging and Selected Topics in Power Electronics*, vol. 3, no. 3, pp. 742–755, 2015.

[71] M. Mao, H. Huang, and L. Chang, "Real-time energy coordinated and balance control strategies for microgrid with photovoltaic generators," in *2013 4th IEEE*

International Symposium on Power Electronics for Distributed Generation Systems (PEDG). IEEE, 2013, pp. 1–7.

[72] N. L. Díaz, J. C. Vasquez, and J. M. Guerrero, "A communication-less distributed control architecture for islanded microgrids with renewable generation and storage," *IEEE Transactions on Power Electronics*, vol. 33, no. 3, pp. 1922–1939, 2017.

[73] D. Wu, F. Tang, T. Dragicevic, J. C. Vasquez, and J. M. Guerrero, "Autonomous active power control for islanded ac microgrids with photovoltaic generation and energy storage system," *IEEE Transactions on energy conversion*, vol. 29, no. 4, pp. 882–892, 2014.

[74] N. A. Ashtiani, A. Sheykhi, and S. A. Khajehoddin, "Parallel inverter system efficiency improvement using alternative adaptive droop control," in *2021 IEEE Applied Power Electronics Conference and Exposition (APEC)*. IEEE, 2021, pp. 790–795.

[75] S. A. Khajehoddin, M. Karimi-Ghartemani, and M. Ebrahimi, "Grid-supporting inverters with improved dynamics," *IEEE Transactions on Industrial Electronics*, vol. 66, no. 5, pp. 3655–3667, 2018.

[76] S. D'Arco and J. A. Suul, "Virtual synchronous machines—classification of implementations and analysis of equivalence to droop controllers for microgrids," in *2013 IEEE Grenoble Conference*. IEEE, 2013, pp. 1–7.

[77] C. Li, R. Burgos, I. Cvetkovic, D. Boroyevich, L. Mili, and P. Rodriguez, "Analysis and design of virtual synchronous machine based statcom controller," in *2014 IEEE 15th Workshop on Control and Modeling for Power Electronics (COM-PEL)*. IEEE, 2014, pp. 1–6.

92

[78] N. Soni, S. Doolla, and M. C. Chandorkar, "Improvement of transient response in microgrids using virtual inertia," *IEEE transactions on power delivery*, vol. 28, no. 3, pp. 1830–1838, 2013.

[79] ABB. ABB solar inverters for photovoltaic systems [Datasheets]. [Online]. Available: https://library.abb.com/en

[80] A. E.-M. M. Abd El-Aal, J. Schmid, J. Bard, and P. Caselitz, "Modeling and Optimizing the Size of the Power Conditioning Unit for Photovoltaic Systems," *Journal of Solar Energy Engineering*, vol. 128, no. 1, pp. 40–44, 03 2005.

[81] Y. Wang, D. Liu, P. Liu, F. Deng, D. Zhou, and Z. Chen, "Lifetime-oriented droop control strategy for ac islanded microgrids," *IEEE Transactions on Industry Applications*, vol. 55, no. 3, pp. 3252–3263, 2019.

[82] S. Peyghami, P. Davari, and F. Blaabjerg, "System-level reliability-oriented power sharing strategy for dc power systems," *IEEE Transactions on Industry Applications*, vol. 55, no. 5, pp. 4865–4875, 2019.

[83] K. Ma, M. Liserre, F. Blaabjerg, and T. Kerekes, "Thermal loading and lifetime estimation for power device considering mission profiles in wind power converter," *IEEE Transactions on Power Electronics*, vol. 30, no. 2, pp. 590–602, 2014.

[84] M. Ebrahimi, S. A. Khajehoddin, and M. Karimi-Ghartemani, "An improved damping method for virtual synchronous machines," *IEEE Transactions on Sustainable Energy*, vol. 10, no. 3, pp. 1491–1500, 2019.

[85] A. Sheykhi, N. A. Ashtiani, and S. A. Khajehoddin, "Microgrid light-load efficiency improvement based on online-inverter detection," in *2021 IEEE Energy Conversion Congress and Exposition (ECCE)*. IEEE, 2021.